Summer 2013

Detecting activity-evoked pH changes in human brain

Hye Young Heo
University of Iowa

DETECTING ACTIVITY-EVOKED PH CHANGES IN HUMAN BRAIN

by

Hye Young Heo

A thesis submitted in partial fulfillment of the
requirements for the Doctor of Philosophy
degree in Biomedical Engineering
in the Graduate College of
The University of Iowa

August 2013

Thesis Supervisor: Associate Professor Vincent A. Magnotta

Graduate College
The University of Iowa
Iowa City, Iowa

CERTIFICATE OF APPROVAL

PH. D. THESIS

This is to certify that the Ph.D. thesis of

Hye Young Heo

has been approved by the Examining Committee for the thesis requirement for the Doctor of Philosophy degree in Biomedical Engineering at the August 2013 graduation.

Thesis Committee:
Vincent A. Magnotta, Thesis Supervisor

John A. Wemmie

Joseph M. Reinhardt

Edwin L. Dove

Daniel R. Thedens

To my wife, Youngeun

ACKNOWLEDGMENTS

My graduate experience has been challenging and valuable venture at the University of Iowa. Many people provided me support, guidance and encouragement over the years and now it is time to reply my appreciation to them.

I would like to express my deepest gratitude to my research advisor Dr. Vincent Magnotta who was my thesis supervisor. He gave me the opportunity to work at the department of Radiology and an indispensable encouragement for my research. He has been with me every step of the way guiding my work and nurturing my career. I would also like to thank to my research advisor, Drs. John Wemmie and Daniel Thedens for their consistent guidance, encouragement and support of this thesis work. I would like to thank the other members of my thesis committee, Drs. Joseph Reinhardt and Edwin Dove for their guidance and perspectives.

I could not have achieved my research without MRRF lab colleagues. I would like to thank Marla Kleingartner, Joe Ekdahl, Autumn Craig, Greg Pickett, Casey Johnson, Jeff Yager, Wen Li, and other lab members to help my research.

Thank you to my parents for their incredible love and support. To Youngeun, my wife and Sunghoon, my son, I love you.

ABSTRACT

Localized pH changes have been suggested to occur in the brain during normal function. However, a lack of methods for non-invasively measuring pH with high spatial and temporal resolution limits current knowledge of brain pH dynamics. Here I report that a magnetic resonance imaging (MRI) strategy named T_1 relaxation in the rotating frame ($T_{1\rho}$) is sufficiently sensitive to detect widespread pH changes in the mouse and human brain evoked by systemically manipulating carbon dioxide (CO_2) or bicarbonate (HCO_3). Moreover, $T_{1\rho}$ detected changes suggesting a localized acidosis in the human visual cortex induced by a flashing checkerboard. Lactate measurements and pH-sensitive ^{31}P spectroscopy at the same site also suggest a localized acidosis. Consistent with the established role for pH in blood flow recruitment, $T_{1\rho}$ correlated with blood oxygenation level dependent contrast (BOLD), although $T_{1\rho}$ was directly sensitive to blood oxygen content. These observations provide the strongest evidence thus far for localized pH fluctuations in the human brain during normal function. Furthermore, they suggest a novel functional imaging strategy based on pH that is independent of traditional fMRI contrast mechanisms.

Possible sources of acidosis include local metabolism, which is likely to correlate with the degree of stimulation and the associated changes in local neural activity. Therefore, we hypothesized that $T_{1\rho}$ and pH changes would increase with increasing stimulation frequency. To test this hypothesis, we used a full-field visual flashing checkerboard and varied the frequency between 1, 4, and 7Hz. The response was imaged with $T_{1\rho}$, BOLD, and ^{31}P spectroscopy. Supporting our hypothesis, we found that increasing stim ulation frequency increased responses measured by all three imaging

modalities. The activation area detected by $T_{1\rho}$ overlapped to a large degree with that detected by BOLD, although the $T_{1\rho}$ response area was significantly smaller. ^{31}P spectroscopy detected a greater acidosis with the higher stimulation frequencies. These observations suggest that, similar to the BOLD response, the magnitude of the $T_{1\rho}$ and pH response depends on stimulation frequency and is thus likely to be activity-dependent.

Brain acidosis is the end product of energy metabolism. Metabolically active cells lower local pH, the detection of which could help pinpoint regions activated by sensory stimuli, emotion, or cognitive task. fMRI mostly relies on BOLD changes in the venous system while arterial spin labeling (ASL) enables changes in tissue perfusion resulting from local cerebral blood flow (CBF) changes. BOLD contrast can be significantly distant from the actual site of neuronal activity because it relies on changes of the local magnetic field within veins. The venous contribution results in a loss of spatial specificity and spatial resolution of the BOLD response. In addition, the hemodynamic response to brief periods of neural activity is delayed. However, ASL contrast originates predominantly from tissue and capillaries. Even though functional signal changes detected by ASL have superior spatial and temporal resolution as compared to BOLD contrast, ASL contrast still suffers from poor temporal resolution due to delays in the hemodynamic response resulting from neurovascular coupling. Therefore, the ability to measure pH dynamics may provide a more localized and direct measure of brain activity. We hypothesized that pH-sensitive $T_{1\rho}$ response in the visual cortex will temporally precede the hemodynamic response measured by functional imaging including BOLD and ASL contrast since local acidosis evoked by neural activity may drive the hemodynamic response. To test this hypothesis, dynamic imaging was performed using

$T_{1\rho}$, BOLD, and ASL while viewing a phase-encoded expanding ring stimulus which induces travelling waves of neural activity in the visual cortex. We calculated the phase maps for the eccentricity across their occipital cortices for each of functional signal and compared the $T_{1\rho}$ temporal resolution with the hemodynamic response. This study suggests that $T_{1\rho}$ signal has a higher temporal resolution as compared to the hemodynamic response. This is further evidence that the $T_{1\rho}$ signal is not sensitive to blood oxygenation or other blood factors that might alter $T_{1\rho}$.

In conclusion, $T_{1\rho}$ imaging has the potential to provide a new functional imaging marker that may be more specific to the area of brain activity. Therefore, it is possible that by non-invasively detecting pH dynamics in the human brain, $T_{1\rho}$ MRI could offer a novel, more direct approach to map brain function. A number of psychiatric and neurological disorders could potentially benefit from the ability to study dynamic pH changes.

TABLE OF CONTENTS

LIST OF TABLES

LIST OF FIGURES

CHAPTER 1

INTRODUCTION

1.1. Importance of pH Measurement

Over the past decade, researchers in neuroscience have investigated how brain cells regulate their intracellular pH and the consequence of this change in their immediate extracellular environment. It has become clear that neural activity within the brain induces changes in both intracellular and extracellular pH, which in turn have important consequence for brain function. In addition to the neural activity, a number of CNS diseases are associated with acidosis, such as seizures, stroke, and multiple sclerosis [1-8]. Therefore these pH fluctuations likely play critical roles in the understanding of brain function and pathophysiology.

1.1.1. Functional pH change in neural activity

The neural activity in brain cells is extremely sensitive to the effect of chemical factors and both endogenous and exogenous modulators. One of the most potent endogenous neuromodulators within the brain is the positive hydrogen ion (H^+), which plays a crucial role in biological organizations because of the presence in protein of charged groups capable of binding and releasing H^+ ions. The change of pH by these interactions influence numerous biophysical and biochemical functions; yet the mechanism that underlie these interactions are still only partially understood. Neural activation in the brain is inevitably associated with metabolic changes such as oxygen

and glucose uptake. Changes in individual ions and molecules (H^+ and others), by mechanisms not entirely understood [9,10], lead to local changes in blood flow, blood volume and blood oxygenation via so-called neurovascular coupling [11,12].

Neural activities by sensory stimuli, emotion, or cognitive tasks lower local pH [8,13,14]. The local acidosis in activated regions potently increases CBV and CBF, providing a more direct measure of neural activity as well as a better understanding of the BOLD response. Neural activities generate lactate, CO_2 and other metabolites that lower interstitial pH (Figure 1.1). These and the synaptic release of protons from neurotransmitter (NT) vesicles lower pH in the synaptic cleft to modulate pH sensitive channels and other receptors in the pre- and post-synaptic membrane. In addition, increased metabolic activity also produces more CO_2, which is rapidly hydrated to HCO_3^- and H^+. Illustrated in Figure 1.1 are voltage-gated Ca_2^+-channels (VGCC), NMDA receptors, and ASICs. Neuron activation generates acidosis that begins within seconds to minutes and lasts for minutes or longer. The degree of acidification and its duration depend on the magnitude of activity. CO_2 and proton generation from carbohydrate metabolism are likely responsible for the pH changes that are seen.

Brain activation is accompanied by a complex sequence of cellular, metabolic, and vascular processes. Various cellular processes of neurons require energy in the form of adenosine triphosphate (ATP). ATP is synthesized first by glycolysis, which is anaerobic and produces a small amount of ATP, and by oxidative glucose metabolism, which requires oxygen and produces a large amount of ATP. In the brain, most glucose is metabolized by the latter mechanism aerobically. Therefore cerebral metabolism depends on a constant supply of both glucose and oxygen. A continuous supply of these two

energy substrates is maintained by the cerebral blood flow (CBF), which delivers glucose and oxygen to neural tissue through a complex web of blood vessels. Also increased activation removes metabolic waste including CO_2 through the cerebral vasculature. The ability of neurons and glia to generate signals to increase blood flow to match local demand is collectively called neurovascular coupling. As early as 1890, Roy and Sherrington suggested that acidosis increases CBF [15,16]. Many subsequent studies confirmed that local acidosis is a critical determinant of cerebrovascular tone. Carbon dioxide inhalation causes marked cerebral vasodilation, whereas hypocapnia results in pronounced vasoconstriction. Indeed, the cerebral blood flow can be reduced by voluntary hyperventilation. A change in arterial pCO_2 alters pH both inside and outside blood vessels. However, if the arterial pCO_2 is kept constant, the pH changes in the blood do not affect the cerebral blood flow. This evidence points toward pH changes in the brain tissue being responsible for CO_2 reactivity. Brain tissue acidosis accounts for the vasodilation associated with increased neuronal activity because the metabolic end product of cerebral metabolism is carbon dioxide. Consequently, activity-evoked pH changes may precede the hemodynamic responses measured by functional imaging including fMRI BOLD contrast. The ability to non-invasively detect the change of brain pH could offer a novel, more direct approach to map and understand brain function.

1.1.2. Localized acidosis in CNS diseases

Brain pH is largely controlled by the CO_2/HCO_3^- buffering system, which is acutely regulated by breathing. Recently, increasing evidence suggests that pH may be abnormally regulated in panic disorder [17,18]. Furthermore, CO_2 inhalation triggers

panic attacks and patients with panic disorder are particularly sensitive [18]. CO_2 is constantly produced in the brain as an end product of carbohydrate metabolism. It readily crosses cell membrane such as blood-brain barrier. In a reaction catalyzed by carbonic anhydrase, CO_2 is hydrolyzed to carbonic acid (H_2CO_3), which readily dissociated into HCO_3^- and H^+. The resulting acidosis is thought to be responsible for most of the physiological effects of CO_2. Therefore, the CO_2 inhalation is likely to acidify brain pH.

Brain pH changes have been shown to be sensitive to assessment of tumor and stroke. In addition, disrupting ASIC1a gene or blocking its activity had been shown to produce profound effects in mice; including markedly attenuated anxiety and depression-related behaviors, prevented neuronal loss in a model of multiple sclerosis (MS), reduced neuronal injury in ischemia, and altered seizure severity [18-21]. A significant drop in brain pH during neuronal excitation or seizure activity suggests that ASIC activation might occur and activated ASICs play a role in the generation of epileptic seizures. Stroke and multiple sclerosis can produce even more substantial and sustained brain acidosis. During neurological conditions such as brain ischemia, increased anaerobic glycolysis due to reduced oxygen supply leads to lactic acid accumulation [22]. Accumulation of lactic acid, alone with increased H^+ release from ATP hydrolysis, causes a decrease in pH, resulting in brain acidosis. During brain ischemia, for example, extracellular pH falls to 6.5 or lower. In addition, epilepsy is a very common form of abnormal brain function that appears to be influenced by pH [22,23]. These pH fluctuations likely play critical roles in brain physiology and pathophysiology. Therefore, the ability to measure pH could offer a novel, more direct approach to map brain function as well as to detect disease and response to treatment.

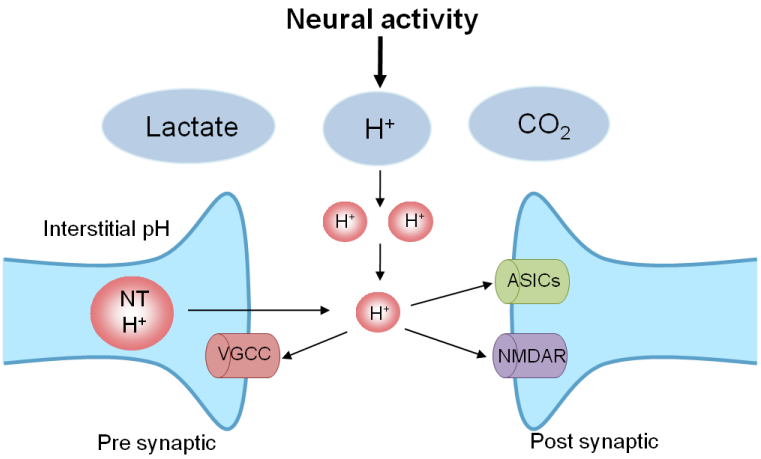

Figure 1.1. Model of proton signaling in the brain [30]. Cellular activity and disease generate CO_2, lactate, hydrogen ion, and other metabolites that lower interstitial pH. Theses and synaptic release of protons from neurotransmitter (NT) vesicles lower pH in the synaptic cleft to modulate pH sensitive channels and other receptors in the pre- and post-synaptic membrane. Illustrated are voltage-gated Ca_2^+-channels (VGCC), NMDA receptors, and ASICs.

CHAPTER 2

BACKGROUND AND LITERATURE REVIEW

2.1. Brief Introduction to Magnetic Resonance Imaging

The foundation of magnetic resonance imaging began with the development of nuclear magnetic resonance discovered independently by Felix Bloch and Edward Purcell in 1946 [24,25]. The use of magnetic resonance (MR) imaging is growing exponentially, in part because of the excellent anatomic and pathologic detail provided by the modality and because of recent technologic advances that have led to faster acquisition times. In addition, functional imaging of the brain is one of the most exciting recent developments in MR imaging. The visualization of activated brain regions during external stimulus or performing specific tasks opens a completely new perspective for the use of MRI. Recently, developed techniques offer functional information of the brain with high temporal and spatial resolution.

Any nucleus with unpaired protons and/or neutrons has a net spin, which is potentially applicable for MRI. Spin is the tendency to behave like a spinning ball of charge. Any time a charge moves, it creates a magnetic field. Some biologically important nuclei that have angular momentum include ^{1}H, ^{13}C, ^{17}O, ^{23}Na, and ^{31}P. However the hydrogen nucleus, ^{1}H, consists of a single proton and is of great abundance in human tissues, making it an excellent element to be exploited for clinical imaging.

Thermal (Brownian) motion molecules have random orientation, thus creating no net magnetic field of the spin system. When a particle with a net spin is placed in a

magnetic field, it can absorb photons of energy at a very specific energy. This frequency, the Larmor frequency, is determined by the gyromagnetic ratio of the particles

$$\omega = \gamma B \tag{2.1}$$

where γ is the gyromagnetic ratio of the atom, B is the magnetic field that the atom experiences, and ω is the resulting frequency at which energy can be absorbed. The random orientation of individual spins causes the net magnetization M_0 to be zero. However, when placed in a magnetic field, each atom may be at one of two slightly different energy states, either parallel or anti-parallel to the field as shown in Figure 2.1. The energy difference between these energy states ΔE is

$$\Delta E = \hbar\omega_0 = \gamma\hbar B_0 = h\frac{\gamma}{2\pi}B_0 \tag{2.2}$$

where h is the Planck's constant ($\hbar = h/2\pi$). In an equilibrium state, greater numbers of protons occupy the lower energy states resulting in M_0, which is aligned along the B_0, referred to as z-axis. The difference between two energy states is proportional to the magnetic field B_0 in which the atom is placed.

In order to gain information from the object, the spin system must be disturbed by a short temporary radio frequency (RF) pulse applied at the Larmor frequency. After applying the RF pulse, changes between the spin states of the nuclei and each individual spin can occur independently. The transmitting RF coil creates a magnetic field B_1 that is perpendicular to the B_0. By applying a B_1 field at the Larmor frequency ω, the M_0 can be tilted. The angle of this flip depends on intensity, waveform and duration of the RF pulse. This RF pulse causes phase coherence for the spins by exciting the spins. After a 90 degree pulse, the magnetization will become tilted to the transverse plane (xy). After this

excitation, the spins start to return to the equilibrium state. The excited spins lose their energy and also their phase coherence, i.e. spin synchronicity. This relaxation of the nuclei is the return of the distribution of spins towards the Bolzmann distribution. The change from higher energy state to lower causes the nuclei to emit energy at the Larmor frequency. This precession of the M_0 during the return to the z-axis will induce an electrical signal with a frequency ω into the RF coil. Figure 2.2 shows this resulting signal, which is called the free induction decay (FID).

There are two relaxation processes by which nuclear magnetization obeys: the longitudinal, or spin-lattice relaxation (T_1) and the transverse, or spin-spin relaxation (T_2). After applying an RF pulse, the spins return to their equilibrium state in which there is no transverse magnetization and the longitudinal magnetization is at its maximum value and oriented in the direction of main magnetic field (B_0). As shown in Figure 2.2, the magnetization recovers to 63% of its equilibrium value after one time constant T_1. The longitudinal relaxation time (T_1) determinates the rate at which the equilibrium state is achieved. The external magnetic field inhomogeneities and interaction between spins cause net magnetization to dephase in transverse plane. The magnetization drops to 37% of its original magnitude. The rate of phase coherence loss is the transverse relaxation time (T_2). T_2 decay depends primarily on spin-spin and spin-surroundings interactions whereas so called T_2^* decay depends additionally on susceptibility gradients and external polarizing field inhomogeneities.

2.1.1. T_1 and T_2 relaxation

A MR signal intensity depends mainly on the proton density and the relaxation time of water protons. There are two parameters that the user can tune to vary the contrast in the MR image: repetition time (TR) and echo time (TE). Theses parameters can be varied to achieve PD, T_1 and T_2 weighted images. Different tissues have unique T_1 and T_2 relaxation time constants. These relaxation time constants determine the exponential decay curve for the MR signal. In conventional spin-echo experiments, TE is the time from the 90° RF pulse to the center of the echo. TR is the time between two repeated 90° RF pulses. By changing the TR and/or TE, T_1 or T_2-weighted images are acquired. The MR signal intensity for each pixel in an image can be described as

$$S = S_0(1 - e^{-TR/T_1})\ e^{-TE/T_2} \tag{2.3}$$

In T_1 relaxation, the energy induced by the RF pulse dissipates into the surrounding tissue. The most efficient energy transfer occurs when the natural motional frequency (translation, rotation, and vibration) of the protons are at the Larmor frequency. However, the natural motional frequency of water protons depends on the physical states of the tissue. It is influenced by the atoms to which they are attached or to which they are proximal. The time needed for this energy dissipation through dipole-dipole interaction is represented by the constant T_1. T_1 is sensitive to rapid motion of the proton environment compared to T_2 due to its sensitivity to small disturbances in the magnetic field that occur at the Larmor frequency. This makes the T_1 relaxation field dependent on its immediate environment and its relaxation time longer as the strength increases. In the small water molecule, protons have high natural motional frequencies. The natural motional

frequency of the proton in water is also much faster than the Larmor frequency for hydrogen. In solids, protons have lower natural motional frequencies than do water protons. The natural motional frequencies of protons in solids are slower than the Larmor frequency for hydrogen. Protons in fat have frequencies that are almost equal to the Larmor frequencies for water. This result is caused by the rotational frequency of the carbons around the terminal C-C bond. Because this frequency is near the Larmor frequency, the efficiency of energy transfer from the protons to the lattice or from the lattice to the protons is increased, thus decreasing T_1.

The transverse relaxation is characterized by the T_2 constant. It is caused by time varying dipole-dipole interactions, where energy is not dissipated, but signal is lost due to dephasing of spins. T_2 is relatively independent to field strength and it is more related to the slow variations, large τc which is the correlation time of the interactions of the spins with their environment, in the local magnetic environment. In water molecules, spin-spin interaction among the protons is negligible because the distance between protons both within each molecule and between adjacent molecules is relatively large. Thus T_2 relaxation time is long due to slower dephasing rate. The molecular structure of solids is opposite to that of water, which is dense structure, allowing many interactions between protons. This large number of interactions results in more dephasing. Therefore, T_2 relaxation time for solids is short.

Most of the water in the body is not in the pure state but is bound to a macromolecule such as a protein. These bound water molecules lose their own mobility. Therefore it makes a more efficient energy transfer because the frequencies of the bound water molecules get closer to the Larmor frequency. The net result is a shortening in the

T_1 relaxation. However, T_1 for H_2O and solid tissue is long because the energy transfer is not efficient. In addition, the T_1 of water is longer than the T_1 for solid tissue because the difference between the Larmor frequency and the natural motional frequencies of protons in water is much greater than the difference between the Larmor frequency and the motional frequencies of protons in solid tissue.

2.1.2. $T_{1\rho}$ and $T_{2\rho}$ relaxation

The spin lattice relaxation time (T_1) at low field strengths provides information from the processes at macromolecular level with slow correlation time because T_1 is dependent on the magnetic field strength. However, the low field strength decreases the signal to noise ratio (SNR) that affects the quality of MR images. Therefore, the relaxation time constant of low field strengths was combined with the high SNR provided by the higher field MRI was introduced [26,27]. The $T_{1\rho}$ is the spin lattice relaxation time constant (T_1) in the rotating frame, which determines the decay of the transverse magnetization in the presence of a very low magnetic field, spin-lock RF field. In conventional T_1 relaxation, spins exchange energy with the surrounding lattice via processes that occur near the Larmor frequency. The spin-lock RF pulse can change the environment in which individual spins are able to interact with the lattice. In the presence of a spin-lock RF field, spins are able to efficiently couple to the lattice at frequencies close to the spin-lock RF pulse frequency which is typically far below the Larmor frequency.

Measurement of the MR signal following the spin-lock pulse (Figure 2.3A) is ideal for spectroscopic measurement of $T_{1\rho}$. The first RF pulse flips the longitudinal

magnetization into the transverse plane (xy plane). The B_{1+y} represents the spin-lock pulse and TSL and B_1 are its duration and amplitude, respectively. The dotted line represents the decay of the magnetization in the absence of spin-lock pulse and is governed by T_2^*. In contrast, if the magnetization is spin-locked, it decays according to $T_{1\rho}$ (solid line) while the spin-lock pulse is applied. However, the decay is T_2^* again after the spin-lock pulse. For $T_{1\rho}$ imaging applications, the $T_{1\rho}$-prepared RF pulse cluster with self-compensating spin-lock pulse as shown in Figure 2.3B is more useful to prepare the magnetization because the self-compensating pulse refocuses dephasing from B_1 inhomogeneity by reversing the direction of the precession of the spins in the rotating frame halfway through the duration of the spin-lock pulse. Figure 2.4 shows the magnetization decays according to the spin lattice relaxation in the rotating frame during TSL. The measured $T_{1\rho}$ relaxation decay follows the equation.

$$S = S_0 e^{-TSL/T_{1\rho}} \tag{2.4}$$

where S_0 is the signal intensity produced when no spin-lock pulse is applied and TSL is the duration of spin-lock encoding. By changing the TSL in successive images, quantitative absolute $T_{1\rho}$ maps can be calculated. The rate of relaxation is defined by the $R_{1\rho}$ parameter, which is simply the reciprocal of $T_{1\rho}$.

Using the Block equations, we can mathematically model the evolution of magnetization under the pulse sequence illustrated above. Figure 2.5 contains the rotating frame magnetization vector diagrams accompanying the equations presented below.

Firstly, we assume that a sample has a thermal equilibrium magnetization normalized to a value of 1.

$$M_x = 0,\ M_y = 0,\ M_z = 0 \tag{2.5}$$

We apply an RF pulse along the x-axis of width τ and amplitude ω_{1x}, causing a $\theta = \omega_{1x}\,\tau$.

$$M_x = 0,\ M_y = sin\theta,\ M_z = cos\theta \tag{2.6}$$

After applying the RF pulse (90^{o}_{-x}) to flip the magnetization vector (M) into the transverse plane, we apply a spin-lock pulses along the y-axis of amplitude ω_{1y} for a time TSL. In order for the spins to stay aligned in the locking field B_1, spin-lock pulses must be higher than the local fields of water nuclei [26,28,29]. During applying spin-lock pulses, the magnetization is spin-locked with amplitude B_1 for a time of spin lock (TSL) and undergoes the $T_{1\rho}$ relaxation in the presence of a B_1 field of the spin-lock pulses in the rotating frame. Magnetization perpendicular to the spin-locking field also decay with a time constant $T_{2\rho}$, which can be estimated as the reciprocal average of T_1 and T_2. Furthermore, magnetization perpendicular to the spin-locking vector will precess about it with an angular frequency ω_{1y}, resulting in a rotation of $\alpha = \omega_{1y}$ TSL.

$$M_x = -cos\theta\ sin\alpha \cdot e^{-TSL/T2\rho} \tag{2.7}$$

$$M_y = sin\theta \cdot e^{-TSL/T1\rho} \tag{2.8}$$

$$M_z = cos\theta\ cos\alpha \cdot e^{-TSL/T2\rho} \tag{2.9}$$

At the end of the spin-lock pulses, the magnetization is nutated back into the longitudinal axis using a nonselective RF pulse (90^{o}_{-x}) along the x axis, causing a rotation of – θ.

$$M_x = -cos\theta\ sin\alpha\ e^{-TSL/T2\rho} \tag{2.10}$$

$$M_y = sin\theta \cdot\ e^{-TSL/T1\rho} -\ sin\theta\ cos\theta\ cos\alpha \cdot\ e^{-TSL/T2\rho} \tag{2.11}$$

$$M_z = sin^2\theta\ \cdot e^{-TSL/T1\rho} +\ cos^2\theta\ cos\alpha \cdot\ e^{-TSL/T2\rho} \tag{2.12}$$

This complex magnetization orientation is simplified somewhat with the application of a crusher gradient, which removes transverse magnetization, resulting in

$$M_x = 0 \tag{2.13}$$

$$M_y = 0 \tag{2.14}$$

$$M_z = sin^2\theta\ \cdot e^{-TSL/T1\rho} +\ cos^2\theta\ cos\alpha\ \cdot e^{-TSL/T2\rho} \tag{2.15}$$

If the flip angle θ is calibrated to be a 90° pulses, the longitudinal magnetization is simply

$$M_z = e^{-TSL/T1\rho} \tag{2.16}$$

For regions where the flip angle is accurately calibrated to be a 90° pulses, the longitudinal magnetization contains only information regarding $T_{1\rho}$ as shown in Equation 2.15. However, Equation 2.4 is often used due to B_1 inhomogeneity that exists. Several methods exist for reduction of this flip angle dependence. The use of adiabatic 90° pulses may be implemented instead of hard pulses [30]. Adiabatic pulses provide a robust means of achieving more uniform flip angle in spite of variations in B_1. However, the use of the adiabatic pulses is limited due to high specific absorption ratio (SAR). Another method is

to use a "rotary echo" spin-lock pulse with 90° pulses shift for half of the spin-lock time (B_{1+y}) and a -90° pulses shift for the remainder of the spin-lock time (B_{1-y}) as shown in Figure 2.3B [31]. In this case, the magnetization undergoes a rotation of α/2 during the first half of the spin-lock pulse.

$$M_x = -cos\theta\ sin\frac{\alpha}{2} \cdot e^{-TSL/2T2\rho} \tag{2.17}$$

$$M_y = sin\theta \cdot e^{-TSL/2T1\rho} \tag{2.18}$$

$$M_z = cos\theta\ cos\frac{\alpha}{2} \cdot e^{-TSL/2T2\rho} \tag{2.19}$$

The second half of the spin-locking pulse is applied with a -90° phase, causing a rotation of - α/2, and the magnetization becomes

$$M_x = 0 \tag{2.20}$$

$$M_y = sin\theta \cdot e^{-TSL/T1\rho} \tag{2.21}$$

$$M_z = cos\theta \cdot e^{-TSL/T2\rho} \tag{2.22}$$

Lastly, we apply the RF pulse (90^{o}_{-x}) along the x axis to nutate back into the longitudinal axis.

$$M_x = 0 \tag{2.23}$$

$$M_y = sin\theta cos\theta \cdot (\ e^{-TSL/T1\rho} - \ e^{-TSL/T2\rho}) \tag{2.24}$$

$$M_z = sin^2\theta \cdot e^{-TSL/T1\rho} + \ cos^2\theta \cdot e^{-TSL/T2\rho} \tag{2.25}$$

We can remove the transverse magnetization with application of a crusher gradient, leaving only Mz. Dependence of Mz on α is removed with use of the self-compensating spin-lock pulse. However, a portion of magnetization is still lost to $T_{2\rho}$ relaxation if the flip angle (θ) is not 90°, and magnetization undergoing $T_{1\rho}$ relaxation is again degraded by a factor $\sin^2 \theta$.

Equation (2.14) indicates that the longitudinal magnetization has a complex dependence on flip angle, magnetization rotation about the spin-lock vector, and relaxation times. In order to visualize the effects of relaxation times and varying B_1, the longitudinal magnetization was plotted as a function of B_1 for varying values of $T_{1\rho}$ and $T_{2\rho}$ as shown in Figure 2.6. B_1 is considered to vary from 20μT to 30μT. $B_{1\rho}$ is considered to vary from 18μT to 27μT. B_1 pulse width is calibrated to have 90° flip angle when B_1 is at its maximum value of 30μT. Note that changes in B_1 linearly affect both spin-locking power ($B_{1\rho}$) and flip angles of the RF pulse (B_1). $T_{1\rho}$ weighted images are very sensitive to flip angle, and thus dependent on the B_1 field homogeneity according to equations (2.9)–(2.14). Simulations as shown in Figure 2.6 show that spatial variation in signal intensity is induced, with an oscillatory dependence on B_1, resulting from the small variations in B_1. Figure 2.6A and 2.6B show that the signal intensity is increased with longer $T_{1\rho}$. However, the signal intensity is decreased with shorter $T_{1\rho}$, and the significance of these oscillations increases, even though the absolute amplitude of the oscillations is independent of $T_{1\rho}$. In results, the amplitude of the oscillations relative to the mean signal intensity increases with short $T_{1\rho}$. However, the artifacts are dramatically reduced by using the self-compensating spin-lock pulse as shown in Figure 2.6A-D (dashed line). Figure 2.6E shows the longitudinal magnetization with varying B_1 (20μT to

30μT), $B_{1\rho}$ (18μT to 27μT and 10μT to 15μT) and fixed $T_{1\rho}$ / $T_{2\rho}$ of 1/0.2s. We found that the spin-lock pulse amplitude range does not affect the absolute amplitude of the oscillations, but the frequency of the oscillation. Figure 2.7 shows the two simulated $T_{1\rho}$ curves at spin-lock fields ($B_{1\rho}$) of 10μT and 18μT with a fixed $T_{1\rho}$ / $T_{2\rho}$ of 0.01/0.002s by solving the classical Bloch equations (Equation 2.4-2.24). Figure 2.7B shows the simulated curves from Figure 2.7A with overall $T_{1\rho}$ decay multiplied out. Remaining are the oscillation (red and blue lines) and the $T_{2\rho}$ decay (black dashed line). The oscillation caused by residual dipolar interactions are a measure of how long the spin-lock magnetization shows distinct dephasing and rephrasing patterns. However, the oscillation amplitude is reduced over time due to $T_{2\rho}$ decay. Figure 2.8A-E shows the magnetization vector during the TSL in the presence of dephasing caused by residual dipolar interactions. Figure 2.8F shows the corresponding time evolution of the MR signal coherence, which looks similar to a conventional spin echo. However, the advantage to spin-lock is that a higher spin-lock field translates into shorter refocusing times and more efficient refocusing of residual dipolar interaction. The illustrations in Figure 2.8A-E show the dephasing spins remaining in a single plane. In reality, even during spin-lock the spins migrate from the plane and the oscillation amplitude shown in Figure 2.8F will dampen over time ($T_{2\rho}$ decay).

$T_{1\rho}$ relaxation results from the mechanism of proton exchange and translational diffusion and the relaxation rates of each component are additive. In biological tissues, amide and hydroxyl groups are the primary contributors to proton exchange [32]. The slow molecular tumbling of macromolecules and their rotational interactions with surrounding water molecules contribute to the dipolar relaxation mechanism [33].

However, the dipolar relaxation processes does not significantly affect the overall dispersion of $T_{1\rho}$ relaxation because the wide frequency distribution appears as a broad spectrum that may be 10-100 kHz wide. Also the rate of diffusion of water molecules is not significantly affected by the spin-locking fields. Therefore $T_{1\rho}$ dispersion is dominated by the mechanism of proton exchange. Consequently, $T_{1\rho}$ dispersion has been shown to be sensitive to changes that affect proton exchange such as pH and ^{17}O concentration [32,34-37].

Figure 2.9 shows the conventional $T_{1\rho}$-weighted pulse sequence with spin-echo (SE) readout. In spin-lock preparation part, the magnetization becomes "$T_{1\rho}$-prepared" and results in a $T_{1\rho}$-weighted MR signal. Single slice of the $T_{1\rho}$-prepared magnetization is excited using a 90° slice-selective pulse followed by a conventional SE readout.

$T_{1\rho}$-weighted pulse sequence can be also be implemented using a turbo spin-echo readout (TSE). By using turbo spin-echo readout, several lines of k-space can be acquired within each TR period reducing the total scan time to obtain an image substantially. An example of $T_{1\rho}$-weighted pulse sequence with TSE readout is illustrated in Figure 2.10. An echo train length of four is shown which would result in four k-space lines being acquired per excitation thereby expediting the image acquisition by a proportionate factor. Figure 2.11 shows the $T_{1\rho}$-weighted pulse sequence with EPI readout. A nonselective 90° pulse excites spins that are then spin-locked in the transverse plane by the application of two phase-alternating spin-lock pulses. The alternately phased spin-lock pulse implements the self-compensating method to improve the spin-lock magnetic field homogeneity. A second nonselective 90° pulse restores the spin-locked magnetization to the longitudinal axis. A large amplitude crushed gradient is subsequently applied to

destroy a residual transverse magnetization. After spin-lock preparation, the longitudinal magnetization with $T_{1\rho}$ prepared is subsequently imaged using a spin-echo EPI sequence with rectilinear k-space sampling. The fast $T_{1\rho}$ imaging combined with the EPI readout can facilitate to use functional MRI with $T_{1\rho}$ contrast.

2.2. Functional Magnetic Resonance Imaging

Functional Magnetic Resonance Imaging (fMRI) is an MRI procedure that measure neural activity in the brain. fMRI using the blood oxygenation-level dependent (BOLD) response is by far the most commonly employed method for noninvasive localization of activity in the brain in cognitive psychology investigations even though several other functional methods exist. These include arterial spin labeling (ASL) and vascular-space-occupancy (VASO). ASL depends on measuring blood perfusion by assessing the difference between a measurement where the blood is tagged magnetically and a control experiment without tagging. The VASO method measures blood volume changes.

2.2.1. Blood oxygenation level dependent based fMRI

BOLD signal have been widely used the contrast for fMRI although other contrast measures that are more directly coupled to neuronal activity exist. Ogawa reported that functional brain mapping is possible by using the venous BOLD contrast in 1990 [38-41]. The BOLD contrast relies on changes in deoxyhemoglobin (dHb), which acts as an endogenous paramagnetic contrast agent [42]. The change results from blood flow including blood volume, perfusion, and blood velocity and oxygen extraction

fraction are the primary links to local metabolism and neuronal function. Therefore, changes in the local dHb concentration in the brain lead to alterations in the signal intensity of magnetic resonance images (Figure 2.12).

2.2.1.1. Blood Oxygenation Level Dependent

MR signal intensity and spatial localization depend on a uniform magnetic field existing throughout the sample of interest. However homogenous magnetic field is limited by the fact that different tissues and material possess a property called magnetic susceptibility. The magnetic susceptibility influences the magnetic field that protons experience inside a tissue or material. Changes in MR susceptibility disrupts the uniformity of the magnetic field resulting in signal loss near the boundary between these changes. For fMRI, the magnetic susceptibility of oxygenated and deoxygenated blood differs, with oxygenated blood having a magnetic susceptibility closer to that of the surrounding tissue. The difference in magnetic susceptibility between oxygenated and deoxygenated blood is small, on the order of tenths of parts per million. However, the protons in the tissue surrounding the blood vessels are affected by this microscopic field variation, resulting in an increase in the T_2^* relaxation constant and decrease in signal intensity. Unlike deoxygenated blood, oxygenated blood has susceptibility close to that of the surrounding tissue, it does not disrupt the magnetic field as much as deoxygenated blood. MR signal intensity increases with increased oxygenation of the blood.

It is important to understand a chain of events from task to fMRI because fMRI measures the vascular hemodynamic response induced by increased neural activity. Figure 2.13 shows a schematic of fMRI signal changes induced by stimulation.

Stimulations induce synaptic and electric activities at localized regions trigger an increase in CBF, CBV, and $CMRO_2$. In addition, it increases CMRglu (cerebral metabolic rate of glucose) which is a good indicator of neural activity. Increase in CBF enhances venous oxygenation level, while increase in $CMRO_2$ decreases venous oxygenation level. The increased oxygen extraction result in a shortly increase in the deoxyhemoglobin. This should give rise to a short decrease in the MR signal. The initial dip is thought to correspond to a phase lag between the increased oxygen utilization by the parenchyma and the vascular response of increased blood flow. This results in an initial increase in deoxygenated blood and a decrease in the BOLD signal. After a short delay, total venous oxygenation level increase due to an increase in CBF that exceeds the increase in $CMRO_2$. The increased venous oxygenation level makes T_2^* relaxation time longer even though an increased CBV slightly decrease T_2^* relaxation time. Consequently fMRI signal intensity increases during the task.

2.2.1.2. Current challenges in BOLD contrast

Although BOLD-based fMRI is widely used, several limitations exist that impede absolute determination of functional activity from the fMRI signal. These challenges include venous contribution of the signal, bulk magnetic susceptibility signal losses and distortion, hemodynamic delay, and indirect coupling to the neuronal response. Functional maps based on BOLD contrast can be significantly distant from the actual site of neuronal activity [43-45]. It relies on changes of the local magnetic field within large vessels (arteries and veins) as well as within in microvessels (arterioles, capillaries, venules), and in the surrounding tissue. Changes in blood oxygenation at the site of

activation can result in apparent activation in veins that drain blood from the activated areas, often resulting in detection of signal in regions distal to the actual area of activation [46]. The venous contribution results in a loss of spatial specificity and spatial resolution of the BOLD response. BOLD-based fMRI is acquired with contrast that reflects the magnetic susceptibility signal from the relative ratio of deoxy/oxy hemoglobin. BOLD imaging is weighted to measure the resulting T_2^* changes. However, the long TE times used to get adequate T_2^* decay resulting from the oxygenation changes in the blood also result in signal loss in tissues near air cavities [47]. This signal loss often precludes the acquisition of fMRI data in regions that are of considerable interest for functional studies, such as the orbitofrontal cortex and inferior temporal regions. In addition, this magnetic susceptibility artifact becomes more severe at high magnetic fields. Lastly, it is difficult to acquire high temporal resolution even if functional images can be obtained rapidly because hemodynamic responses are relatively slow [48-51]. Typically, hemodynamic signal changes are observed at 1-2 seconds after onset of neural activation and reaches maximum at 4-10 seconds. However, it is not easy to measure the exact time of neural activity from hemodynamic responses since hemodynamic response varies regionally.

2.2.2. Cerebral blood flow based fMRI

Perfusion is a fundamental physiological parameter, which is the delivery of oxygen and nutrients to tissues by means of blood flow. Tissue perfusion is measured using a diffusible tracer that can exchange between the vascular compartment and tissue. This yields a perfusion measurement in units of milliliters of blood flow per gram of tissue per unit time (ml/g/min). Cerebral blood flow measurements using ^{15}O-labeled

water as an exogenous positron emission flow tracer have been used extensively for functional study. Similarly, perfusion-based fMRI can be used to noninvasively measure perfusion using arterial blood water as an endogenous contrast agent.

2.2.2.1. Cerebral Blood Flow

ASL is a subtraction technique where two successively acquired images are subtracted, one with and one without proximally labeling arterial water spins (Figure 2.14). The perfusion contrast is induced by the exchange of these labeled spins with spins within the microvasculature and tissue of interest [52-56]. To accomplish this, the longitudinal magnetization of arterial blood water must be manipulated so that it differs from the tissue magnetization. The difference of the two images (control and tag) is directly related to CBF, and relative CBF changes due to physiological perturbations can be measured. Most of the labeled water molecules (~90%) are extracted into tissue while the remaining labeled water will have lost most of its label by the time it reaches the venous system. Unlike BOLD contrast, the perfusion-based signal originates predominantly from tissue/capillary.

Currently, ASL methods can be classified into two categories: continuous arterial spin labeling (CASL) techniques and pulsed arterial spin labeling (PASL) techniques as shown in Figure 2.15 [57-60]. CASL uses long RF pulses in combination with a slice selection gradient to adiabatically invert the arterial magnetization because it flows through a plane in arteries in the neck. However, the application of long off-resonance RF pulses can generate magnetization transfer effects [54,56]. CASL is usually limited to single-slice perfusion imaging in spite of efforts to solve these magnetization transfer

effects. In PASL, a short RF inversion pulse is used to produce a bolus of labeled magnetization at a tagging location proximal to the slice of interest. The RF pulses must be short in duration compared to the T_1 of blood. After a period of time TI (Inversion time) after the initiation of RF tagging pulse, the tag image is acquired of the region of interest, which represents a mixture of the pre-existing magnetization in the ROI and the magnetization of the tagged blood that has flowed into the ROI.

Compared to relatively venous-weighted BOLD methods, ASL has higher inherent spatial resolution. This results in greater anatomical specificity of brain activation as compared to BOLD imaging [61-65].

2.2.2.2. Current challenges in CBF contrast

One of the biggest disadvantages of ASL method is its intrinsicly low SNR [66-69]. The small blood volume fraction of a voxel limits the signal to noise ratio. A typical functional change in the acquired ASL signal is often on the order of 1% or less. In addition, the ASL method requires image subtraction to obtain blood flow information leading to increased noise levels in the perfusion images. ASL temporal resolution should be superior to that of BOLD contrast and its signal reflects primarily the vascular response of the capillaries as mentioned earlier. However, the sample rate for perfusion images is lower than BOLD because of the pair-wise subtraction of tagging and control pulses and the need to wait for recovery of transverse magnetization. In addition, ASL techniques usually have less imaging coverage because T_1 limits the time available for multi slice acquisition before the label decay. There are a number of systematic

confounding factors such as transit delay, magnetization transfer and relaxation artifacts that impact the ASL studies.

2.3. pH-sensitive Magnetic Resonance Methods

The ability to non-invasively measure pH dynamics in vivo provides unique insight into better understanding brain function as well as neurological and psychiatric disorders. Various magnetic resonance (MR) approaches have been developed to measure brain pH with pH-dependent chemical shift changes using MR spectroscopy, pH-sensitive contrast agents, proton exchange properties, and by combining paramagnetic contrast agents with proton exchange.

2.3.1. Magnetic Resonance Spectroscopy

Magnetic resonance spectroscopy (MRS) complements magnetic resonance imaging (MRI) as a non-invasive means for the characterization of chemical compositions in tissue. The presence of electrons surrounding the nucleus has a shielding effect against the external main magnetic field and causes the additional local field changes the effective field sensed by the nucleus. The local magnetic field that is actually experienced by the nucleus relies on the chemical structure of molecules. Different chemical environments enable the nucleus to resonate at slightly different Larmor frequencies. For example, the terminal phosphorus nuclei of all ATP molecules in the same tissue compartment resonate at nearly the same frequency, because they all experience similar shielding from the main magnetic field by intra-molecular distortions of electron clouds due to the molecule's other two phosphorus nuclei and its protons. In

contrast, the α and β phosphorus nuclei have different resonant frequencies from the terminal phosphorus and from each other due to their different chemical environments. The shielding effect on nuclear resonant frequency is called the chemical shift. Therefore there are some frequency peaks in the MR spectrum from multiple spin systems with different resonant frequencies due to their different chemical structures. MRS uses these peaks to quantify the concentration of brain metabolites such as N-acetyl aspartate (NAA), choline (Cho), creatine (Cr) and lactate in the tissue examined. MRS is based on the fact that resonant frequencies of nuclear precession can be detected from ^{1}H, ^{31}P, ^{13}C, ^{15}N, ^{23}Na, ^{17}O, and several other magnetic nuclei.

2.3.1.1. Proton/Phosporous Spectroscopy

Magnetic nuclei other than ^{31}P can assess pH changes from biological tissues. The ^{1}H MRS includes signals from several compounds with strong signals sensitive to pH [70-72]. Lactate is one of the good candidates as an indicator of pH in brain [36,73-78]. For example, cerebral intracellular acidosis following brain injury may be caused by accumulation of acidic metabolic intermediates such as lactate [79,80]. Figure 2.16 shows the dynamic changes in brain lactate levels and pH in vivo following fluid-percussion brain injury of graded severity in the rat. Figure 2.16A shows the changes of intracellular pH after the trauma by using ^{31}P MRS. The early acidosis (40min.) was followed by alkalosis 2-4hrs after injury. Figure 2.16B shows the change of intracellular brain lactate concentrations by using ^{1}H MRS. A significant correlation is observed between brain lactate level and pH for all injury levels as shown in Figure 2.16C.

In addition to the lactate, the ^{1}H signal from carnosine and homocarnosine which are concentrated in brain tissues has been used to measure pH in the human brain and gave values quite similar to Pi in the ^{31}P MRS. While pH is usually determined by the frequency difference between Pi and PCr in the ^{31}P MRS, the aromatic signals of histidine in the carnosine molecules observed in ^{1}H MRS can be used to determine the pH by ^{1}H MRS. These signals are the aromatic imidazole ring for which the two protons on C-2 and C-4 (Im_C2 and Im_C4). Two resonances of histidine were clearly identified in the proton spectra, and by using their pH-dependent chemical shifts the pH was estimated [81]. Figure 2.17 shows three baseline subtracted spectrum that are obtained before, during, and after hyperventilation. The histidine Im_C2 resonance shift to higher field during hyperventilation and returned to the normal chemical shift position after hyperventilation. The pH increases during hyperventilation and decrease slowly after hyperventilation. However, homocarnosine and carnosine of ^{1}H MRS has a narrow chemical shift range, and is therefore limited in its precision. The homocarnosine titration curve is shown in Figure 2.18 for comparison with the ^{31}P MRS indicators mentioned above. MgATP and PME are less precise because their pKs are farther from the physiological pH range. Unlike the signals mentioned above, Pi is the best of the ^{31}P indicator for assessing pH changes because its signal is large and narrow, and its pK is near intracellular pH of brain [14].

It is possible to measure pH of brain tissue by ^{31}P MRS because the resonant frequencies of particular nuclei in some compounds are impacted by changes in the pH of the tissue compartment containing them [14,82-84]. Measurement of pH depends on detection of the chemical shift of the conjugate acid and base forms of some compounds

used as a pH indicator. If protons exchanged between the base and acid forms rapidly relative to the duration of the NMR measurements, just one signal is detected. However, if the two forms exchange protons at a rate that is slow relative to the duration of the NMR measurement, separate signals from each are observed. The ratio of their intensities can be substituted for the base/acid concentration ratio in the Henderson-Hasselbalch equation [85].

$$\mathrm{pH} = \mathrm{pK} + \log\left(\frac{[\mathrm{base}]}{[\mathrm{acid}]}\right) \tag{2.26}$$

For an observed chemical shift (δ) comprised of a weighted average between the shift of a pure base (δ base) and that of its conjugated acid (δ acid), the Henderson-Hasselbalch equation is rewritten as

$$\mathrm{pH} = \mathrm{pK} + \log\left(\frac{(\delta - \delta\ \mathrm{acid})}{(\delta\ \mathrm{base} - \delta)}\right) \tag{2.27}$$

In brain tissue, although several other metabolites detectable by MRS have resonant frequencies sensitive to pH, such as γ-ATP, phosphorylethanolamine, fructose phosphates, and glucose phosphate, Pi is the best NMR indicator of pH, for two reasons: (1) NMR-detectable concentrations of Pi are usually present. Its component conjugate acid ($H_2PO_4^-$) and base (HPO_4^-) are sufficiently concentrated for both to influence the weighted average of the Pi signal. (2) The pK of this dissociation is 6.77, which places the most sensitive part of its titration curve in a range of principal biological interest. Thus, for NRM measurements of pH based on dissociation of phosphoric acid, the Henderson-Hasselbalch equation is written as

$$pH = pK + \log\left(\frac{(\delta Pi - \delta\, H_2PO_4^-)}{(\delta\, HPO_4^{2-} - \delta Pi)}\right) \quad (2.28)$$

$$H_3PO_4 \rightleftharpoons H^+ + H_2PO_4^- \quad (2.29)$$

$$H_2PO_4^- \rightleftharpoons H^+ + HPO_4^{2-} \quad (2.30)$$

$$HPO_4^{2-} \rightleftharpoons H^+ + PO_4^{3-} \quad (2.31)$$

where δPi is the observed chemical shift of the concentration-weighted average signal from $H_2PO_4^{1-}$ and HPO_4^{2-}, and $\delta H_2PO_4^{1-}$and δHPO_4^{2-} are the chemical shifts of the pure compounds known from separate measurements. Figure 2.19 shows stimulated normal ^{31}P MRS of brain and changes that occur in hypocapnia alkalosis, hypercapnia acidosis, and acidosis with energy failure in ischemia. Since most Pi is in cytosol, the signal principally reflects the pH of intracellular compartments.

The normal ^{31}P MRS is represented at top left, with the region containing the (boldface) signal from phosphate (Pi) expanded on the right. The other signals are from phosphocreatine (PCr), α, β and γ phosphates of ATP, and compounds with phosphomonoester (PME) and phosphodiester (PDE) groups. In hypocapnia alkalosis, the Pi signal shifts to the left. In hypercapnia acidosis, the Pi signal shifts in the opposite direction. In addition, Pi signal intensity rises and PCR intensity falls, due to concentration changes caused by the effect of acidosis on the creatine kinase equilibrium. In ischemia severe enough to cause loss of tissue energy stores and disruption of cell membranes, Pi may be the only signal remaining, shifted far in the acid direction, as shown in Figure 2.19.

2.3.1.2. Potentials and Challenges for Spectroscopy

Although many MRS works on brain pH have continuously achieved new understanding of how pH is related to brain function and disease in the nervous system, MRS methods have many limitations. The first reason is the heterogeneity of Pi distribution among brain cells. Distribution of the Pi signals from ^{31}P MRS across tissue compartments is exceptionally important for interpretation of pH values which are inferred from a single sample averaged over volumes of complex tissue that are large compared to cell size. Therefore, pH measurement by MRS would be difficult to achieve the anatomical selectivity or spatial resolution of pH micro electrodes. In ^{1}H MRS, a longer TE should be used to eliminate of fast decaying components because histidine signal at ~7.8ppm contains at least three contributions. However, SNR is reduced due to the use of long TE and hence a less accurate pH estimation. Furthermore, ^{1}H MRS for in vivo pH measurement should be conducted by using oral loading of histidine because histidine concentrations are low for credible measurement. Other limitations include slow temporal resolution (~tens of minutes), low spatial resolution, and accurate shimming.

2.3.2. Magnetization Transfer

Magnetization transfer imaging (MT) is based on the magnetization interaction, through chemical exchange between unbound water protons (free water protons) and macromolecular protons (Figure 2.20.). Examples of protons bound to macromolecules are those in hydroxyl (-OH) groups in white matter lipids and proteins, and examples of unbound protons include those in free water molecules in cytosol. This distinction defines

two pools of protons in the body. The first pool is called the restricted pool and the second pool is called free pool.

Conventional MRI is based on the contrast of T_1, T_2 and the proton density in tissue; it depends on free bulk water protons. These free water protons have faster rotational frequency, resulting in fewer interactions with the environment and less restricted water molecules that may cause local field inhomogeneity. Therefore, most free water protons have resonance frequencies lying narrowly around the normal proton resonance frequency, making their transverse magnetization dephasing slower and their T_2 longer (Figure 2.21). The T_2 relaxation time of the free water protons is long enough to be detectable (>10ms). In contrast, water protons bound to macromolecules have a slower rotational frequency due to extensive interactions with the protons in the local macromolecules. This creates an inhomogeneous magnetic field that leads to wider resonance frequency spectrum because the full width at half maximum of a spectrum is inversely related to the transverse relaxation time. This results in faster dephasing of magnetization and a much shorter T_2 (<200μs). Therefore, water protons bound to macromolecules with short T_2 are not typically detected in MR images obtained with conventional TE times.

However, using an off-resonance pulse excitation to saturate water protons in the restricted pool can have a detectable effect on MR signal from the free pool. After applying off-resonance pulse, the transverse magnetization created in rapidly dephased and the longitudinal magnetization requires some time to return to equilibrium. The saturation of longitudinal magnetization of protons in the restricted pool is in turn transferred to the longitudinal magnetization of protons in the free pool by a process

called magnetization exchange. The result is an increase in the T_1 of protons and reduced signal from the protons in the free pool. With MT, the presence or absence of macromolecules can be seen.

Figure 2.22 shows the exchange of longitudinal magnetization between restricted protons bound to macromolecules and free water protons. Figure 2.22A diagram shows macromolecular protons (H), including hydration layer protons and free water protons. Off-resonance RF pulse (black arrows) saturates the restricted macromolecular protons (unsaturated protons are designated H, while saturated are designated H) in Figure 2.22B. In Figure 2.22C, saturation is transferred to hydration layer protons (…H). Saturated protons diffuse into the free water proton pool and decrease the signal from this pool as shown in Figure 2.22D.

Protons in some tissues such as blood, cerebral spinal fluid, and fat undergo almost no magnetization exchange with the restricted pool. However, protons in other tissues such as white matter, cartilage, muscle, and liver display stronger magnetization exchange, thus their signal can be reduced by 20-50% or more by adding an MT pulse to the sequence. The MT effect is described by the magnetic transfer ratio (MTR) that can be written as

$$\mathrm{MTR} = 1 - \frac{\mathrm{M_{sat}}}{\mathrm{M_0}} \tag{2.32}$$

where Msat is the saturated magnetization and M_0 is the steady state magnetization. Plotting the MTR amplitude as a function of the frequency offset of the saturating RF pulse produces the Z-spectrum. The Z-spectrum associated with macromolecules in tissue is slightly asymmetric around the free water resonance peak. This MT asymmetry is

considered to be due to chemical shift center mismatch between the free water and macromolecules in tissue.

2.3.2.1. Chemical Exchange Saturation Transfer and Amide Proton Transfer

Chemical exchange saturation transfer (CEST) imaging is a particular type of MT imaging, which is focused on measuring chemical exchange between solutes and free water; the chemical exchange effect depends on proton concentration (pH) and thus it can provide a method of measuring pH in vivo. CEST occurs when saturation is applied at the frequency of the solute protons and therefore is usually detected by examining asymmetries in the Z-spectrum to balance the effects of direct saturation of the water peak on the Z-spectrum.

Amid proton transfer (APT) imaging employs the CEST mechanism to detect mobile endogenous proteins and peptides [86-94]. The amide protons resonance peak resonates at 3.5 ppm downfield from water resonance peak. APT contrast reflects the relative changes in pH, the amount of exchangeable amide protons of protein and water content [95,96]. The amide proton transfer ratio (APTR) can be measured as MTR asymmetry of the Z-spectrum at ± 3.5ppm from the water peak [102].

$$\mathrm{APTR} = \mathrm{MTR}(-3.5\mathrm{ppm}) - \mathrm{MTR}(+3.5\mathrm{ppm}) = \frac{S_{sat}(-3.5\mathrm{ppm})}{S_0} - \frac{S_{sat}(+3.5\mathrm{ppm})}{S_0} \quad (2.33)$$

where Ssat and S0 are the saturated and unsaturated signal intensities respectively. As the proton exchange rate is proportional to the change in pH [97,98]. APTR has been

proposed as a means to image intracellular pH changes in the brain [99]. In protein solutions, the signal intensities and line widths of the amide proton resonances depends on the hydrogen exchange rates. This exchange rate is base-catalyzed for pH value above ~5, thus is proportional to the hydroxyl ion concentration and exponentially proportional to pH.

Asymmetry in Z-spectrum in the amide group region has been shown to change during acute ischemia [99]. This change can be seen as the difference in APTR (=MTRasym) between the ischemic (ipsilateral) and the normal (contralateral) sides of the brain as shown in Figure 2.23. Comparison of the MTRasym spectrum between ischemic and contralateral regions shows a reduction in intensity for the 2-5ppm offset range. The area of ischemia (arrow) visible on the right side of the images is located in the caudate nucleus. In the T_2 weighted image (Figure 2.23(a)), no effect of ischemia is visible. However, the MTRasym image (Figure 2.23(c)) shows the ischemic region, as confirmed by the diffusion weighted image (Figure 2.23(b)). Imaging of MTR shows a strong negative effect in the caudate nucleus. To calibrate the exchange-rate changes in terms of pH change, ^{31}P MRS was used to determine intracellular pH values (Figure 2.23(d)). This is valid assuming that the inorganic phosphate species used in ^{31}P MRS experiences that same intracellular environment as amide protons. Using the fact that amide proton exchange is predominantly base-catalyzed, it can be derived that:

$$k = k_{base}\,[OH] \;=\; k_{base} \times 10^{pH-pK_w} = 5.57 \times 10^{pH-6.4} \qquad (2.34)$$

The base-catalyzed exchange rate (Kbase) can be obtained by fitting the exchange rate versus pH, using pKw =15.4 at 35°C [100]. Zhou et al. derives the equation APTR=5.73 X $10^{PH-9.4}$ [99].

2.4.2.2. Potentials and Challenges for Chemical Exchange Saturation Transfer/Amide Proton Transfer

CEST/APT imaging has shown pH-sensitive MRI contrast by using the chemical exchange between free water molecules and endogenous proteins and peptides. However, APT imaging is dependent on experimental parameters such as the shape, duration and power of the off-resonance RF pulse, thus it is important to optimize the experimental conditions for credible CEST/APT imaging because of their small contrast [89,90,101-104]. In addition, there are other factors affecting pH, such as temperature and the sensitivity to B_1 and B_0 inhomogeneities that would degrade an accuracy of pH measurement [89]. Furthermore, these techniques have been limited to acquiring single slices of image data. This limitation is largely a factor of the very long continuous wave RF irradiation required to reach the steady state for quantitative APT imaging. As a result, repeating RF excitation for each slice is a very time-consuming procedure, and thus not feasible for in vivo applications. Although CEST/APT techniques capable of acquiring multi-slices of image data are recently developed [101], the B_1 and B_0 inhomogeneities cause measurement errors and artifacts because the spatial coverage of the multi-slice CEST/APT imaging can be significantly larger than that of single-slice imaging.

2.3.3. $T_{1\rho}$ Magnetic Resonance Imaging

2.3.3.1. $T_{1\rho}$ Contrast

Several studies show pH-dependency of tissue $T_{1\rho}$ relaxation in the rat brain [105,106]. The study by Kettunen et al showed that acidification of the brain tissue by on pH unit is estimated to prolong tissue $T_{1\rho}$ relaxation [111]. In order to manipulate brain pH, rats were exposed to hypercapnia or hypoxia. Hypercapnia reduced pH which was associated with a $T_{1\rho}$ increase relative to the control level. Figure 2.24 shows the brain tissue $T_{1\rho}$ relaxation as a function of intracellular pH. The data fitted into a linear fit showing that an acidification of pH from 7.2 to 6.2 would increase tissue $T_{1\rho}$ by 7.4ms and 3.5ms in the absence and presence of AMI-227, respectively.

The extent of $T_{1\rho}$ positively correlates with the lactate concentration, suggesting that pH modulates $T_{1\rho}$ in the ischemic tissue [105]. During the evolution of ischemia, the pH drop and reduced translational motion of molecules further increased $T_{1\rho}$ relaxation. In fact, $T_{1\rho}$ immediately increase upon induction of cerebral ischemia. It may be caused by changes in tissue acidosis rather than shift of extracellular water into the cell interior. However net water accumulation might affect the change of $T_{1\rho}$ after tens of minutes. $T_{1\rho}$ relaxation in vivo could be influenced by proton exchange, cross-relaxation as well as direct contributions of protein protons, which may change in ischemic brain. Proton exchange is an acid-base catalyzed process and thus influenced by pH. Another phantom study showed that $T_{1\rho}$ relaxation in protein phantom is strongly affected by pH due to chemical exchange [34].

2.3.3.2. Potentials and Challenges for $T_{1\rho}$

$T_{1\rho}$ imaging is less sensitive to diffusion losses caused by static susceptibility artifacts compared to BOLD because $T_{1\rho}$ imaging is generated by applying a spin-lock pulse without the application of gradients, which reduce spin dephasing compared to T_2-weighted imaging [107]. In functional MR studies, the lengthy echo times used in the traditional echo planar imaging (EPI) sequence are required to maximize T_2^* BOLD contrast. This results in significant signal loss due to intra voxel dephasing in areas with large static susceptibility. Recent reports using functional MR experiments with $T_{1\rho}$ contrast suggest that $T_{1\rho}$ -weighted contrast in addition to T_2^* contrast is useful to study brain function. However, the main limitation in $T_{1\rho}$ imaging is the specific absorption rate (SAR) limits, which is the amount of RF energy per unit mass per unit time deposited into the body.

$$SAR \propto \frac{B_0 * B_1 * TSL}{TR} \tag{2.35}$$

The addition of the spin-lock pulse having low amplitude to saturate the free water protons increases SAR. Although new techniques to reduce SAR by applying the full power spin-lock pulse to only central phase-encode lines of the k-space was introduced, the application of different power of the spin-lock results in image artifacts [108]. Another concern is the uniformity of the spin-locked field, which is hard to accomplish for a head-sized target. Adiabatic excitation, combined with spin-locking pulses, is one potential way to overcome this limitation [109].

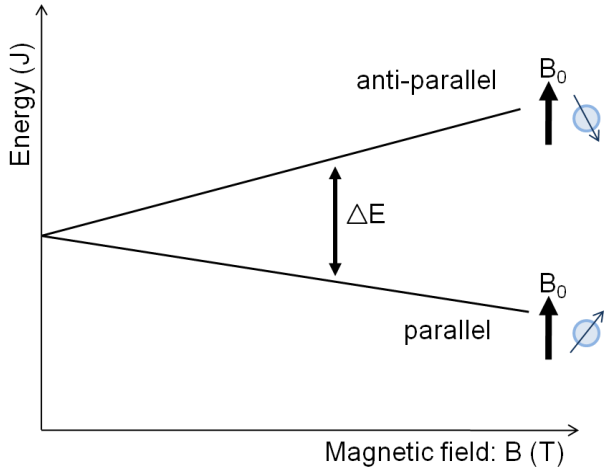

Figure 2.1. The energy of two spin-levels as a function of magnetic field strength.

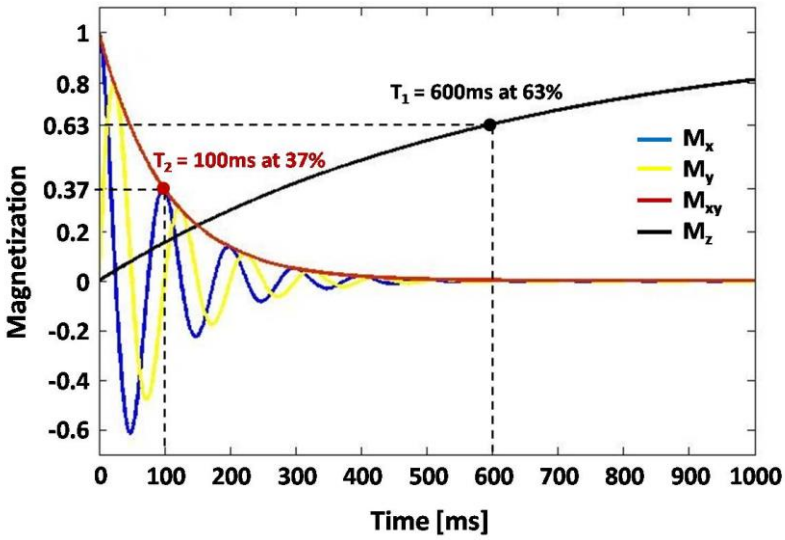

Figure 2.2. Free induction decay, T_1 and T_2 relaxation time.

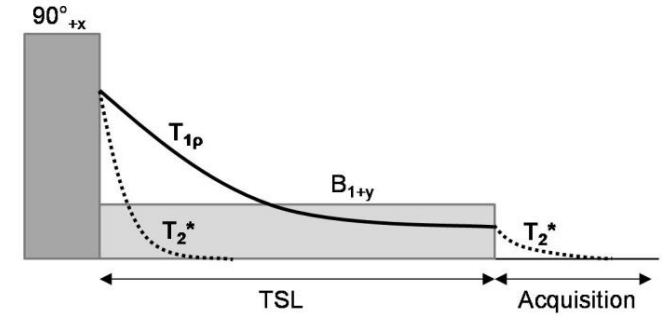

(A)

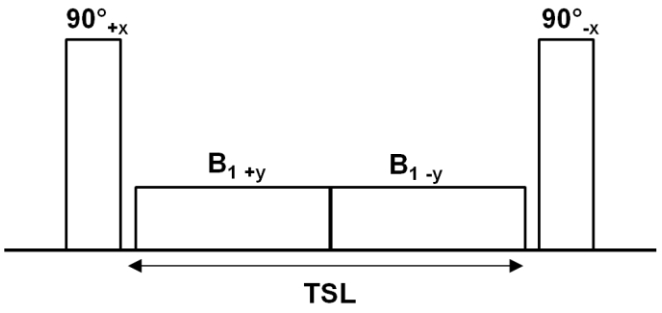

(B)

Figure 2.3. $T_{1\rho}$-weighted spin–lock RF pulse cluster. Figure 2.3A shows the $T_{1\rho}$-prepared RF pulse cluster with single phase spin-lock pulse. Figure 2.3B shows the $T_{1\rho}$-prepared RF pulse cluster with self-compensating spin-lock pulse. Non-selective RF pulses ($90°_{+x}$ and $90°_{-x}$) are used for the longitudinal magnetization to flip into the transverse plane. B_{1+y} and B_{1-y} are the spin-lock pulse. TSL is the duration of the spin-lock pulse.

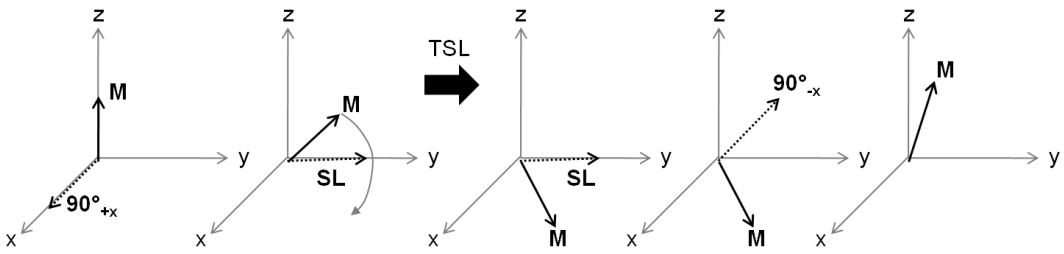

Figure 2.4. Vector diagram of the evolution of the magnetization during TSL

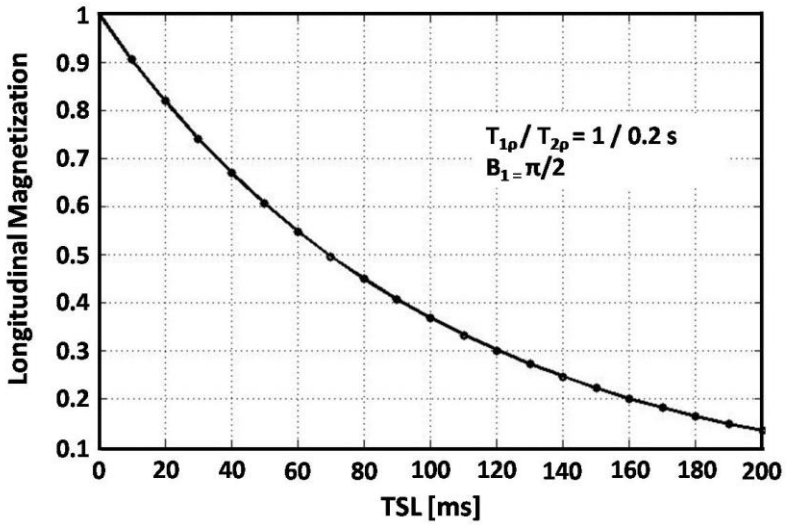

Figure 2.5. Simulated longitudinal magnetization as a function of TSL

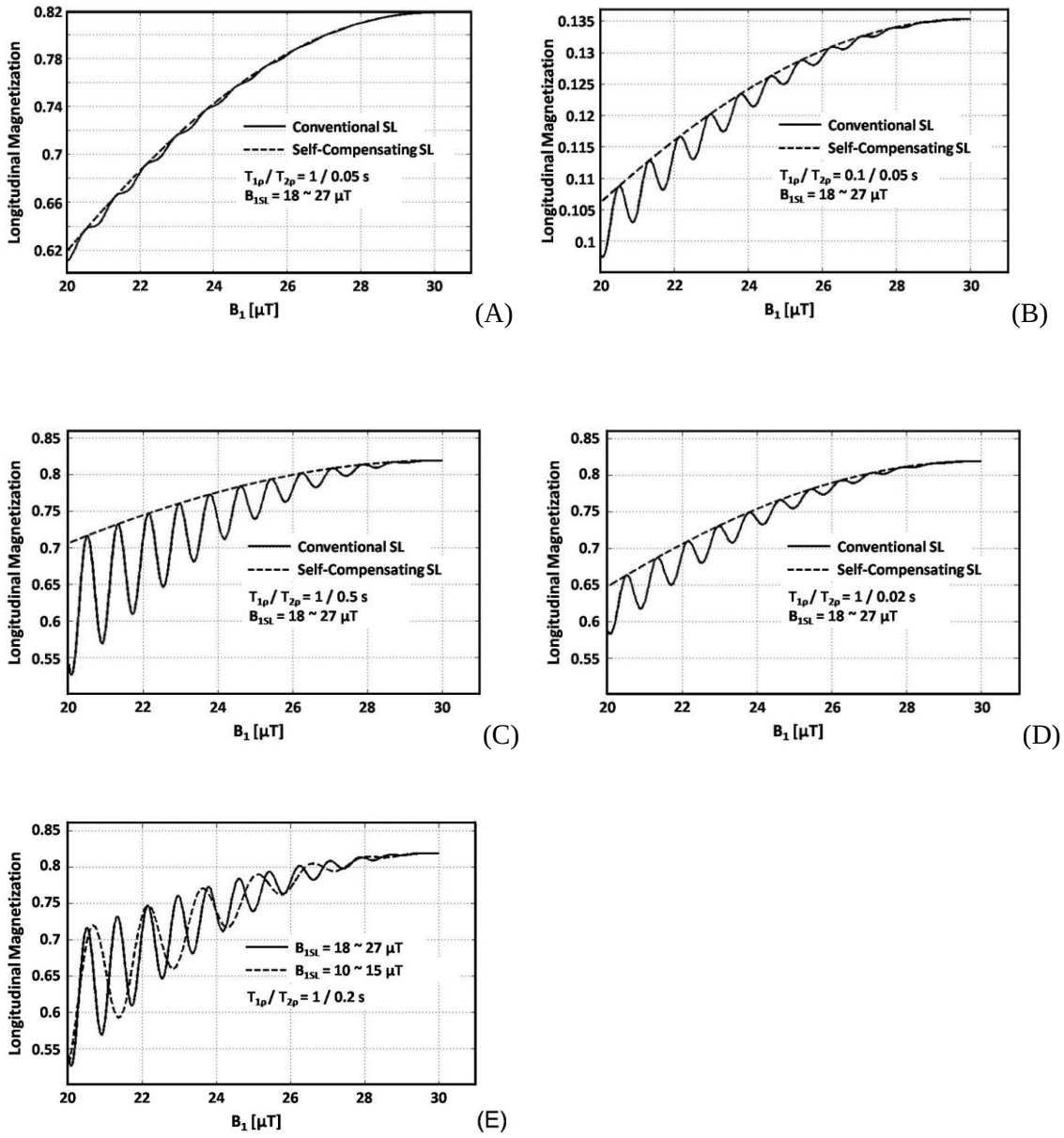

Figure 2.6. Simulated longitudinal magnetization after $T_{1\rho}$ preparation cluster as a function of B_1. B_1 is considered to vary from 20μT to 30μT (A-E). $B_{1\rho}$ is considered to vary from 18μT to 27μT (A-D). Plots (A) and (B) are for varying $T_{1\rho}$ and a fixed $T_{2\rho}$ of 0.05s. Plots (C) and (D) are for varying $T_{2\rho}$ and a fixed $T_{1\rho}$ of 1s. Figure 2.6E shows the longitudinal magnetization with different $B_{1\rho}$ range of 18μT to 30μT and 10μT to 15μT.

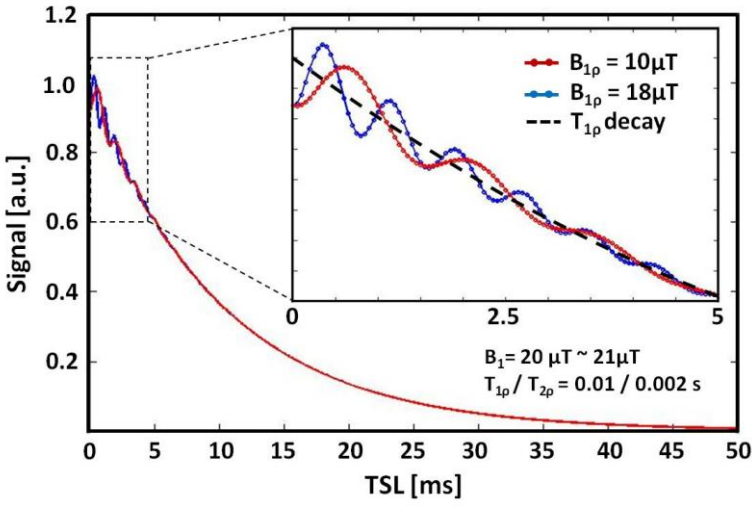

(A)

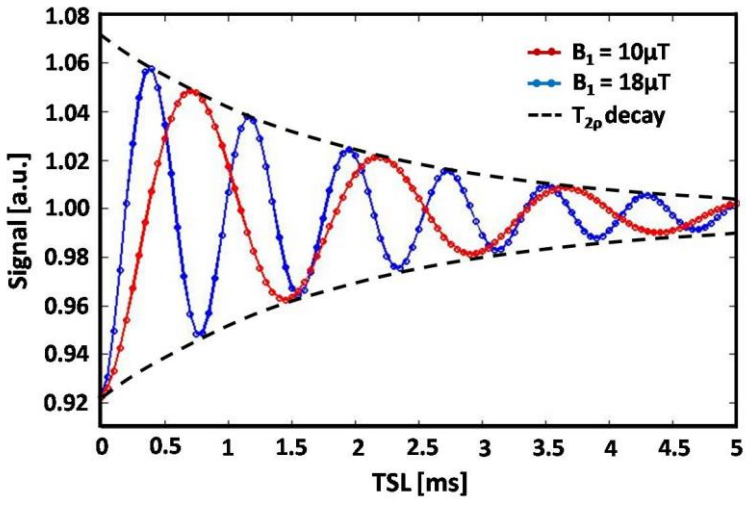

(B)

Figure 2.7. Simulated MR signal changes as a function of TSL. Shown are the oscillations, characteristic of residual dipolar interaction, $T_{1\rho}$, and $T_{2\rho}$ decay.

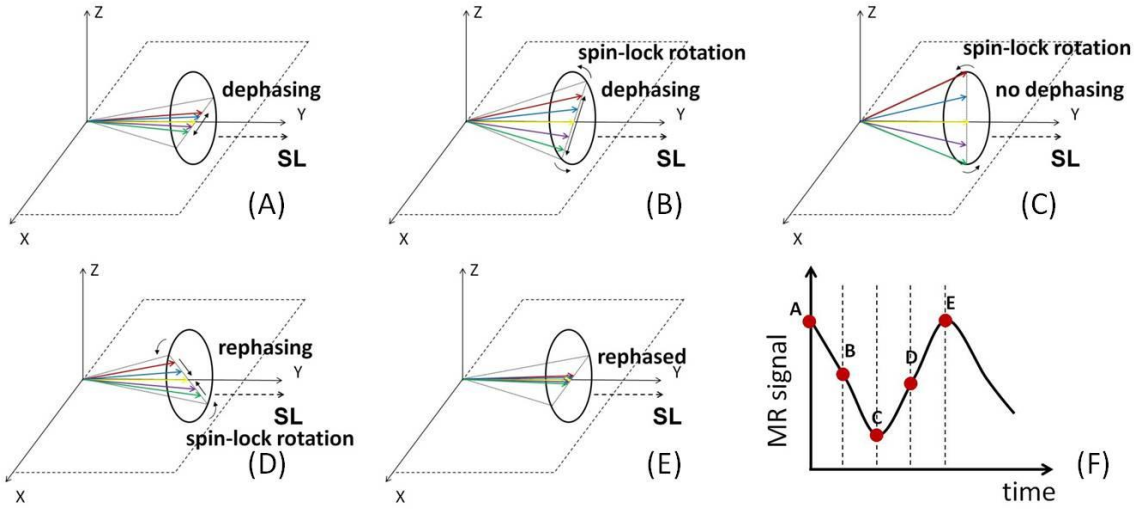

Figure 2.8. Vector diagram of the evolution of the magnetization during TSL in the presence of dephasing caused by residual dipolar interactions

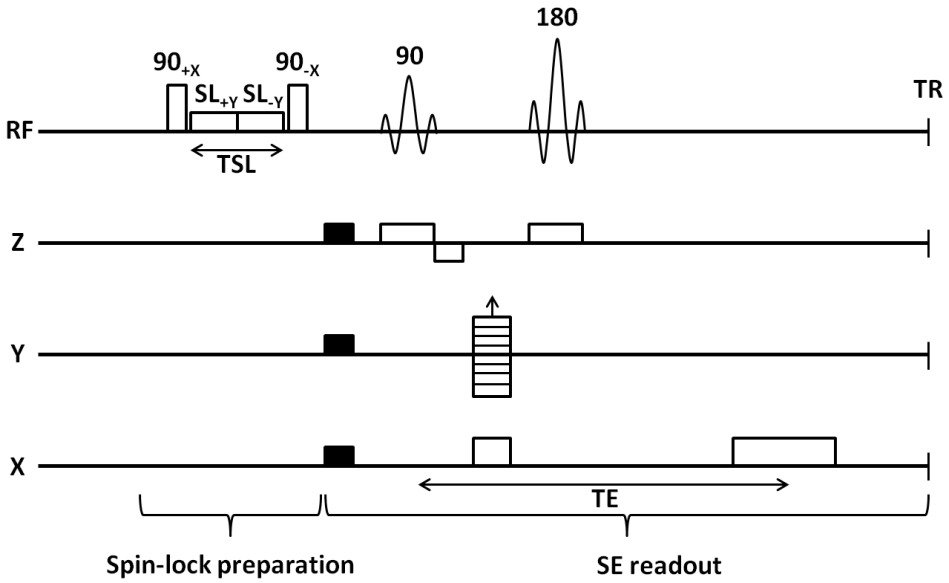

Figure 2.9. $T_{1\rho}$-weighted pulse sequence with SE readout. Two non-selective 90 pulses are separated by a pair of spin locking pulses (SL) with opposite phase. Crusher gradients (shaded) are used to destroy any residual magnetization after the spin-locking preparation period. A conventional spin-echo sequence acquires the image data.

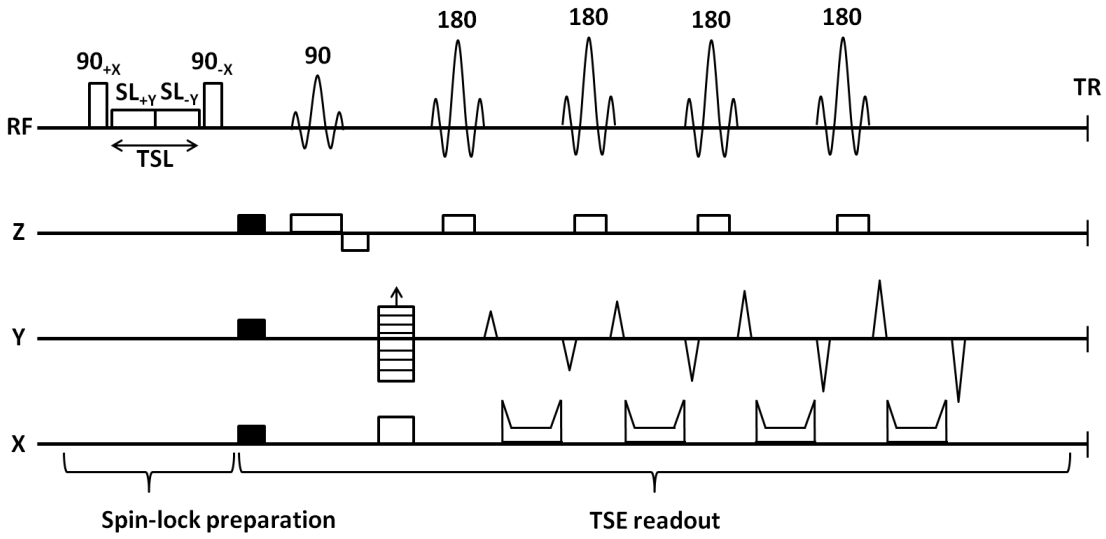

Figure 2.10. $T_{1\rho}$-weighted pulse sequence with TSE readout. An echo train length of four is display as an example. Two non-selective 90 pulses are separated by a pair of spin locking pulses (SL) with opposite phase. Crusher gradients (shaded) are used to destroy any residual magnetization after the spin-locking preparation period. A conventional turbo spin-echo sequence acquires the image data. The amplitude of the phase-encoded gradient pulses (Y) increase for each echo acquired as an illustration of centric phase-encode ordering.

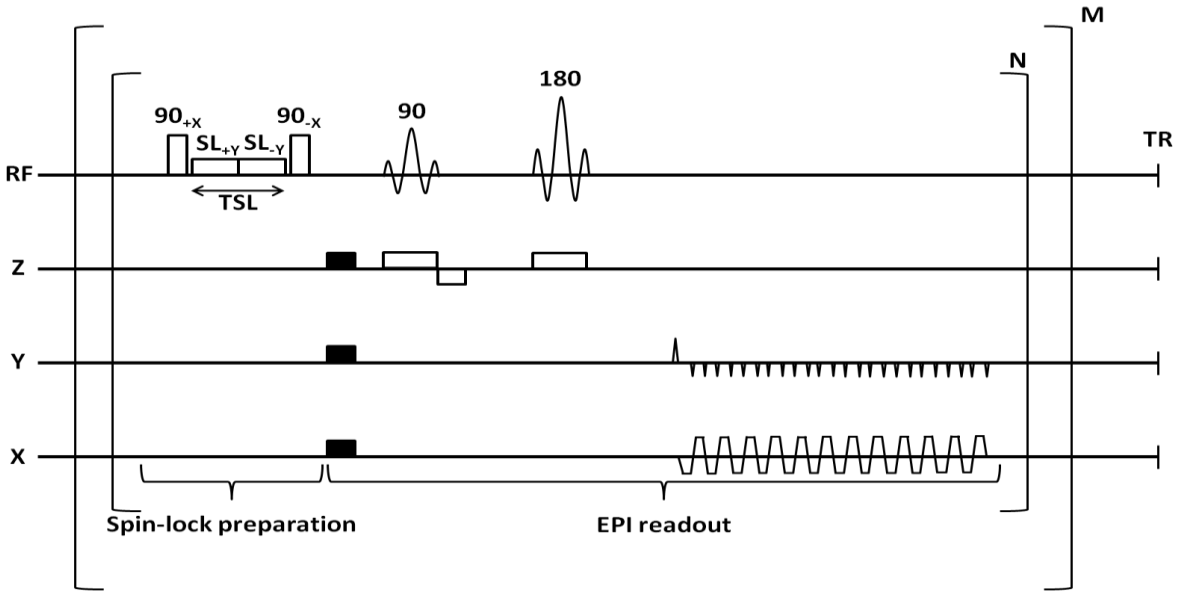

Figure 2.11. $T_{1\rho}$-weighted pulse sequence with EPI readout. Two non-selective 90 pulses are separated by a pair of spin locking pulses (SL) with opposite phase. Crusher gradients (shaded) are used to destroy any residual magnetization after the spin-locking preparation period. A conventional spin-echo EPI sequence acquires the image data. The events within the brackets are repeated N times within a given TR for the acquisition of N slices. M multiple spin-lock pulse durations can be selected.

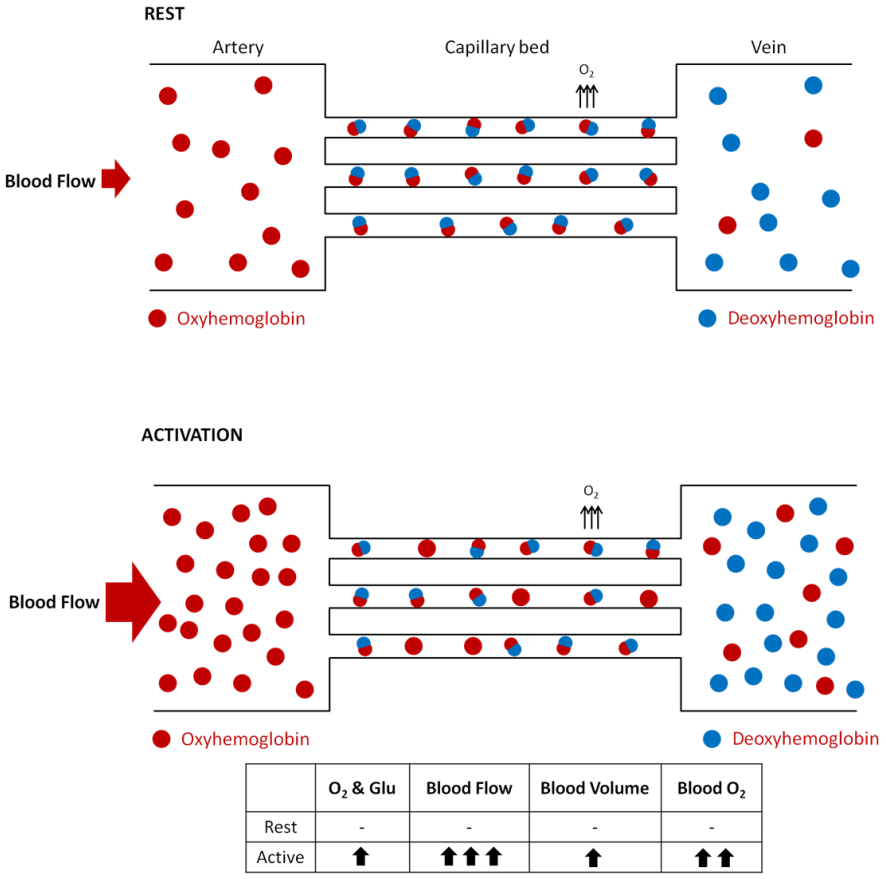

	O_2 & Glu	Blood Flow	Blood Volume	Blood O_2
Rest	-	-	-	-
Active	↑	↑↑↑	↑	↑↑

Figure 2.12. Schematic diagram illustrating BOLD. Upon activation, oxygen is extracted by the cells, thereby increasing the level of deoxyhemoglobin in the blood. This is compensated for by an increase in blood flow in the vicinity of the active cells, leading to a net increase in oxyhemoglobin

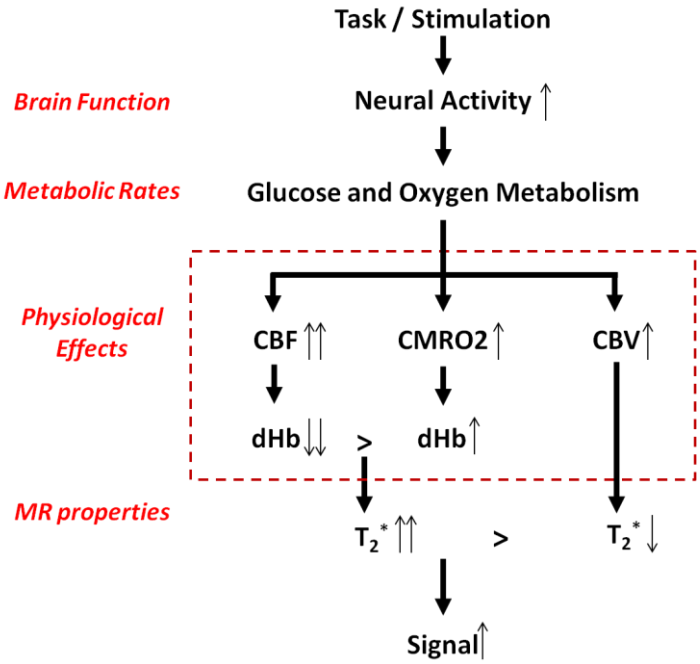

Figure 2.13. A schematic of fMRI signal changes induced by stimulation.

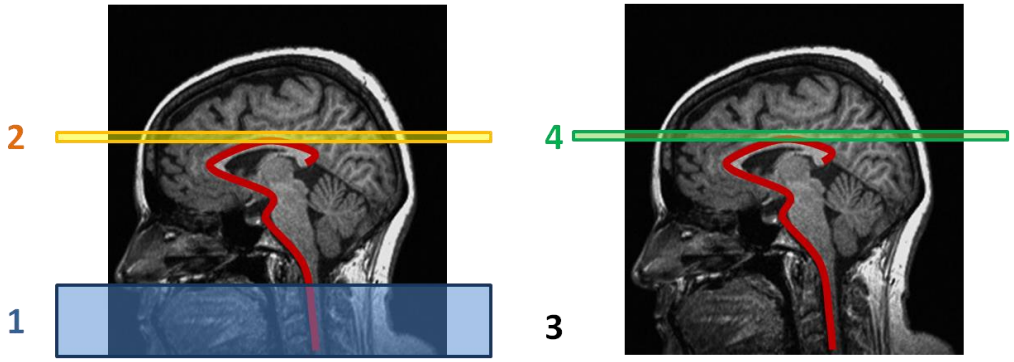

Figure 2.14. A schematic diagram illustrating arterial spin labeling. 1. Tag inflowing arterial blood by magnetic inversion RF pulse. 2. Acquire the tag image. 3. Repeat experiment without tag. 4. Acquire the control image. 5. Subtract the control image and tag image. This subtracted image reflects the amount of arterial blood delivered to each voxel within the slice within the transit time.

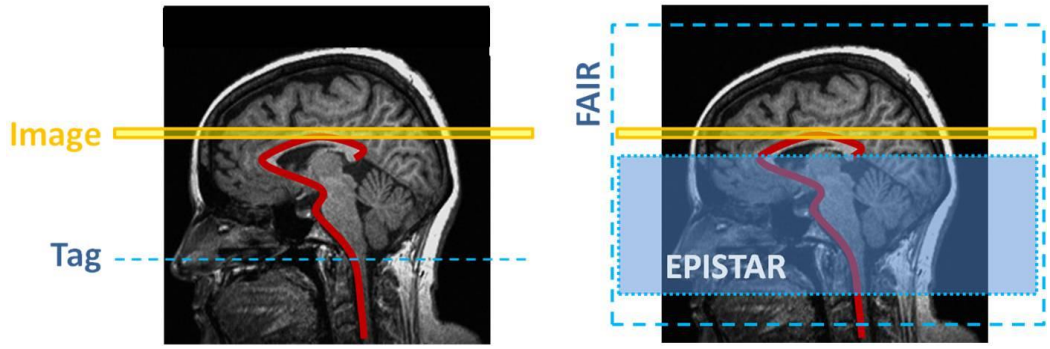

Figure 2.15. Schematic diagrams illustrating CASL and PASL. CASL (left) continuously label arterial spins using the application of a continuous RF pulse as they flow through a labeling plane. During the acquisition of the control image, as RF pulse is applied above the image slice to account for magnetic distortions caused by the pulse itself, but itself will not label any blood. PASL (right) labels arterial spins using a spatially selective labeling pulse. The RF pulse is applied in a spatially selective manner. Several versions exist, including EPISTAR (echo planar imaging and signal targeting with alternating radiofrequency) and FAIR (flow-sensitive alternating recovery).

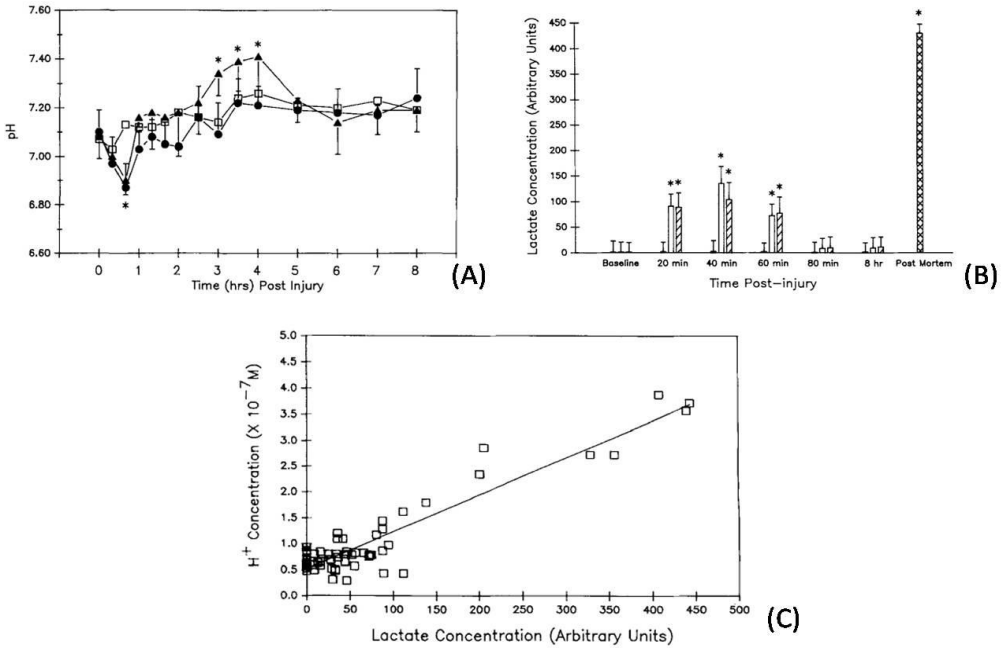

Figure 2.16. The change of lactate signal in ^{1}H MRS spectrum from the traumatic brain injury in the rat [110]. Figure 2.16A shows the changes of intracellular pH over an 8-hr period following graded traumatic fluid-percussion head injury: low-level injury (▫), moderated injury (●), and high-level injury (▲). Figure 2.16B shows the changes of intracellular brain lactate concentrations. Figure 2.16C indicates a relationship between lactate concentration and intracellular pH following graded fluid-percussion head injury in the rat.

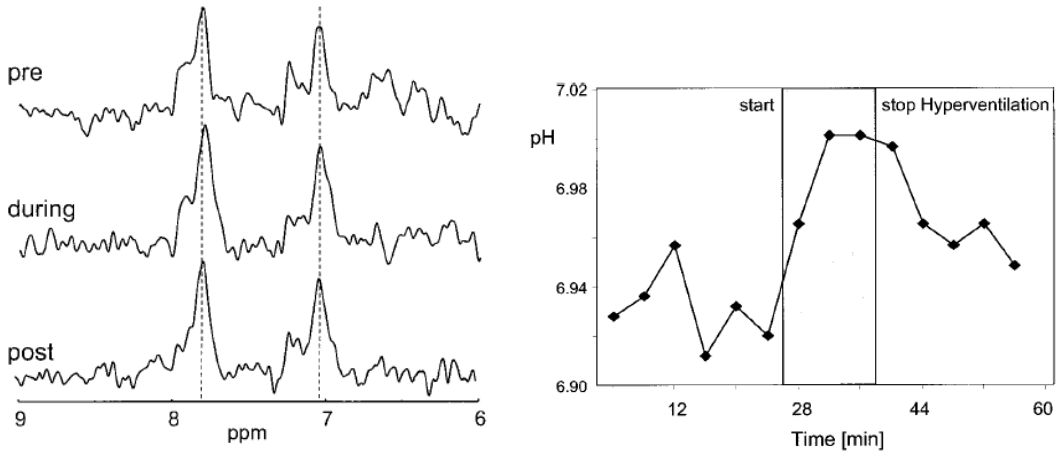

Figure 2.17. The change of the histidine Im_C2 signal in ^{1}H MRS spectrum obtained before, during, and after hyperventilation (left) [14]. pH values calculated from the chemical shift positions of Im_C2 plotted vs. time (right).

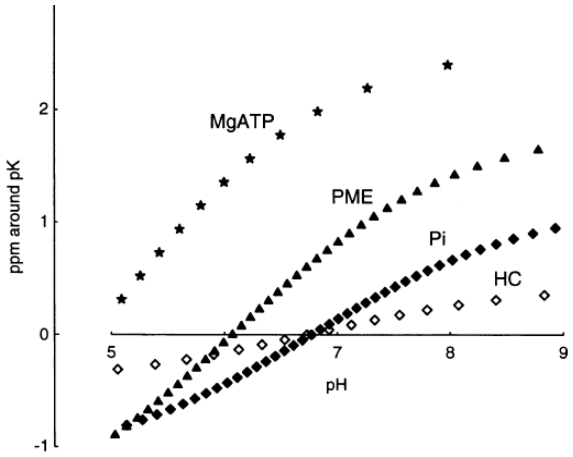

Figure 2.18. Titration curve of three signals (MgATP, PME and Pi) in the ^{31}P MRS and homocarnosine (HC) in the ^{1}H MRS [14].

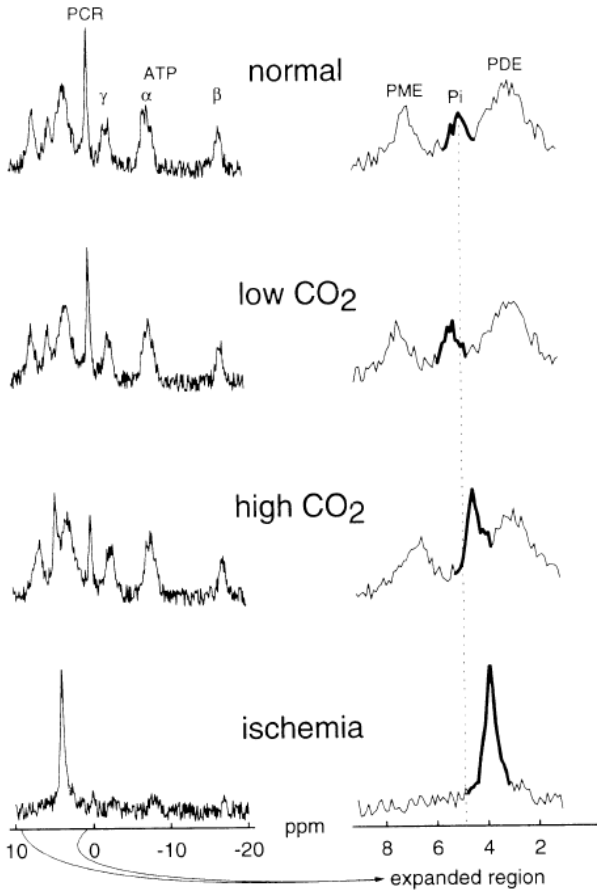

Figure 2.19. Stimulated normal ^{31}P MRS of brain and changes that occur in hypocapnia alkalosis, hypercapnia acidosis, and acidosis with energy failure in ischemia [14].

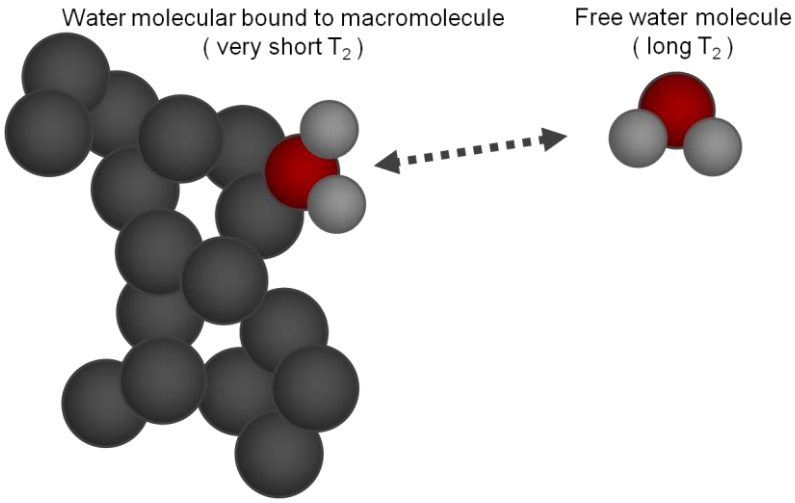

Figure 2.20. Water interactions with macromolecules

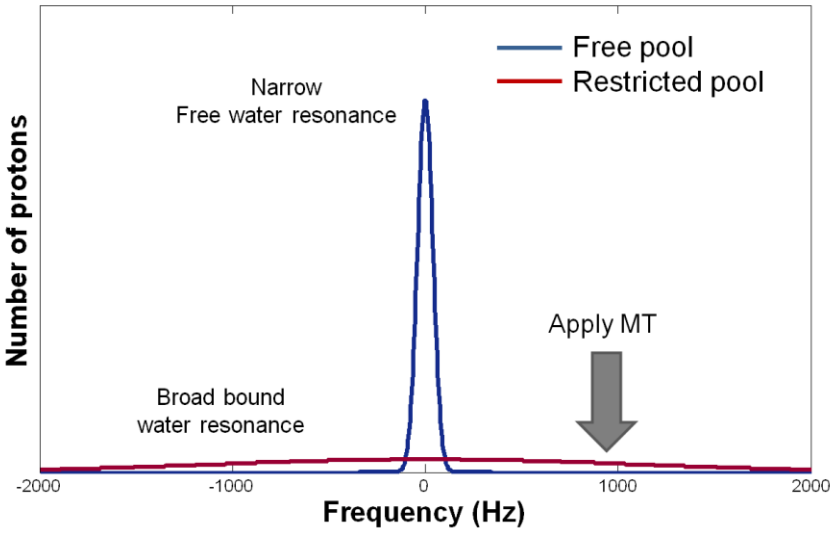

Figure 2.21. Magnetization transfer spectrum.

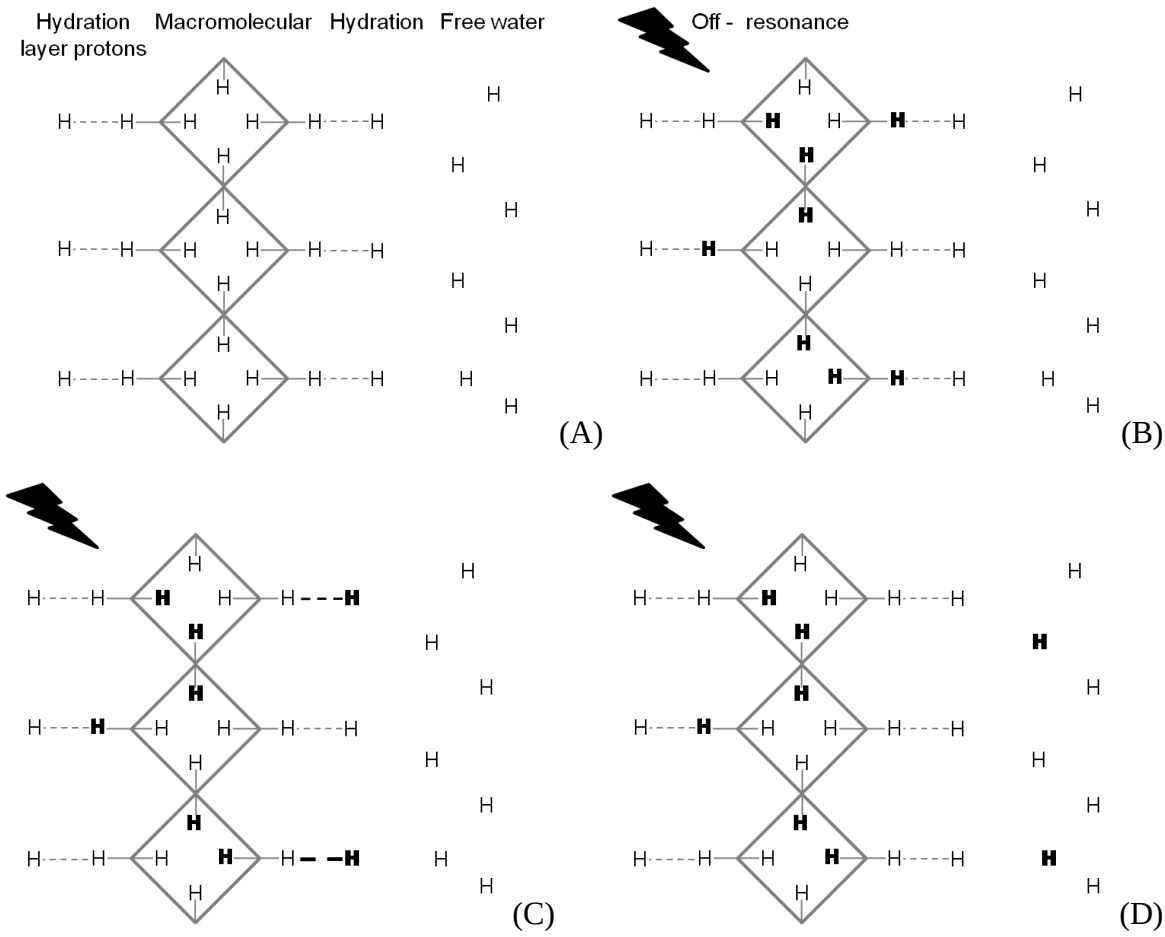

Figure 2.22. Exchange of longitudinal magnetization. Off-resonance RF pulse (black arrows) saturates the restricted macromolecular protons (unsaturated protons are designated *H*, while saturated are designated *H*)

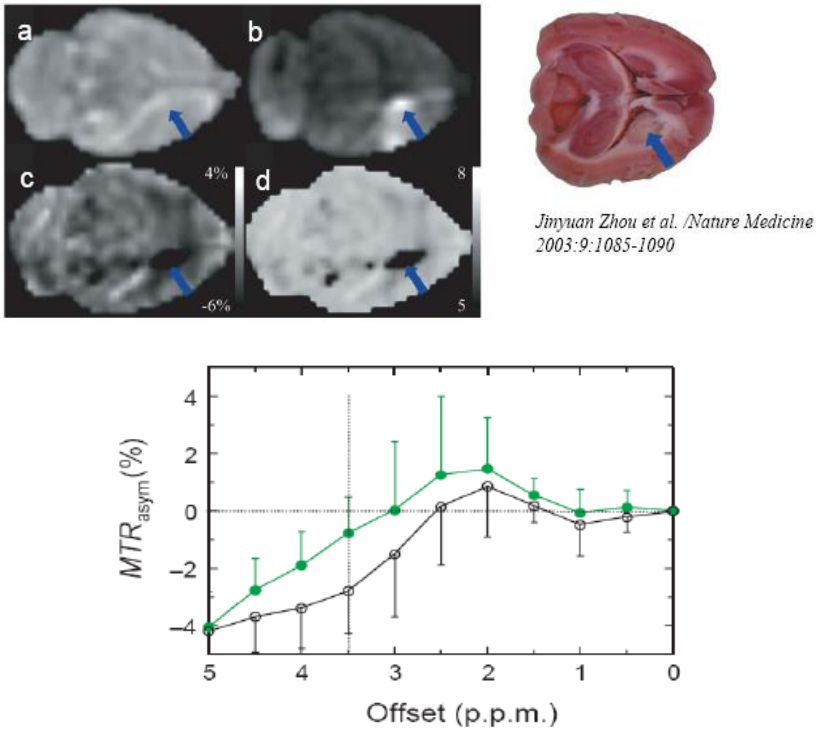

Figure 2.23. APT effects during focal ischemia in the rat brain [99]

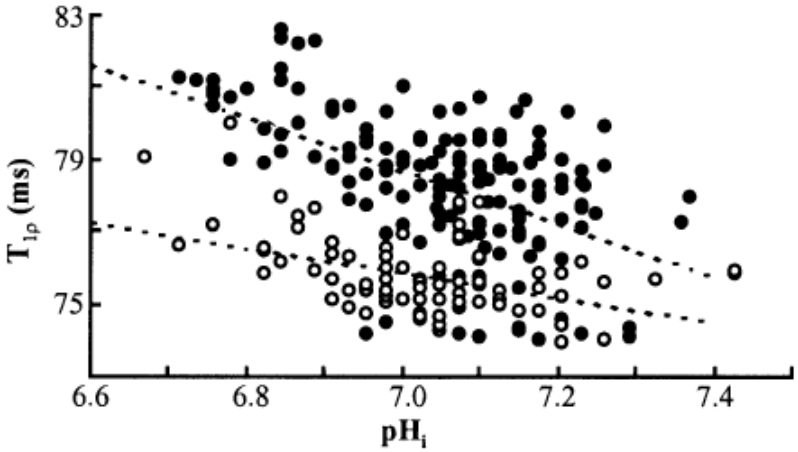

Figure 2.24. Parenchymal $T_{1\rho}$ as a function of pH [106]. The data are from the hypercapnia experiments in the presence (open symbols) and absence (closed symbols) of contrast agent (AMI-227).

CHAPTER 3

PRELIMINARY STUDIES

3.1. Validation of pH Sensitivity in Buffered Phantoms

3.1.1. Methods

This portion of the study was performed to evaluate the sensitivity of $T_{1\rho}$ for assessment of pH changes. We also wanted to investigate the relationship between the estimated $T_{1\rho}$ times and pH. The goal was to develop an imaging technique that has a relatively linear relationship between $T_{1\rho}$ times and pH within the physiological range that would be studied in vivo. Agar phantoms were prepared by dissolving 3.5% agar and 8% BSA powder in 0.1-M phosphate buffer. pH was adjusted with HCL and NaOH to create phantoms that varied from pH 6.0 to 8.0, a range extending beyond values likely to occur in vivo. A total of six phantoms (pH 6.0, 6.5, 6.7, 7.0, 7.5, and 8.0) were created in 15ml Falcon tubes. pH levels in the agar phantoms were assessed using pH paper (Micro Essential laboratory, Brooklyn, N.Y. USA, detection range pH 5.5-8, 0.2 pH unit), before and after solidification and after MR scanning.

All phantom imaging studies were acquired on a 4.7T Varian horizontal small-bore MRI scanner (Varian, Palo Alto, CA), using a volume transmit and receive Lits-cage RF coil (Doty, USA). $T_{1\rho}$ weighted images were acquired using a fast spin-echo sequence with a spin-locking preparation pulse, which created a $B_{1\rho}$ field of 1000Hz. A fast spin-echo $T_{1\rho}$ sequence was acquired through the center of the phantoms using the following parameters: TE=12ms, TR=2000ms, field of view=60x30mm, matrix size=512x128,

turbo factor=7. Four spin-lock times of 10, 20, 40, and 60ms were used. Each phantom was imaged separately, and a least squares regression analysis was used to generated $T_{1\rho}$ maps for each phantom by fitting MR signal intensity as a log-linear function of spin-lock times. A 5x5 square region of interest was placed at the center of the phantom. The mean and standard deviation of the estimated $T_{1\rho}$ signal was estimated within the regions of interest.

3.1.2. Results

Figure 3.1A shows $T_{1\rho}$ maps for the agar phantoms with different pH values. The $T_{1\rho}$ within the 5X5 voxel ROI of the 3.5% agar phantoms was 55.2ms, 50.9ms, 49.5ms, 48.3ms, 47ms, and 44.8ms for pH values of 6.0, 6.5, 6.7, 7.0, 7.5, and 8.0, respectively. $T_{1\rho}$ times were inversely proportional to the pH in the physiologic range as shown in the Figure 3.1B (R^2=0.95, relaxivity=2.07$pH^{-1}sec^{-1}$). The phantom study shows that $T_{1\rho}$ imaging is sensitive to pH changes and can be modeled linearly across the physiological range of pH.

3.2. $T_{1\rho}$ Insensitivity to Oxyhemoglobin Content

3.2.1. Methods

Blood phantom study was conducted to determine the specificity of the $T_{1\rho}$ signal to pH changes as compared to blood oxygenation changes. Fresh sheep blood was acidified with HCL, oxygenated with 100% oxygen, or remained unaltered to vary the blood pH or oxygenation respectively. pH, pO_2, and pCO_2 were measured before and

after imaging with a Radiometer ABL 5 blood gas analyzer. Each phantom was imaged individually. A single axial slice was acquired to estimate T_2^* relaxation times using a gradient-echo sequence with the following parameters: TR=2s, field of view=60x30mm, matrix size=512x128, slice thickness =1.0mm. Eight echo-times (1.7, 2, 3, 6, 9, 12, 14, and 16ms) were acquired for mapping T_2^* relaxation times. For estimation of the $T_{1\rho}$ relaxation time, a fast spin-echo sequence with $T_{1\rho}$ encoding pulse was used to acquire the same axial slice collected for T_2^* mapping. The scan parameters include TE=12ms, TR=2s, field of view=60x30mm, matrix size=512x128, slice thickness=1.0mm, TSL=10, 20, 40, and 60ms, $B_{1\rho}$ =400Hz, and turbo factor=7. A least square log-linear regression analysis was used to generate T_2^* and $T_{1\rho}$ maps. Similar to the agar phantom study, a 5x5 region of interest was placed at the center of the phantoms for estimating the T_2^* times for each condition.

3.2.2. Results

In the sheep blood phantom (Figure 3.2), the BOLD data showed sensitivity to blood oxygenation content, but was not sensitive to changes in pH of the blood. The data shows an increase in T_2^* times by 20.6ms when the blood oxygenation was changed by 624%. The T_2^* times did not change when the pH was changed between 7.12 and 6.49. Table 3.1 shows physiological variables, $T_{1\rho}$, and T_2^* measurements of blood phantoms across a pH and oxygenated spectrum. The $T_{1\rho}$ times showed sensitivity to changes in pH within the blood and were not sensitive to blood oxygenation. $T_{1\rho}$ times varied from 136±4.3ms to 173.2±2.7ms for pH values of 7.12 and 6.49 respectively. However, the $T_{1\rho}$ times did not change when the blood oxygenation was changed. This blood data shows

that there is a double disassociation between the $T_{1\rho}$ and T_2^* imaging in their sensitivity to pH and blood oxygenation.

3.3. pH Detection in Mouse Brain

3.3.1. Methods

Mouse imaging was conducted to correlate the $T_{1\rho}$ signal changes with pH changes in vivo. Simultaneous measurements were obtained from $T_{1\rho}$ imaging and a gold-standard probe implanted into mice. Four mice were anesthetized using a combination of ketamine/xylazine and placed in a stereotaxic frame. A longitudinal scalp incision was made and an acrylic head holder was secured to the cranium between the coronal and lamboid sutures. pH sensitive fiber optic electrode (pHOptica, WPI; detection range pH 5-9) implanted in the amygdala based on stereotaxic positioning of the probe. Implantation of the probe was performed twenty-four hours prior to the imaging session. Immediately prior to imaging, the mice were anesthetized using a combination of ketamin/xylazine and placed in the RF coil and then into the Varian 4.7T scanner. To evaluate the capability of $T_{1\rho}$ to detect changes in mouse brain pH, $T_{1\rho}$ images were obtained in the mice under three conditions: 1) while breathing room air, 2) while breathing 20% CO_2, and 3) following HCO_3^- injection (5mmol/kg, ip). The fiber optic sensor implanted into the amygdala was used to continuously measure brain pH during the entire experiment. The beginning and end of the imaging sessions were marked to allow the mean pH measure to be calculated during each of the imaging sessions. Imaging sessions consisted of a localizer, T_2 weighted scans to assess for blood

around the tip of the fiber optic sensor, and $T_{1\rho}$ imaging. $T_{1\rho}$ images were collected on the using a spin-echo sequence with the following parameters: TE=12ms, TR=2s, field of view =30x30mm, imaging matrix size=256x128, slice thickness=1mm, and spin-lock durations of 10, 20, 40, and 60ms. $T_{1\rho}$ maps were generated for each condition. A 5x5 region of interest was placed at the tip fiber optic probe. The mean $T_{1\rho}$ time and standard deviation was computed within this region of interest. The relationship between this $T_{1\rho}$ and the mean pH value during the imaging session was estimated from this data.

In addition, an awake mouse was imaged to correlate the $T_{1\rho}$ signal changes with pH changes in vivo to eliminate effects of anesthesia on blood flow, metabolism and neuro-vascular coupling. Furthermore we used 10% and 100% O_2 as well as 20% CO_2 to see if $T_{1\rho}$ relaxation is sensitive to the change of the brain pH, but not sensitive to the brain oxygenation level. The fiber optic pH sensor was not used in the awake mouse study. To accomplish a maximum of immobilization during scanning, we permanently affixed MR-compatible head holders to the skull of the mouse. T_2 images were acquired using the same parameters used in the anesthetized mouse study. $T_{1\rho}$ images were collected on the using a spin-echo sequence with the following parameters: TE=15ms, TR=2.5s, field of view =30x30mm, imaging matrix size=256x256, slice thickness=1mm, and spin-lock durations of 10, 20, 40, and 60ms. The mean $T_{1\rho}$ time and standard error was computed within this region of interest (174 pixels) as shown the T_2-weighted image in the Figure 3.3A.

3.3.2. Results

The T_2-weighted scans collected were visually reviewed for evidence of a hematoma before $T_{1\rho}$ imaging was performed. No evidence of a hematoma was visible in any of the mice imaged in this study. $T_{1\rho}$ maps of the mouse brain are shown in Figure 3.3A across various states including compressed air and 20% CO_2 inhalation and HCO_3^- injection. A MR compatible fiber optic pH sensor appears as a signal void on the MR images and marked with a white arrow in Figure 3.3A. The mean signal measured from the sensor during image acquisition was used to determine the relationship between pH and the estimated $T_{1\rho}$ times in the mouse. The 5x5 voxel ROI where the $T_{1\rho}$ measurements were obtained is shown with a white square in Figure 3.3A. In Figure 3.3B, the measurements obtained for each mouse are depicted using a different color and symbol. The baseline pH measurements varied from animal to animal due to variations in the respiratory rate across animals. In all cases we found that the brain had elevated pH following HCO_3^- injection as compared to the air inhalation. During the administration of 20% CO_2, $T_{1\rho}$ times were longer in the area surrounding the pH sensor indicating the region was more acidic and consistent with the lower pH detected from the sensor. This effect appeared to be linear across the range of pH values obtained in this study (pH 6.57 to pH 7.23). Figure 3.3B shows the relationship between $T_{1\rho}$ and pH measured from the fiber optic pH sensor across all four of the mice (R^2=0.77). We found that $T_{1\rho}$ is sufficiently sensitive to detect pH changes on the order of 0.1pH units or less. The data fitted into a linear fit showed that an acidification of 0.1pH units would increase $T_{1\rho}$ by 3.2ms.

$T_{1\rho}$ maps of the awake mouse brain are shown in Figure 3.4A across various states including compressed air, 20% CO_2, 10% O_2, and 100% O_2 inhalation. $T_{1\rho}$ times during breathing 20% CO_2, are significantly increased are consistent with the expected acidosis as compared to the baseline room air condition. However, the $T_{1\rho}$ times did not change when the mouse was under the hyperoxia (100% O_2) and hypoxia (10% O_2) as compared to breathing room air (Figure 3.4B). The $T_{1\rho}$ time was 63.8±0.33ms during the room air, 66.1±0.4ms during 20% CO_2, 62.4±0.4ms during 10% O_2, and 60.8±0.6ms during 100% O_2. $T_{1\rho}$ times were calculated in the ROI as shown the T_2-weighted image in the Figure 3.4A. The present study shows that $T_{1\rho}$ relaxation is sensitive to the change of the brain pH, but not sensitive to the brain oxygenation level.

3.4. Systemic pH Changes in Human Brain Induced by CO_2 and Hyperventilation

In our initial human studies, our goal was to show that brain pH changes associated with interventions known to manipulate pH would be reflected in $T_{1\rho}$ changes. In addition, we hypothesized that pH could be used as a marker for neuronal activity and that the measurement of functional pH changes can be seen using $T_{1\rho}$ imaging.

3.4.1. Methods

A single subject was recruited into an imaging study involving respiratory challenges to manipulate brain pH. MR images of the brain were obtained on a 3.0T Siemens TIM Trio scanner. $T_{1\rho}$ weighted images were acquired using a turbo spin-echo sequence with a spin-locking preparation pulse, which created a $B_{1\rho}$ field of 400Hz.

Imaging parameters were TR=3s, TE=12ms, field of view=240x240mm, imaging matrix size=128x128, bandwidth=130Hz/pixel and slice thickness=3mm. $T_{1\rho}$ maps were generated from four $T_{1\rho}$-weighted images that were obtained by varying the spin-locking times (20, 40, 60, and 80ms). To evaluate the use of $T_{1\rho}$ to detect changes in human brain pH, $T_{1\rho}$ images were obtained from a subject under three conditions: 1) breathing 5% CO_2, 2) breathing room air, and 3) hyperventilation in room air (30breaths/minute). For each condition, the subject was placed into the respiratory challenge 1 minute before imaging began and then the four spin-lock times were acquired within a 36 second window. The Biopac MRI CO_2 ($ETCO_2$) sensor was connected to the subject to measure end-tidal CO_2 during each of the conditions. $T_{1\rho}$ maps were computed for each condition and evaluated for changes within the cortical gray matter, white matter, and putamen.

To replicate the pilot study described above, a small 7.5% CO_2 and hyperventilation study was conducted. Two subjects were enrolled into this imaging study after obtaining informed consent. $T_{1\rho}$ imaging was performed under three conditions: 1) pre-hypercapnia (breathing room air), 2) hypercapnia (breathing 7.5% CO_2), and 3) post-hypercapnia (breathing room air). $T_{1\rho}$ weighted images were acquired using a turbo spin-echo (TSE) sequence with a spin-locking preparation pulse which created a B_1 field of 500Hz. Imaging parameters were TE=12ms, TR=2s, field of view=240x240mm, imaging matrix size=128x64, bandwidth = 130Hz/pixel and slice thickness=3cm, TSL= 20, 40, 60 and 80ms. In addition, we performed another $T_{1\rho}$ study with hyperventilation (40 breaths / minute). $T_{1\rho}$ images were acquired using the same parameters used in the 7.5% CO_2 study.

3.4.2. Results

To ensure that similar manipulations could be performed in humans and the sensitivity of the $T_{1\rho}$ was similar between the human and animal scanners, a single subject was imaged while manipulating the end-tidal CO_2. Figure 3.5A shows $T_{1\rho}$ maps of the human brain varied with end-tidal CO_2 concentration ($EtCO_2$) during the 5% CO_2, room air, and hyperventilation conditions. During CO_2 inhalation a widespread increase in $T_{1\rho}$ times consistent with the expected acidosis was evident as compared to the baseline room air condition (Student's t-test; $p<0.01$). Similarly, the reduced $T_{1\rho}$ times during hyperventilation are consistent with the expected alkalosis (Student's t-test; $p<0.01$). The pH dependence of $T_{1\rho}$ in brain tissue is clearly seen in the Figure 3.5C. $T_{1\rho}$ times were measured as the mean of ROI with 5x5mm square as shown in a white square in the Figure 3.5A. Figure 3.5B shows the subtracted $T_{1\rho}$ maps between hyperventilation and room air, and between 5% CO_2 and room air. In the subtraction images, voxels that were acidic relative to the baseline condition are shown in red and voxels that were more alkaline are shown in blue.

Figure 3.6A shows the subtracted $T_{1\rho}$ maps between hypercapnia (7.5% CO_2) and pre-hypercapnia (Air1), and between hypercapnia (7.5% CO_2) and post-hypercapnia (Air2). The red color represents higher acidity while the blue color represents increased alkalinity. During CO_2 inhalation the widespread increases in $T_{1\rho}$ times are consistent with the expected acidosis as compared to the baseline room air condition. During post-hypercapnia $T_{1\rho}$ time returns to a level similar to the pre-hypercapnic phase as shown in Figure 3.6B.

To examine the use of $T_{1\rho}$ to detect changes in human brain pH, we performed another $T_{1\rho}$ study with hyperventilation. Figure 3.7 shows the subtracted $T_{1\rho}$ maps between the room air (pre-hyperventilation, air1) and the hyperventilation, and between the room air (post-hyperventilation, air2) and hyperventilation. The red color represents higher acidity however the blue color represents increased alkalinity. During the hyperventilation, the widespread reduced $T_{1\rho}$ times are consistent with the expected alkalosis as compared to the baseline room air condition. However, $T_{1\rho}$ time returns to a level similar to the pre-hyperventilation (air1) phase as shown in Figure 3.7B. There are some red color regions in the edge of the brain because of motion artifacts during the hyperventilation.

3.5. Discussion and Conclusion

In the sheep blood study, we found a double disassociation between the $T_{1\rho}$ and BOLD signal sensitivity. $T_{1\rho}$ is not sensitive to blood oxygenation but to pH changes, while BOLD is sensitive to pH changes, but not to blood oxygenation. Thus these two MR contrast mechanisms arise from different biologic phenomena and do not directly influence each other. Two prior studies have also investigated the influence of blood oxygenation on $T_{1\rho}$ measurements [106,111]. Zipp et al. showed that $T_{1\rho}$ is insensitive to oxygen saturation level in packed erythrocytes for red blood cells from normal controls while subjects with sickle cell disease showed a stronger relationship between the estimated $T_{1\rho}$ times and blood oxygenation level [117]. Another study by Kettunen et al. found a linear positive relationship between $T_{1\rho}$ relaxation time for the similar oxygen saturation level as used in this study and same field strength scanner [112]. However, we

used a slightly lower $T_{1\rho}$ frequency as compared to the lowest $T_{1\rho}$ frequency reported by Kettunen et al. In addition, they used a $T_{1\rho}$-weighted sequence based on a gradient-echo sequence, while the present study employed a $T_{1\rho}$-weighted sequence based on a turbo spin-echo sequence. The use of a 180° inversion RF pulse in turbo spin-echo sequences could minimize T_2^* effects. Moreover, they used bovine blood for their experiment while the present study used sheep blood. Previous studies have investigated the difference between sheep and bovine red blood cells and found no difference in the membrane permeability of water but did find a species-specific variation in the membrane proteins among species.

$T_{1\rho}$ times were collected in an anesthetized awake mouse using our 4.7T Varian scanner under three conditions: 1) normal breathing, 2) 20% CO_2 inhalation, and 3) post-HCO_3^- injection (5 mmol/kg, ip). $T_{1\rho}$ maps were estimated on a voxel by voxel basis and $T_{1\rho}$ times were calculated for when the mouse was breathing CO_2, or air, and following HCO_3^- injection. Consistent with our phantom studies and earlier fiber-optic pH measurements, we found that 20% CO_2 altered mean $T_{1\rho}$ times by amounts consistent with an average pH reduction. In contrast, HCO_3^-injection (5 mmol/kg, ip) altered $T_{1\rho}$ times by values consistent with a pH increase. Consequently, we found that $T_{1\rho}$ is sufficiently sensitive to detect pH changes on the order of 0.1 pH units or less measured simultaneously with a fiber optic pH sensor surgically implanted into the amygdala. In another mouse study, it is observed that the $T_{1\rho}$ times did not change when the mouse was under the hyperoxia (100% O_2) and hypoxia (10% O_2). It suggests that the $T_{1\rho}$ relaxation is sensitive to the change of the brain pH, but not sensitive to the brain oxygenation level.

Additionally, in the human brain we found that $T_{1\rho}$ is sensitive to pH changes induced by hyperventilation and by CO_2 inhalation.

Therefore these advances increase our enthusiasm for developing $T_{1\rho}$ as a pH-sensitive measure for a variety of applications. One application that is a primary goal of this proposal is to more precisely measure endogenous pH changes that occur with brain activity.

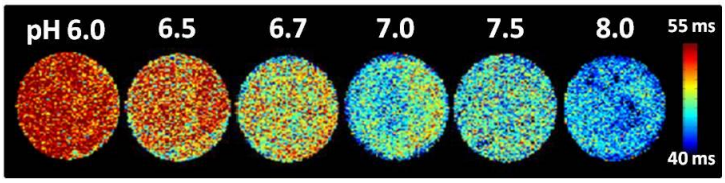

(A)

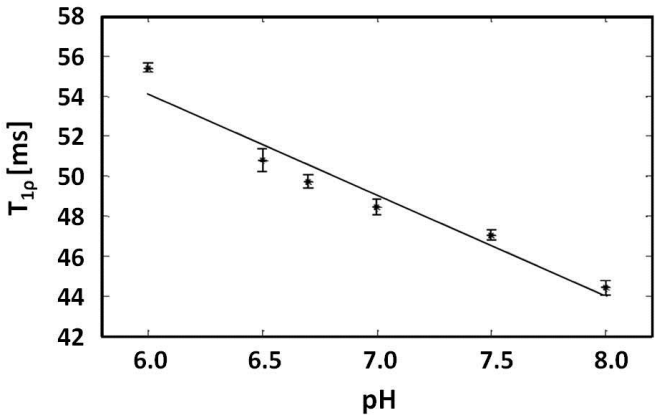

(B)

Figure 3.1. $T_{1\rho}$ measurements of agar phantoms across a pH spectrum. (A) $T_{1\rho}$ maps for agar phantoms of different pH values. $T_{1\rho}$ is inversely proportional to the pH value as shown in Figure 3.1B. (B) The result presented in Figure 3.1B were calculated in a 5X5mm square ROI placed manually near the center of the phantom.

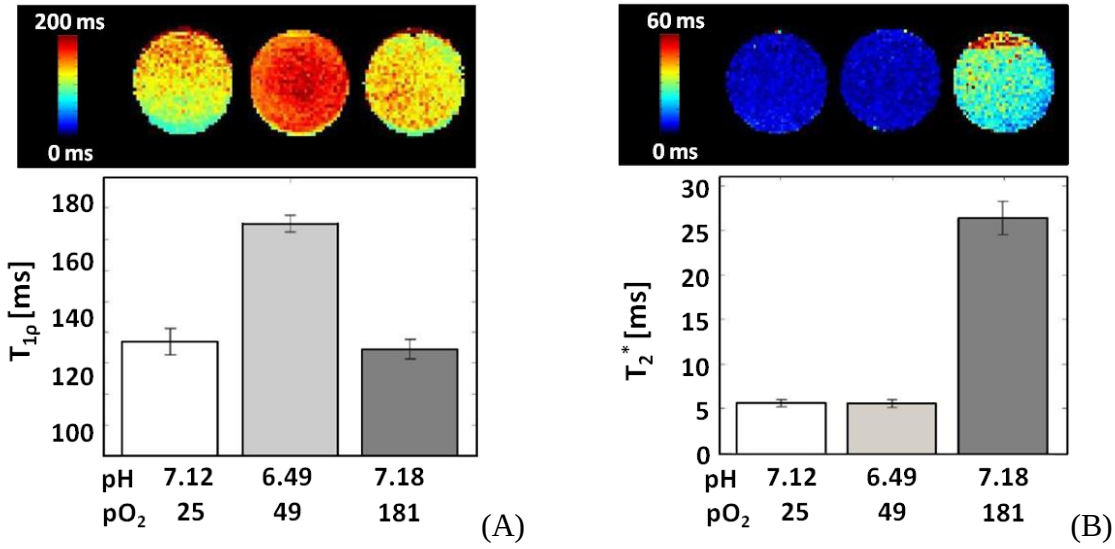

Figure 3.2. $T_{1\rho}$ measurements of sheep blood phantoms across a pH and oxygenated spectrum. (A) $T_{1\rho}$ maps and measurements of sheep blood phantoms in control (left), acidified (center), and oxygenated (right) conditions demonstrating $T_{1\rho}$ increases with a decrease in blood pH and is independent of the oxygenated state of hemoglobin. (B) BOLD maps and measurements of sheep blood phantoms in control (left), and acidified (center), and oxygenated (right) conditions demonstrating BOLD is dependent of the oxygenated state of hemoglobin and independent of the pH of the blood.

	Control		Acidified blood		Oxygenated blood	
	Before	After 30min.	Before	After 30min.	Before	After 30min.
pH	7.12	7.10	6.49	6.49	7.18	7.17
pCO_2	71	73	187	182	52	52
pO_2	25	35	49	50	181	680
$T_1\rho$ [ms]	136.8 ± 4.3		173.2 ± 2.7		134.3 ± 3.2	
T_2^* [ms]	5.6 ± 0.38		5.5 ± 0.4		26.2 ± 2.9	

Table 3.1. Physiological variables, $T_1\rho$, and T_2^* measurements of blood phantoms across a pH and oxygenated spectrum.

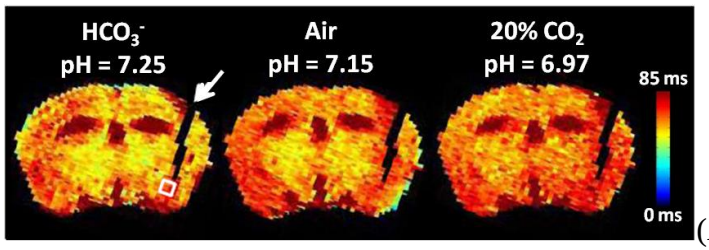

(A)

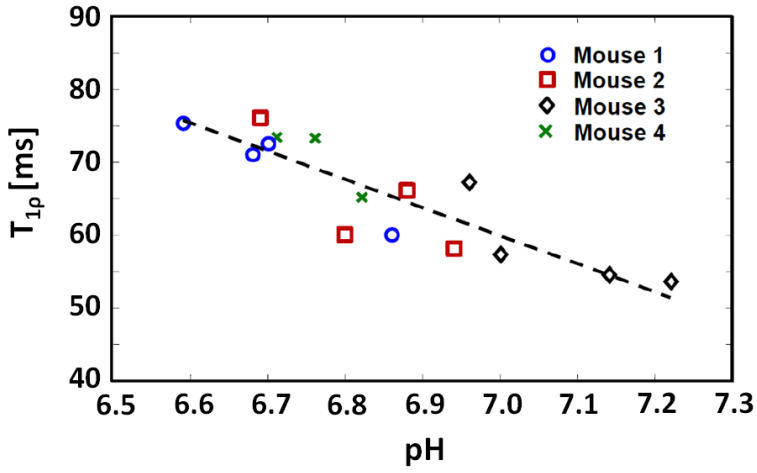

(B)

Figure 3.3. Detecting pH changes with $T_{1\rho}$ in the brain of an anesthetized mouse. (A) Optic pH measurements of the rodent amygdala and $T_{1\rho}$ maps of the rodent brain after given HCO_3^- (left), exposed to room air (center) and exposed to 20% CO_2 (right) demonstrates an increase in $T_{1\rho}$ with a decrease in brain pH. In the mouse model, widespread increases in $T_{1\rho}$ times during CO_2 inhalation were found consistent with the expected acidosis as compared to the baseline room air condition. (B) Figure 3.3B show the relationship between $T_{1\rho}$ and pH measured across all four of the mice. A fiber optic sensor, which was previously implanted into the amygdala, was used to continuously measure brain pH during the entire experiment.

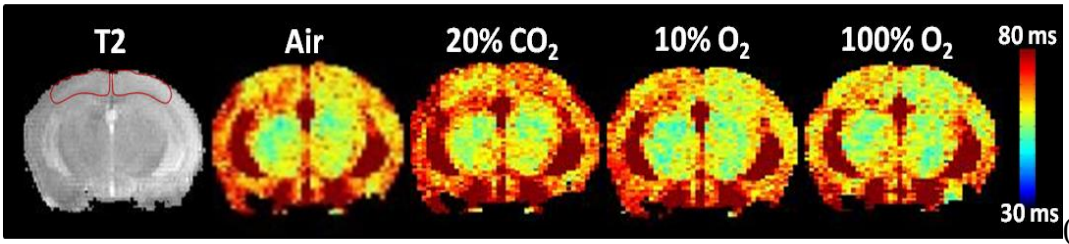

(A)

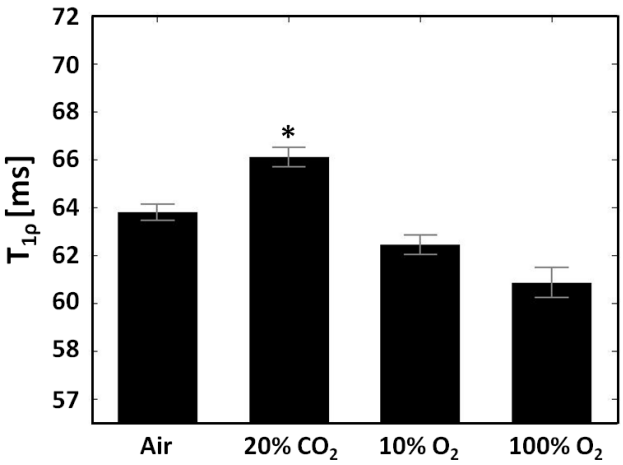

(B)

Figure 3.4. Detecting pH changes with $T_{1\rho}$ in the brain of an awake mouse. (A) A T_2-weighted image (left). $T_{1\rho}$ maps of the rodent brain after exposed to room air, 20% CO_2, 10% O_2, and 100% O_2 demonstrating $T_{1\rho}$ increase with a decrease brain pH resulting from CO_2 inhalation and independent of the oxygenated state of hemoglobin by exposing different concentrations of the oxygen. During 20% CO_2 inhalation, the increases in $T_{1\rho}$ times are consistent with the expected acidosis as compared to the baseline room air condition. However, the change of the oxygen level does not significantly affect $T_{1\rho}$ times as shown Figure 3.4B. (B) Figure 3.4B shows the change of $T_{1\rho}$ times in the rodent brain during room air, 20% CO_2, 10% O_2, and 100% O_2. $T_{1\rho}$ times were calculated in the ROI having 174 pixels as shown in red color in T_2-weighted image in the Figure 3.4A.

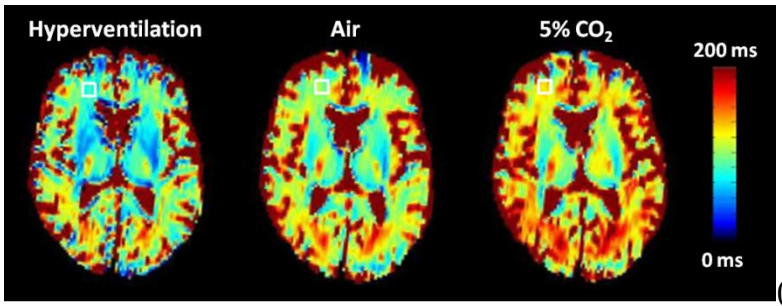

(A)

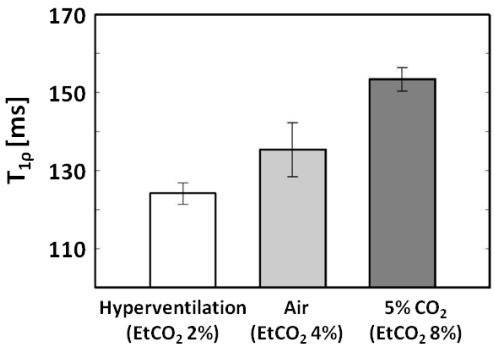

(B)

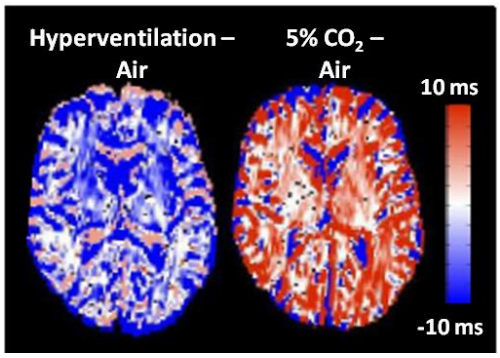

(C)

Figure 3.5. Human brain $T_{1\rho}$ measurements across a pH spectrum. (A) $T_{1\rho}$ maps of the human brain varied with end-tidal CO_2 concentration ($EtCO_2$) during the 5% CO_2, room air, and hyperventilation conditions. The intensity maps represent $T_{1\rho}$ times ranging between 0ms (basic) to 200ms (acidic). During CO_2 inhalation, the widespread increases in $T_{1\rho}$ times are consistent with the expected acidosis as compared to the baseline room air condition. Whereas the reduced $T_{1\rho}$ times during hyperventilation are consistent with the expected alkalosis. (B) The change of $T_{1\rho}$ times in brain tissue is clearly seen in the Figure 3.5B. (C) Figure 3.5C shows the subtracted images between the $T_{1\rho}$ map with hyperventilation and the $T_{1\rho}$ map with room air and between the $T_{1\rho}$ map with 5% CO_2 and the $T_{1\rho}$ map with room air. $T_{1\rho}$ times change with respiratory challenges. $T_{1\rho}$ times were calculated in a 5x5 square ROI placed manually in the gray matter as shown in white color square in the Figure 3.5A.

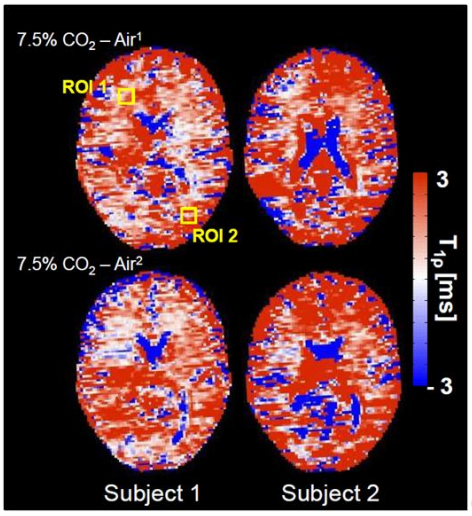

(A)

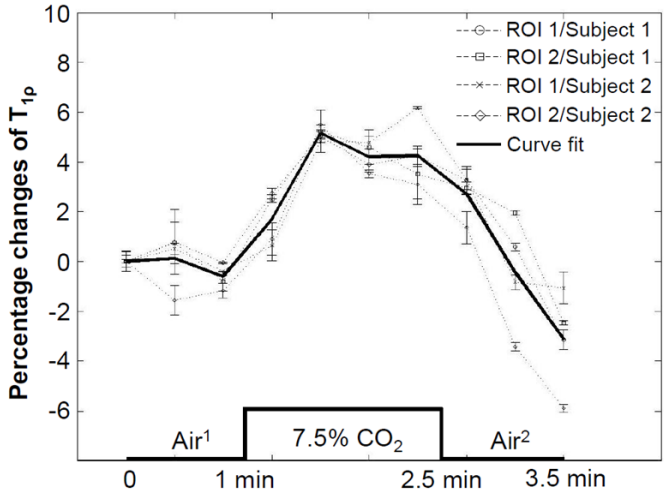

(B)

Figure 3.6. Changes in $T_{1\rho}$ in human brain during hypercapnic challenge. (A) Subtracted images between the $T_{1\rho}$ map with 7.5% CO_2 and the $T_{1\rho}$ map with room air for two subjects. (B) Percentages of $T_{1\rho}$ times with respiratory challenges. ROIs were defined in white matter as shown in yellow color square in Figure 3.6A.

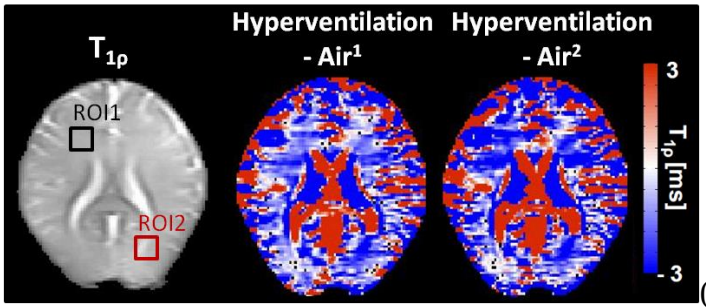

(A)

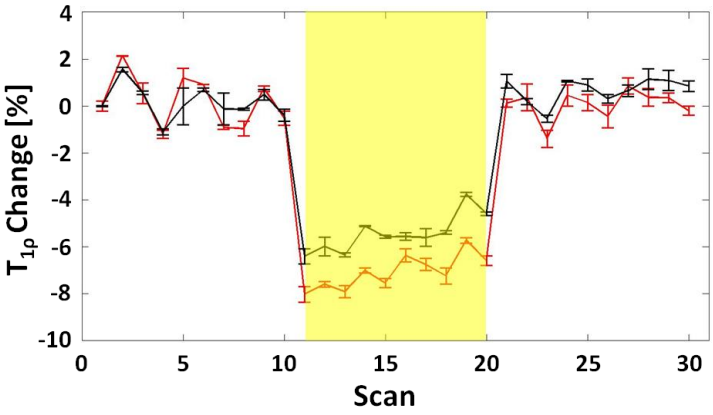

(B)

Figure 3.7. Changes in $T_{1\rho}$ in human brain during hyperventilation. (A) A $T_{1\rho}$-weighted image with spin-lock duration of 12ms (left). ROIs were defined in white matters as shown in black and red color squares. Subtracted images between the $T_{1\rho}$ map with room air and the $T_{1\rho}$ map with hyperventilation for single subject. (B) $T_{1\rho}$ changes during breathing room air, hyperventilating (40breaths/minute), and breathing room air. The yellow-shaded areas represent the hyperventilation phase.

CHAPTER 4

DETECTING ACTIVITY-EVOKED PH CHANGES IN HUMAN BRAIN

4.1. Background and Rationale

Brain pH is homeostatically regulated in large part through the CO_2/HCO_3^- buffering system. In a reversible reaction, CO_2 combines with water to form carbonic acid, which readily dissociates into HCO_3^- and H^+. Raising CO_2 shifts the equilibrium toward H^+, thereby lowering pH. Conversely, raising HCO_3^- shifts the equilibrium away from H^+ and increases pH. Because of the brain's powerful capacity to buffer pH, it has been questioned whether brain pH changes during brain function [14]. However, there are several potential sources of localized pH change. As carbohydrate metabolism increases so does production of pH-lowering by-products lactic acid and CO_2 [17]. Additionally, pH can be altered by activity-evoked HCO_3^- transport [112]. Local field potentials produced by ion flux might also change pH [113]. Finally, synaptic vesicles are acidic and release protons into the extracellular space during neurotransmission [114]. Such dynamic pH fluctuations have the potential to dramatically alter cognition and behavior through a number of pH-sensitive receptors and channels [115]. An example is the acid-sensing ion channels, which promote synaptic plasticity, learning, and memory [116,117]. Therefore, an ability to measure pH in the functioning brain could add new insight into a poorly understood dimension of brain function and dysfunction.

This study aims to evaluate the utility of $T_{1\rho}$ MR imaging as a method to measure pH dynamics. The sensitivity of $T_{1\rho}$ to pH changes was evaluated in visual cortex during

functional activation. We measured the change in lactate concentration resulting from neural activity in the visual cortex, which may contribute to local acidosis since lactate is one of the primary determinants of extracellular pH. Furthermore, ^{31}P spectroscopy, a widely accepted measure of pH, was used to validate pH changes in visual cortex during neural activity. In addition, we showed that $T_{1\rho}$ has higher spatial specificity than BOLD contrast.

4.2. Methods

Six subjects (four males and two females, 28-35 years of age) underwent MR, fMRI and ^{1}H MRS study. The study was performed twice on each of six subjects. A visual flashing checkerboard (22x22 squares) alternating at 4Hz was presented for all of the functional imaging studies using a block design. The baseline condition was a fixation cross. Every four seconds during the flashing checkerboard condition, a red square was shown in the center of the checkerboard. Subjects were asked to press a button on a fiber optic response system (Lumina LP-400, Cedrus Corporation, San Pedro, USA) when the square appeared. This was done to ensure that the subjects were on task during the entire study. This was especially important during the spectroscopic portion of the study where the activation period was lengthy. The stimulation timing sequence delivery and response registration was controlled by Presentation 13.1 software (Neurobehavioral System Inc., Albany, CA, USA). For BOLD imaging, 7 cycles of activation and visual fixation were presented with an 80 second period. The task began and ended in the baseline condition. The BOLD imaging portion of the study was repeated twice. For functional $T_{1\rho}$, 5 cycles were collected with a 72 second period. This portion also began and ended with the

baseline condition. The functional $T_{1\rho}$ was acquired three times. For functional spectroscopic imaging, the task began in the baseline task (7 minutes 20 seconds) followed by the visual activation condition (7 minutes 20 seconds) and returning to the baseline condition for 7 minutes 20 seconds. Anatomical 3D T_1-weighted scans were collected using an MP-RAGE sequence using the following parameters: TE=2.8ms, TR=2530ms, TI=909ms, FA=10°, field of view = 256x256x256mm, matrix size=256x256x256, bandwidth=180Hz/pixel. BOLD imaging was performed using a T_2^* weighted gradient-echo sequence with the following acquisition parameters: TE=30ms, TR=2000ms, flip angle=90°, field of view=220x220mm, matrix size=64x64, bandwidth=2004Hz/pixel, and slice thickness/gap=4.0/1.0mm. Functional $T_{1\rho}$ imaging was performed using an echo-planar spin-echo sequence with an additional $T_{1\rho}$ spin-lock encoding pulse. The sequence parameters were TE=12ms, TR=2200ms, field of view=220x220mm, matrix size =64x64, bandwidth=1954Hz/pixel and slice thickness =4mm. Three spin-lock pulses were used (10, 30 and 50ms) with a spin-lock frequency of 400Hz. The spin-lock pulse duration was for each repetition was selected based on the repetition number modulo three. A ^{1}H MRS scan was acquired using a single voxel point-resolved spin-echo sequence (PRESS) with water suppression using the following parameters: TE=288ms, TR=1680ms, bandwidth=1000Hz. A TE of 288ms was used to minimize lipid and macromolecule signal overlapping lactate at 1.3ppm. The MRS voxel (20x20x20mm3) was positioned on a localizing image at the site of activation observed in the BOLD study. Each spectroscopic acquisition lasted 3 minutes 40 seconds allowing two measurements to be obtained during each condition.

A second experiment was conducted using ^{31}P spectroscopic imaging after acquiring a dual tune head coil ($^{31}P/^{1}H$). This portion of the study provided an external validation of the pH changes while viewing a flashing checkerboard. Six subjects were recruited into this functional imaging study to assess functional brain metabolite changes associated with the flashing checkerboard after informed written consent was obtained. The imaging consisted of a localizer followed by a 2D ^{31}P spectroscopic acquisition using a free induction decay acquisition. The ^{31}P CSI study was collected using the following parameters: TE=2.3ms, TR=4000ms, FOV=240x240mm, Matrix=8x8, thickness=30mm, Averages=16, Vector Size=1024, and Bandwidth =2500ms. A volume of 40 mm isotropic centered on the occipital cortex was selected as the shim volume and encompassed the CSI voxel of interest. This acquisition is repeated three times. During the first and third acquisition the subject is gazing at a fixing cross while during the second acquisition a 8Hz flashing checkerboard is presented. The subjects are instructed to respond as in the previous studies to the red square that appears to ensure that the subject is engaged in the task.

The anatomical T_1-weighted images for each subject were placed into the Montreal Neurological Institute (MNI) coordinate system using AFNI. The mean time series image was estimated and co-registered with the MNI aligned T_1-weighted scan using an affine transformation. All BOLD functional MRI data were analyzed using AFNI software. Pre-processing of T_2^* weighted time series data included three dimensional motion correction, slice timing correction, linear trend removal, motion correction, and spatial smoothing with a Gaussian filter (6mm Full width half maximum (FWHM)). The data from each run was concatenated before statistical analysis. The

analysis was performed for all voxels within the brain for each subject using a generalized linear model (GLM). A linear regression was performed to estimate the signal contributed by the blood oxygenation signal corresponding to the experimental design. An estimate of the hemodynamic response was estimated by convolving the experimental design with a gamma-variate function. The resulting t statistic for the hemodynamic response function was converted to a z-score. The mean T_2^* weighted image was estimated and used to co-register the images with the MNI aligned T_1-weighted anatomical image. The resulting transform was used to place the z-image into MNI space. A t-test was performed across the subjects and corrected for multiple comparisons using a FDR analysis.

The $T_{1\rho}$ data was preprocessed using a combination of AFNI and MATLAB. Motion correction was performed using AFNI. Each set of spin-lock times were then analyzed using MATLAB to generate a $T_{1\rho}$ map using a log-linear regression of the voxel signal intensity with the spin-lock time. The $T_{1\rho}$ data were concatenated and spatially smoothed using Gaussian filter (FWHM=6mm). The resulting $T_{1\rho}$ maps were analyzed using a linear regression where the relationship between the $T_{1\rho}$ map and the experimental design was estimated. The resulting statistical t-statistics were converted to z-scores. The mean spin-lock image was estimated and used to co-register the $T_{1\rho}$ images with the MNI aligned T_1-weighted anatomical image. The resulting transform was used to place the z-image into MNI space. A t-test was performed across the subjects and corrected for multiple comparisons using a FDR analysis.

The two ^1H spectroscopic measurements obtained for each condition were frequency and phase corrected and then averaged in Matlab, and the resulting spectral

data was analyzed using LCMODEL (Stephen Provencher Inc., Oakville, Ontario, Canada). Ratios of Lactate/Cr and Lac/NAA were obtained and compared between the 1) baseline, 2) activation, and 3) recovery periods using an ANOVA.

The ^{31}P data was analyzed using the Siemens Syngo software to determine the chemical shift of the inorganic phosphate (Pi) and phosphocreatine (PCr) peaks in the ^{31}P spectra. The analysis included frequency filtering, frequency and phase correction, baseline correction, and curve fitting with prior knowledge. The pH within the brain was estimated using the following formula as proposed by Petroff et al [118].

$$pH = 6.77 + \log \{(\delta-3.29)/(5.68-\delta)\}$$

where δ is the chemical shift between in ppm between Pi and PCr. The pH estimates for the baseline, activated, and recovery phases where compared using an ANOVA model in SPSS.

4.3. Results

Figure 4.1 shows the ^{1}H MR spectra for baseline, visual stimulation, and post-stimulation from one subject. The lactate doublet centered at 1.33ppm was visible in the subject. Paired t-test showed that the main effect for time was due to significant increase in lactate from BS1 to VS1 and VS2 and from BS2 to VS1 and VS2 ($p<0.01$), and significant decrease in lactate from VS1 to PS1 and PS2 and from VS2 to PS1 and PS2 ($p<0.01$). The overall increase in lactate, quantified as the difference between the weighted average of VS1 and VS2 compared with the average of BS1 and BS2 was

highly significant ($p<0.005$). Moreover the overall decrease in lactate quantified as the difference between the weighted average of VS1 and VS2 compared with the average of PS1 and PS2 was highly significant ($p<0.005$).

During the visual activation study, statistically significant activation was observed in the primary visual cortex for both the BOLD and $T_{1\rho}$ techniques. Figure 4.2 shows the group activation maps of the $T_{1\rho}$ and BOLD imaging in MNI space overlaid on the T_1-weighted anatomical image. The activated voxels with a significant activation ($z>2.9$, $p<0.002$ corrected) are shown. Areas of the $T_{1\rho}$ activation related to pH changes are smaller than those of the BOLD changes reflecting sensitivity to the blood oxygenation level. Statistically significant elevation in the lactate to Cr ratio measurements was also found during visual activation as compared to both the baseline and recovery periods. This also held true for the lactate to NAA ratios as well.

The ^{31}P data showed a reduction in the estimated pH value in all subjects during the activated state within the voxel encompassing the visual cortex. The estimated values returned towards the baseline level during the recovery period. Statistical analysis of the pH values were shown to be significantly lower (7.313/0.985) during the activated state ($p<0.05$) as compared to the baseline (7.419/1.0) and recovery (7.382/0.995) states.

4.4. Discussion and Conclusions

$T_{1\rho}$ imaging can be used to measure brain pH changes associated with brain function. The findings in the preliminary study suggest that local acidosis occurs with brain function that can be detected using MR imaging. This acidosis was measured using both $T_{1\rho}$ imaging, as well as ^{31}P spectroscopy. We found that a decrease in brain pH was

shown in all subjects during visual stimulation in the visual cortex, as compared to the baseline and post-stimulus period. The voxel in which the spectroscopy measurements were obtained were large (volume=27cm^3) and were acquired over a 7 minute period limiting the ability to study more rapid pH dynamics that may occur on the order of seconds. However, the $T_{1\rho}$ imaging technique had a temporal resolution of 6-9s per measurement with a 4mm isotropic resolution. This technique holds the possibility to study pH dynamics with much higher temporal resolution than ^{31}P spectroscopic techniques. Furthermore, it may also be possible to further improve the temporal resolution of this technique using parallel imaging or compressed sensing reconstruction techniques.

Together these data suggest that brain pH can change during normal activity and not just during pathological states such as a seizure or stroke [14,119]. Although activity-evoked pH changes have been suggested [14,17,114], the data presented here provide the most direct supportive evidence thus far in the human brain. There a number of potential sources of pH change and several of these might summate to produce the localized acidosis detected here. Further study will be required to identify the relevant sources of acid and to determine whether they might have functional consequences. A growing list of pH sensitive receptors and channels suggests that the pH changes observed here might have a prominent role in brain function and dysfunction [115,116]. Interestingly, panic disorder patients exhibited abnormally high lactate levels in the visual cortex in response an equivalent visual checkerboard task [120]. Coupled with that observation, the data presented here raise the possibility that pH abnormalities might occur in panic disorder and may contribute to the pathophysiology of panic [17]. Regardless of the implications

for brain function, this study suggests a novel approach for mapping brain activity. The currently employed mapping measures, including fMRI and PET, rely on the hemodynamic response. The data herein suggest that although $T_{1\rho}$ correlates with the hemodynamic response, it does not depend on it directly, and thus might provide a tractable independent measure of neural activity.

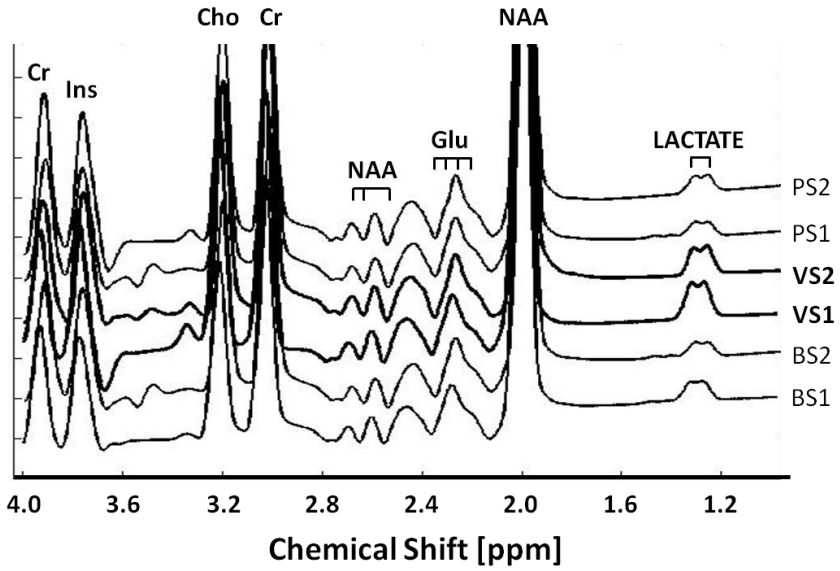

Figure 4.1. Localized ^{1}H MR spectra for baseline, visual stimulation, and post-stimulus. The six spectra shown were obtained consecutively from the same voxel in the same subject. Stack plot of spectra obtained before (baseline 1, BS1 and baseline 2, BS2), during (visual stimulation 1, VS1 and visual stimulation 2, VS2), and following visual stimulation (post-stimulus 1, PS1 and post-stimulus 2, PS2). In vivo metabolites include N-acetylaspartate (NAA), creatine (Cr+PCr), choline (Cho), myo-inositol(Ins), and glutamate (Glu).

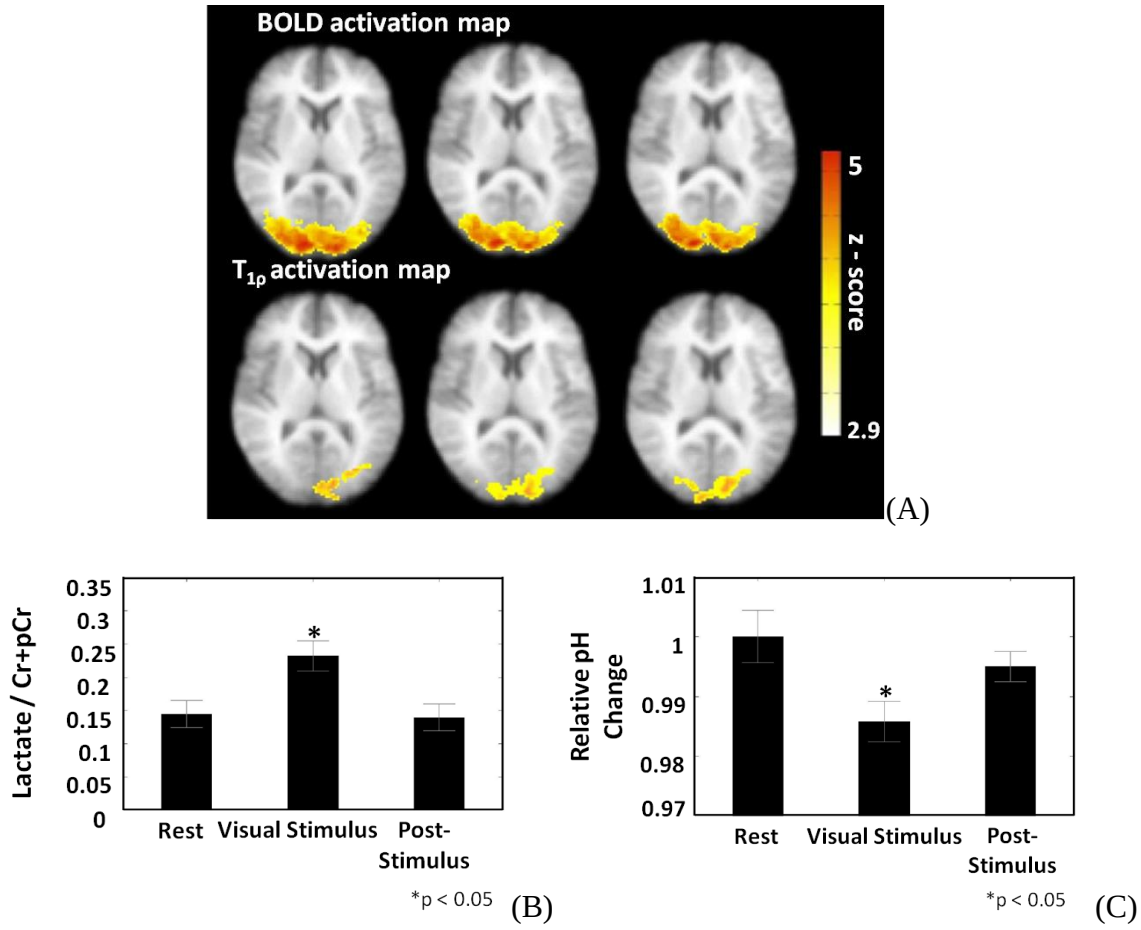

Figure 4.2. Brain function resulting from visual flashing checkerboard stimulation. (A) BOLD and $T_{1\rho}$ functional activation maps (P<0.002 corrected) resulting from the visual flashing checkerboard stimulus. Three contiguous slices are shown. (B) The lactate to total creatine ratio increased during visual stimulation and returned to its baseline state during the post-stimulus recovery phase. The increase was statistically significant (p<0.05). (C) pH measured via ^{31}P spectroscopy in the visual cortex was found to decrease during visual stimulation. This acidosis (0.1 pH units) was statistically significant (p<0.05).

CHAPTER 5

$T_{1\rho}$ RESPONSE TO THE ACTIVITY-DEPENDENT LOCALIZED ACIDOSIS

5.1. Background and Rationale

While pH regulation is often assumed to be homeostatic, local dynamic pH fluctuations occur in the brain with neural activity. There are a number of potential source of acid in the brain. Carbohydrate metabolism induced by increased neural activity produces lactic acid, CO_2, and H^+ as end-products. In addition, the synaptic release of protons from neurotransmitter vesicles generates a localized acidosis to modulate pH-sensitive channels and other receptors in the pre and post-synaptic membrane. Such transient local pH changes have the potential to dramatically alter pathophysiology and behavior through a number of pH-sensitive receptors in the brain. For example, acid-sensing ion channels-1a (ASIC1a) plays a critical roles in fear, anxiety-related behaviors [19,20,121-123], and CNS diseases [19,116]. In addition, significantly elevated baseline lactate concentrations have been found in bipolar [124] as well as functionally elevated lactate responses in panic disorder [120]. These findings suggest that local or more global acidosis exists within these disorders possibly resulting from altered metabolic regulation.

The ability to non-invasively measure pH dynamics in vivo provides unique insight into better understanding brain function as well as neurological and psychiatric disorders. Various magnetic resonance (MR) approaches have been developed to measure brain pH with pH-dependent chemical shift changes using MR spectroscopy [70,81-84,125,126], pH-sensitive contrast agents [127,128], proton exchange properties [94,129-

131], and by combining paramagnetic contrast agents with proton exchange [132-134]. ^{31}P MR spectroscopy methods have been widely used to measure intracellular pH using the pH-dependent chemical shift between inorganic phosphate (Pi) and phosphocreatine (PCr) [135,136]. The disadvantage of the ^{31}P spectroscopic techniques is their limited spatial resolution (on the order of 10-30cm^3 volume), long acquisition times (on the order of 5-10 minutes) for a single measurement, and the requirement of special hardware that is typically not available on clinical scanners. Molecules with pH-sensitive ^{1}H resonance have also been reported [71,72,137,138]. 2-imidazole-1-yl-3-ethoxycarbonylpropionic acid (IEPA) has been used to estimate pH, which is pH-dependent chemical shift due to the protonation and deprotonation of the amine group. pH-dependent relaxation properties have also been shown using an injection of exogenous contrast agents [70,81]. pH-sensitive gadolinium complexes has been shown the possibility of measuring pH with a spatial resolution comparable to standard MRI [127,128]. However, the enhancement observed in an image depends on the local concentration of agent as well as pH, leading to the difficulty of quantification of the environmental parameter of interest. Recently, ^{1}H based MR pulse sequences using proton exchange properties have been used to probe pH changes in vivo [93,99,130, 139]. These techniques include amid proton transfer (APT), a specific variant of chemical exchange saturation transfer (CEST), and $T_{1\rho}$. APT can probe the interaction between bulk water and amide protons in the peptide bonds to enable assessment of microenvironment properties such as pH and temperature. It has been shown that the amide proton exchange rate is base-catalyzed for pH within the physiological range [140]. This approach has been used to image pH changes in the ischemic rat brain [99] and brain tumors in human [87,99]. The $T_{1\rho}$ signal reflects water-

protein interactions in tissue, which has been shown to be pH sensitive. The sensitivity of $T_{1\rho}$ to the surrounding pH has been well documented. Several studies have shown pH-dependency of $T_{1\rho}$ in phantoms and animal models [105,106,139,141]. The extent of $T_{1\rho}$ positively correlates with lactate concentration, suggesting that pH modulates $T_{1\rho}$ in ischemic tissue [105]. Recently, we found that $T_{1\rho}$ contrast can detect dynamic fluctuations in pH associated with brain activity resulting from a visual flashing checkerboard [139]. Both the $T_{1\rho}$ and ^{31}P measurements revealed a local acidosis in the visual cortex associated with brain activity. In addition, a significant increase in the lactate signal using ^{1}H spectroscopy within the visual cortex was observed. The BOLD signal originates in the venous system, which results in spatial displacement of the signal from the actual site of brain activity. Therefore functional $T_{1\rho}$ imaging may provide improved localization of brain activity since acidic end products of metabolism, lactic acid, are likely more localized to the brain activity as compared to blood oxygenation.

A number of previous positron emission tomography (PET) and functional MRI (fMRI) BOLD studies have shown frequency dependence of the blood flow response within the visual cortex response to a flashing checkerboard. Previous studies have found the maximum blood flow response to occur with stimulation frequencies in the range of 6-8Hz [142,143,144,145]. In addition, a previous study using ^{1}H spectroscopy has also shown frequency dependence in lactate signal [146]. In this study, we hypothesized that the measurements of pH assessed using ^{31}P spectroscopy and $T_{1\rho}$ will exhibit similar frequency dependence with the greatest acidosis occurring near 8Hz. To test this hypothesis, dynamic imaging was performed using $T_{1\rho}$, BOLD, and ^{31}P spectroscopy

while viewing a full field flashing checkerboard with different temporal frequencies (1, 4, and 7Hz).

5.2. Methods

Ten subjects (Seven men and three women, 25-35 years of age) underwent MRI, fMRI, and ^{31}P MRS study. Signed informed consent was obtained prior to beginning the study in accordance with the University of Iowa Institutional Review Board.

MR images of the brain were obtained on a 3.0T Siemens TIM Trio scanner (Siemens Medical Solutions, Erlangen, Germany) using a 12 channel head-coil. High-resolution anatomical T_1-weighted images were acquired using a 3D MP-RAGE sequence using the following parameters: TR=2530ms, TE=2.8ms, TI=909ms, flip angle=10°, FOV= 256x256x256mm, matrix size=256x256x256, bandwidth=180Hz/pixel. BOLD imaging was performed using a T_2^*-weighted gradient-echo sequence with the following acquisition parameters: TR=2000ms, TE=30ms, flip angle=90°, FOV=220x220mm, matrix size=64x64, bandwidth=2004Hz/pixel, 25 slices and slice thickness/gap =5.0/1.0mm. $T_{1\rho}$ imaging was performed using an echo-planar spin-echo sequence with an additional $T_{1\rho}$ spin-lock encoding pulse. The sequence parameters were TR=2500ms, TE=12ms, FOV=220x220mm, matrix size=64x64, bandwidth= 1954Hz/pixel, 15 slices and slice thickness/gap=5.0/1.0mm. Two spin-lock pulses were used (10 and 40ms) with a spin-lock frequency of 350Hz. A final experiment was run using ^{31}P spectroscopic imaging. The subjects were briefly removed from the scanner and the 12 channel head-coil has replaced with a quadrature transmit receive dual tune $^{31}P/^{1}H$ coil (RapidMRI, Columbus, Ohio). Imaging for the spectroscopic portion of the study

consisted of a localizer followed by a 2D ^{31}P spectroscopic acquisition. ^{31}P CSI spectroscopy was collected using a free induction decay acquisition with the following parameters: TR=4000ms, TE=2.3ms, FOV=240x240mm, matrix size=8x8, thickness=30mm, bandwidth=1000Hz, vector size=1024. A volume of 40 mm isotropic centered on the occipital cortex was selected as the shim volume and was utilized as the CSI voxel of interest for metabolic measurements.

A visual flashing checkerboard was presented for the functional imaging using a block design as shown in Figure 5.1. Each block of visual stimulation used one of three frequencies (1, 4, or 7Hz) of the flashing checkerboard, which were presented in random order. The baseline condition was a fixation cross. Every four seconds during the flashing checkerboard condition, a red square was shown in the center of the checkerboard. Subjects were asked to press a button on the fiber optic response system (Lumina LP-400, Cedrus Corporation, San Pedro, USA) when the square appeared. This was done to ensure that the subjects were on task during the entire study. This was especially important during the spectroscopic portion of the study where the activation period was lengthy. For BOLD and $T_{1\rho}$ imaging, 7 cycles of activation and visual fixation were presented with a 72 second period. The task began and ended in the baseline condition. Two runs of the BOLD and $T_{1\rho}$ measurements were obtained. For ^{31}P spectroscopy, the session consisted of four blocks each lasting 5min 20sec. The visual stimulation was presented to the subjects using MATLAB (The MathWorks, Inc., Natick, MA, USA) and the Psychophysics Toolbox (Brainard, 1997 and Pelli, 1997).

The anatomical T_1-weighted images for each subject were placed into the Montreal Neurological Institute (MNI) coordinate system using AFNI. The mean time

series image was estimated and co-registered with the MNI aligned T_1-weighted scan using an affine transformation. All functional imaging data were analyzed using a combination of AFNI (Cox, 1996) and MATLAB.

For BOLD data, pre-processing of T_2^*-weighted time series data included three dimensional motion correction, slice timing correction, linear trend removal, and spatial smoothing with a Gaussian filter (6mm FWHM). The data from each run was concatenated before statistical analysis. The analysis was performed for all voxels within the brain for each subject using a general linear model (GLM). A linear regression was performed to estimate the signal contributed by the blood oxygenation signal corresponding to the experimental design. An estimate of the hemodynamic response was estimated by convolving the experimental design with a gamma-variate function (Cox, 1996). Nuisance regressors were included for the subject motion parameters and baseline fluctuations using a third order polynomial. The resulting t-statistic for the hemodynamic response function was converted to a z-score. The mean T_2^*-weighted image was estimated and used to co-register the images with the MNI aligned T_1-weighted anatomical image. The resulting transform was used to place the z-image into MNI space.

For $T_{1\rho}$ data, motion correction was performed using AFNI. Each set of spin-lock times were then analyzed using MATLAB to generate a $T_{1\rho}$ map using a log-linear regression of the voxel signal intensity with the spin-lock time. The $T_{1\rho}$ data were concatenated and spatially smoothed using Gaussian filter (6mm FWHM). The resulting $T_{1\rho}$ maps were analyzed using a linear regression where the relationship between the $T_{1\rho}$ map and the experimental design was estimated. The resulting statistical t-statistics were converted to z-scores. The mean spin-lock image was estimated and used to co-register

the $T_{1\rho}$ images with the MNI aligned T_1-weighted anatomical image. The resulting transform was used to place the z-image into MNI space.

The BOLD and $T_{1\rho}$ responses were analyzed using an ANOVA with the visual stimulation frequencies as a factor to identify voxels that whose response exhibited significant frequency relationship. A contrast between stimulation frequencies (7Hz vs. 1Hz, 7Hz vs. 4Hz, and 4Hz vs. 1Hz) was performed. The threshold for significance in the contrast map was set at $p<0.05$ (corrected using false discovery rate).

The ^{31}P data was analyzed using the same method as shown in Chapter 4.2. The brain pH in the visual cortex estimates according to the corresponding condition where compared using an ANOVA model in SPSS.

5.3. Results

Statistically significant activation maps corresponding to the flashing checkerboard were generated for each frequency (1, 4, and 7Hz) using both $T_{1\rho}$ and BOLD functional imaging. Figure 5.2 shows the group activation maps of the $T_{1\rho}$ and BOLD imaging in MNI space overlaid on the average T_1-weighted anatomical image. The activated voxels with a significant activation ($t>2.306$, $p<0.05$ corrected) are shown. The positive $T_{1\rho}$ activation is shown in red, and the positive BOLD activation is in blue. From Figure 5.2, it is evident that the area of activation increases with stimulation frequency for both BOLD and $T_{1\rho}$ functional imaging. The size of the activated region as well as the median and maximum t-statistic also reflect this frequency dependency (Table 5.1). It is evident that the BOLD response is substantially larger than the $T_{1\rho}$ response, however there is a high degree of overlap (green voxels shown in Figure 5.2) between the

two responses. The average of the $T_{1\rho}$ and BOLD time course as shown in Figure 5.3 was obtained in the ROI (3x2) within visual cortex across subjects as shown in white color square in Figure 5.2(C). It is observed that the magnitude of the $T_{1\rho}$ response depends on the temporal frequency. In addition, the peak percentage change for $T_{1\rho}$ functional imaging (~2%) was approximately half of the change found using BOLD imaging (~4%). Figure 5.4 shows contrast maps of BOLD and $T_{1\rho}$ response between stimulus frequency of 7Hz, 4Hz, and 1Hz. Both BOLD and $T_{1\rho}$ response significantly increased with the visual stimulation frequency. The ^{31}P data showed a reduction in the estimated pH value in all subjects during the activated state within the voxel encompassing the visual cortex. Figure 5.5 shows brain pH values within visual cortex estimated by ^{31}P spectroscopy. During 4Hz and 7Hz visual stimulation, brain pH significantly decreased (acidosis) relative to the visual fixation (REST) and there was a trend relative to 1Hz visual stimulation ($p=0.08$). pH was slightly reduced at 1Hz relative to REST, but this was not statistically significant. PCr/Pi and ATP/Pi ratios decreased with stimulation frequency but were not statistically significant (Table 5.2).

5.4. Discussion and Conclusions

These results replicate the findings of our previous work that suggested an acidosis within the visual cortex in response to a full field flashing checkerboard using $T_{1\rho}$ functional imaging and ^{31}P spectroscopy [139]. The work herein extends that previous study by finding that the magnitude of the pH response depends on the stimulation frequency and thus likely depends on the associated changes brain activity [143]. This was evident in both the $T_{1\rho}$ and ^{31}P measurements. The magnitude and extent

of the $T_{1\rho}$ response increased significantly with increasing frequency of the flashing checkerboard, which is consistent with a greater acidosis. Consistent with these $T_{1\rho}$ data, ^{31}P spectroscopy also detected a greater acidosis during visual stimulation with the higher temporal frequencies (4 and 7 Hz).

Our BOLD data agree with the findings of Vafaee and Gjedde [147] and Singh et al. [143] suggesting that the cluster size of activated voxel as well as the magnitude of BOLD signal is increased with stimulation frequency within the range studied (1-7Hz). Neurovascular responses of the visual pathway as a function of stimulus frequency have been described for visual stimulation [148]. It is known that the electrical response amplitude induced by the visual stimulus relies on the total number of cortical neurons responding to the stimulus, with the greatest number of neurons responding to stimulus frequency rates (approximately 8Hz, 1/125msec) matching the "activity-recovery cycle" duration (125msec) of the pathway from retina to visual cortex. However, the response amplitude decreases as the temporal frequency of flicker exceeds 8Hz. The stimulus rate-dependent increases in the BOLD signal is consistent with the PET observations for CBF [144].

Our previous study in sheep blood phantoms suggested a double disassociation between $T_{1\rho}$ and BOLD; $T_{1\rho}$ was not sensitive to blood oxygenation while BOLD was not sensitive to pH [139]. Here we also found significant differences in the activation patterns detected by $T_{1\rho}$ and BOLD. While the $T_{1\rho}$ activation area was contained mostly within the BOLD activation area, the $T_{1\rho}$ activation area was significantly smaller. It is well known that the BOLD signal comes mainly from the veins draining blood from the activated areas; thus, BOLD contrast may occur at sites significantly distant from the

actual sites of neuronal activity. This is why some investigators apply small motion sensitizing gradients to the echo-planar gradient echo sequence commonly used to acquire BOLD data. Therefore, we speculate that the smaller $T_{1\rho}$ changes may represent an acidosis that is more localized to the area of brain activity as compared to the BOLD signal. However, we found that the signal change was half of the BOLD magnitude and may require additional temporal sampling to achieve the same power as BOLD imaging.

Lactate is one of the potential sources of acid detected by $T_{1\rho}$ and ^{31}P. Prichard et al. [149], Maddock et al. [120] and Magnotta et al. [139] observed that lactate concentration significantly increases during visual stimulation. Lin et al. [146] also observed that stimulation rate-dependent increase of CBF correlates with lactate production. These observations suggest that anaerobic glycolysis may help drive the pH and CBF responses detected here. Increased activity requires greater blood flow to supply glucose and oxygen and to remove metabolic waste including CO_2. Prior studies have shown that local acidosis is a critical determinant of cerebrovascular tone [150]. Consequently, activity-evoked acidosis may be a key mechanism underlying neurovascular coupling. Nevertheless, current functional imaging paradigms remain dependent on blood flow, blood volume and the vascular anatomy, which limits their temporal and spatial resolution. If pH helps drive the vascular response, then $T_{1\rho}$ may be a more direct and precise method of imaging brain function. If so, one might expect the local pH changes detected by $T_{1\rho}$ to be more localized to the activated region. In addition, the $T_{1\rho}$ response might precede the hemodynamic response detected by BOLD and CBF measures. However, future work is needed to better understand the temporal dynamics of the $T_{1\rho}$ response relative to BOLD and CBF changes.

The activity-evoked pH changes detected here by ^{31}P-spectroscopy required substantially longer imaging times compared to BOLD and $T_{1\rho}$. This additional imaging time pay lead to greater habituation and attenuation of the neuronal activity [151,152,153], and may help explain why ^{31}P did not detect a pH change evoked by 1 Hz or why the pH changes evoked by 4 and 7 Hz did not differ from each other. Consistent with this possibility, with continuous visual stimulation Sappey-Marinier et al. [84] observed a decline in lactate concentration from an initial maximum level.

In conclusion, our study suggests that $T_{1\rho}$ depends on the degree of brain activity. Furthermore, this work suggests a strong relationship between $T_{1\rho}$ and pH estimated by ^{31}P spectroscopy. Consequently, our findings support the hypothesis that dynamic $T_{1\rho}$ imaging detects activity-evoked pH changes. $T_{1\rho}$ imaging has the potential to provide a new functional imaging marker that may be more specific to the area of brain activity. Therefore, it is possible that by non-invasively detecting pH dynamics in the human brain, $T_{1\rho}$ MRI could offer a novel, more direct approach to map brain function. A number of psychiatric and neurological disorders could potentially benefit from the ability to study dynamic pH changes.

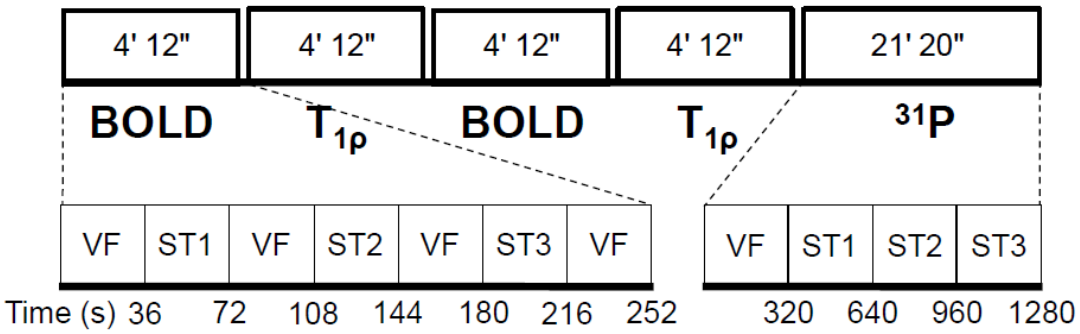

Figure 5.1. Flashing checkerboard paradigms for functional BOLD, $T_{1\rho}$, and ^{31}P spectroscopy studies. BOLD and $T_{1\rho}$imaging were performed twice in an interleaved manner. VF represents a visual fixation. ST1, ST2, ST3 represent visual stimulation with a full field flashing checkerboard at different temporal frequencies of 1, 4, and 7Hz. The temporal frequencies were presented in a random order. During the ^{31}P study, all of the visual stimulation (ST1, ST2, and ST3) and VF were randomly presented.

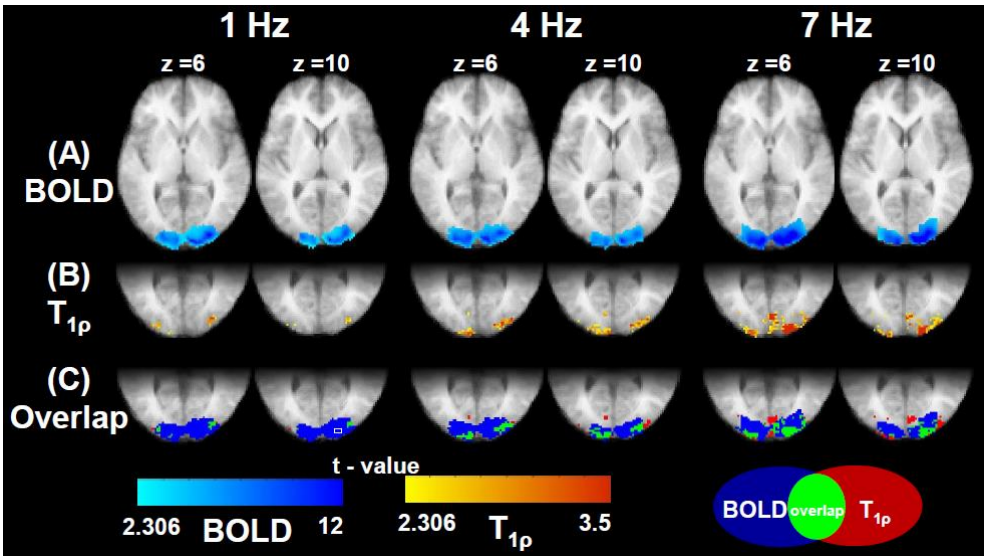

Figure 5.2. BOLD and $T_{1\rho}$ functional activation maps resulting from the different stimulus temporal frequencies. Group analysis of the functional imaging data ($p<0.05$, corrected) for the BOLD and $T_{1\rho}$ at flashing checkerboard frequencies of 1, 4, and 7Hz, respectively. Two axial slices (MNI z=6 and z=10) are shown. Different color scales are used for the BOLD (sky/blue) and $T_{1\rho}$ (yellow/red) are used to display the positive activation for each method. The bottom row shows the overlap (green) between the BOLD and $T_{1\rho}$ results. Voxels responding only to BOLD are shown in blue and those only responding with $T_{1\rho}$ are shown in red.

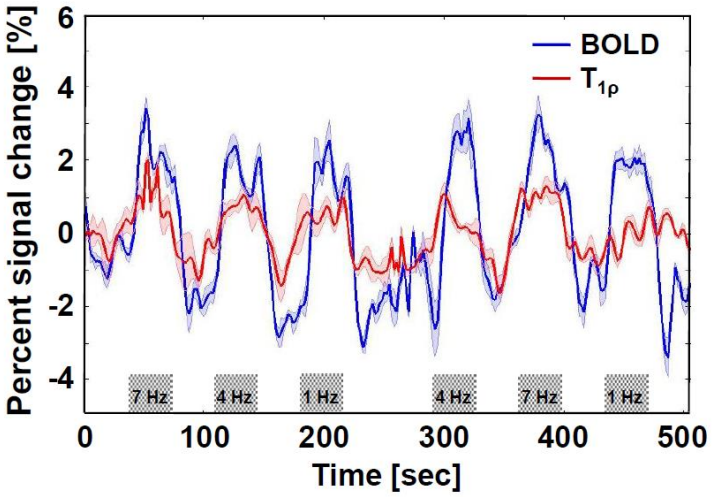

Figure 5.3. Percentage changes of BOLD signal and $T_{1\rho}$ times during different stimulus temporal frequencies. Group-average percent changes of the BOLD (blue line) and $T_{1\rho}$ (red line) time courses obtained in the ROI (3x2) within the visual cortex across subjects as shown in white color square in Figure 5.2(C). Error bars depict standard error of the mean.

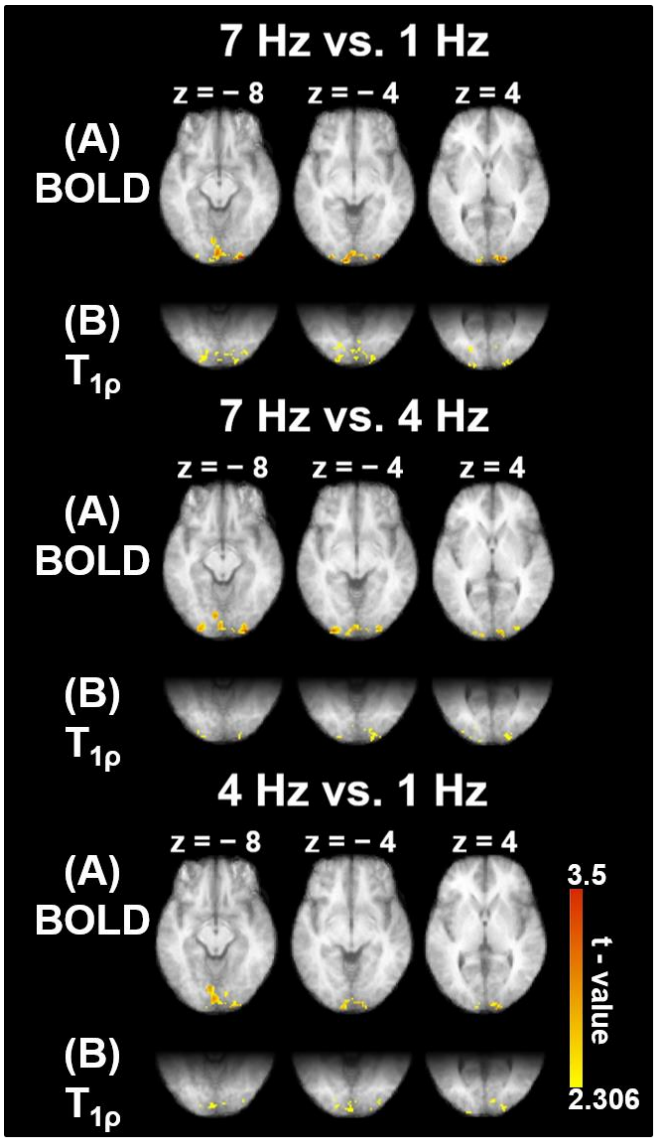

Figure 5.4. BOLD and $T_{1\rho}$ statistical contrast maps (7Hz vs. 1Hz, 7Hz vs. 4Hz, and 4Hz vs. 1Hz). Axial sections of statistical contrast maps ($p<0.05$, corrected) for BOLD (A) and $T_{1\rho}$ (B) response between stimulus frequencies of 7Hz, 4Hz, and 1Hz. Three contiguous slices (MNI $z=-8$, $z=-4$, and $z=4$) are shown.

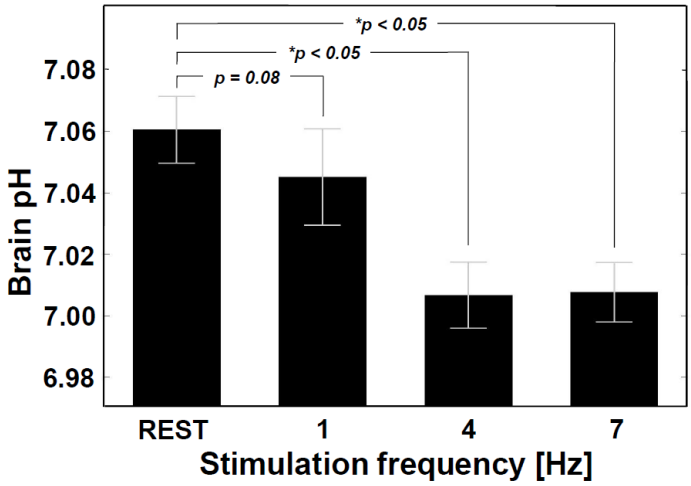

Figure 5.5. Brain pH measurements obtained using ^{31}P spectroscopy during different conditions. Brain pH within the visual cortex averaged across ten subjects. Error bars depict standard error. There was a statistically significant difference between pH during the stimulation at 4 and 7 Hz as compared to REST.

		MNI coordinates			Cluster size	Median t-value	Maximum t-value	p
		x	y	z				
BOLD	1Hz	4	-90	-12	13064	8.7	13.7	<0.05
	4Hz	2	-88	-15	14116	8.6	17.5	<0.05
	7Hz	2	-88	-15	21321	10.1	30.4	<0.05
$T_{1\rho}$	1Hz	-26	-99	-8	26	2.8	4.0	<0.05
	4Hz	22 -2	-91 -101	0 3	162 35	4.4	4.6	<0.05
	7Hz	4 -18	-85 -99	-3 -10	359 128	4.8	6.4	<0.05

Table 5.1. MNI coordinates of the activated cluster center of mass, cluster size, and significance.

Rate	PCr/Pi (% REST)	ATP/Pi (% REST)	pH
REST	100 ± 10.7	100 ± 10.0	7.061 ± 0.011
1 Hz	83.9 ± 13.4	88.67 ± 13.4	7.045 ± 0.015
4 Hz	79.06 ± 11.3	88.41 ± 16.6	7.007 ± 0.010*
7 Hz	76.57 ± 9.3	78.17 ± 9.6	7.008 ± 0.009*

Table 5.2. Phosphate ratios and intracellular pH during different stimulus temporal frequencies.

CHAPTER 6

$T_{1\rho}$ FUNCTIONAL IMAGING TEMPORAL DYNAMICS IN THE HUMAN VISUAL CORTEX

6.1. Background and Rationale

Local dynamic pH fluctuation in the brain occurs with neural activity and has been associated with several neurological and psychiatric disorders. There are a number of potential sources of pH change in the brain and several of these may combine to produce a localized acidosis. Neural activity generates lactate, CO_2 and other metabolites as end products, which lower interstitial pH. In addition, the synaptic release of protons from neurotransmitter vesicles lower pH in the synaptic cleft to modulate pH sensitive channels and other receptors in the pre- and post-synaptic membrane. An increased metabolic activity also produces more CO_2, which is rapidly hydrated to HCO_3^- and H^+. Such dynamic pH fluctuations have the potential to dramatically alter cognition and behavior through a number of pH-sensitive receptors and channels. An example is the acid-sensing ion channels (ASICs), which promote synaptic plasticity, learning, and memory [116,117]. In addition, there is an emerging recognition of the importance of pH and ASICs may play in neurological disease, including stroke, multiple sclerosis, and seizure [19,116]. Recently, increasing evidence suggests that pH may be abnormally regulated in panic disorder [122,154-158]. Furthermore, CO_2 inhalation triggers panic attacks and patients with panic disorder are particularly sensitive [18] The resulting acidosis is thought to be responsible for most of the physiological effects of CO_2. These

finding suggest a critical role for pH-dependent signaling in psychiatric and neurological disease. In addition, neural activity is accompanied by a complex sequence of vascular processes. A continuous supply of energy substrates such as glucose and oxygen is maintained by cerebral blood flow during the neural activity. Prior studies have shown that local acidosis is a critical determinant of cerebrovascular tone [150]. Local acidosis potently stimulates vasodilation and increases blood flow. Therefore brain tissue acidosis accounts for the vasodilation associated with increased neuronal activity.

The ability to non-invasively measure pH dynamics may also offer a novel, more direct approach to map brain function. Brain acidosis is the end product of energy metabolism. Metabolically active cells lower local pH, the detection of which could help pinpoint regions activated by sensory stimuli, emotion, or cognitive tasks. Functional magnetic resonance imaging (fMRI) mostly relies on blood oxygenation-level dependent (BOLD) changes in the venous system while arterial spin labeling (ASL) enables changes in tissue perfusion resulting from local cerebral blood flow (CBF) changes. BOLD contrast can be significantly distant from the actual site of neuronal activity because it relies on changes of the local magnetic field within veins [43,159,160]. The venous contribution results in a loss of spatial specificity and spatial resolution of the BOLD response [161]. In addition, the hemodynamic response to brief periods of neural activity is delayed. Typically, the signal change is observed at 3-5 seconds after onset of neural activation and reaches maximum at 5-10 seconds [162,163]. However, ASL contrast originates predominantly from tissue and capillaries [54,60,164]. Even though functional signal changes detected by ASL have superior spatial and temporal resolution as compared to BOLD contrast, ASL contrast still suffers from poor temporal resolution due

to delays in the hemodynamic response resulting from neurovascular coupling. Therefore, the ability to measure pH dynamics may provide a more localized and direct measure of brain activity.

Recently, we found that the $T_{1\rho}$ contrast can detect dynamic fluctuations in pH associated with brain activity resulting from a visual flashing checkerboard [139]. Both the $T_{1\rho}$ and ^{31}P spectroscopy measurements revealed an acidosis in the visual cortex associated with brain activity. In addition, we found a significant increase in the lactate signal (lactate/creatine ratio) using ^{1}H spectroscopy within the visual cortex. Blood phantoms revealed that $T_{1\rho}$ was sensitive to pH changes and not blood oxygenation while T_2^* was sensitive to blood oxygenation and not pH. It suggests that $T_{1\rho}$ contrast dissociates from BOLD sensitivity. Consequently, functional $T_{1\rho}$ imaging may provide improve localization of brain activity and more direct approach to map brain function since acidic end product of metabolism, lactic acid, are likely more localized to the brain activity as compared to blood oxygenation. Currently, various magnetic resonance approaches have been developed to measure brain pH. ^{31}P spectroscopy is most commonly used to measure brain pH with pH-dependent chemical shift changes, but it has relatively poor temporal and spatial resolution [135,136]. Recently, ^{1}H MRI methods for measuring pH in vivo have exploited pH-dependent magnetization transfer between bulk water and amid protons in the peptide bonds [92,93,99]. This technique includes amid proton transfer (APT) imaging technique, a specific variant of chemical exchange saturation transfer (CEST). APT is pH-sensitive but has not yet been developed for functional imaging.

In this study, we hypothesized that pH-sensitive $T_{1\rho}$ response in the visual cortex will temporally precede the hemodynamic response measured by functional imaging including BOLD and ASL contrast since local acidosis evoked by neural activity may drive the hemodynamic response. To test this hypothesis, dynamic imaging was performed using $T_{1\rho}$, BOLD, and ASL while viewing a phase-encoded expanding ring stimulus, which induces traveling waves of neural activity in the visual cortex. We calculated the phase maps for the eccentricity across their occipital cortices for each of functional signal and compared the $T_{1\rho}$ temporal resolution with the hemodynamic response.

6.2. Methods

Five subjects (three men and two women, 29-33 years of age) underwent MRI (T_1 and T_2-weighted imaging) and fMRI (BOLD, ASL, and $T_{1\rho}$) study, all with normal or corrected-to-normal vision. Signed informed consent was obtained prior to beginning the study in accordance with the Institutional Review Board at the University of Iowa.

MR images of the brain were obtained on a 3.0T Siemens TIM Trio scanner (Siemens Medical Solutions, Erlangen, Germany) using a 12 channel head-coil. For cortical surface reconstruction, high-resolution anatomical T_1-weighted images were acquired using a 3D MP-RAGE sequence using the following parameters: TR=2530ms, TE=2.8ms, TI=909ms, flip angle=10°, FOV=256x256x256mm, matrix size=256x256x256, bandwidth= 180Hz/pixel. BOLD imaging was performed using a T_2^*-weighted gradient-echo sequence with the following acquisition parameters: TR=2500ms, TE=30ms, flip angle=90°, FOV=220x220mm, matrix size=64x64,

bandwidth=2004Hz/pixel, 31 slices and slice thickness/gap=4.0/1.0mm. $T_{1\rho}$ imaging was performed using an echo-planar spin-echo sequence with an additional $T_{1\rho}$ spin-lock encoding pulse. The sequence parameters were TR=2500ms, TE=12ms, FOV=220x220mm, matrix size=64x64, bandwidth=1954Hz/pixel, 15 slices and slice thickness/gap=4.0/1.0mm. Two spin-lock pulses were used (10 and 40ms) with a spin-lock frequency of 350Hz. Pulsed ASL (PICORE Q2T) images were collected by alternating between tag and control images using the following parameters: TR=2500ms, TE=15ms, TI1/TI2=700/1602ms, FOV=220x220ms, matrix size=64x64, 12 slices and slice thickness/gap=4/1mm. Two runs of the ASL and $T_{1\rho}$ measurements were obtained to increase signal to noise ratio. 3D shimming was performed for all functional scans using Siemens's automatic shimming routine.

Phase-encoded eccentric maps were presented using a standard expanding ring stimuli that induce travelling waves of neural activity in the visual cortex [165-167]. Eccentricity mapping was performed using expanding ring checkerboard presented in 6 cycles with 50 second period (0.02Hz) for each of three functional modalities. When the ring reaches the maximum eccentricity, it wraps around to be replaced by a new one at minimum eccentricity. The temporal frequency of 50 seconds for eccentricity stimulation allowed the signal to return to baseline before subsequent activations. The stimulus patterns were based on a radial high-contrast black and white checkerboard flickering at 8Hz. The stimulus was presented on a screen of width 40cm, height 30cm, and a distance of approximately 80cm form the subject's eye. Subjects viewed the screen through a mirror attached to the head coil. A deep red colored circle was shown in the center of the stimulus. Subjects were asked to press a button on the fiber optic response system (Lumin

LP-400, Cedrus Corporation, San Pedro, USA) when the deep red colored circle changed to the bright red colored circle, which was appeared in random order. This was done to ensure that the subjects maintained fixation on the center throughout the stimulus presentation. Six dummy scans (6TR=15sec) were collected at the beginning of each run to reach steady state magnetization before initiating the eccentricity mapping stimulus. The stimuli were generated using MATLAB (The MathWorks, Inc., Natick, MA, USA) and the Psychophysics Toolbox [168,169].

The cortical surface of each subject was reconstructed from the high-resolution T_1-weighted images transformed using Freesurfer [170-172]. The FreeSurfer pipeline is first performs tissue classification before separating the hemispheres and generating a separate surface for each hemisphere. The occipital lobe was flattened by cutting the inflated surface along the calcarine fissure.

All functional imaging data were analyzed using a combination of AFNI [173], SUMA(http:/afni.nimh.nih.gov/afni/suma) and additional custom-written MATLAB and Linux shell scripts. Pre-processing for all functional data included slice timing correction, linear trend removal, and three dimensional motion correction. The functional data were detrended with components of no interest from time series volumes using a third order polynomial. For ASL data, we calculated control-tag difference images using surround subtraction to reduce BOLD signal contamination of the CBF time course [60]. For $T_{1\rho}$ data, $T_{1\rho}$ relaxation times were calculated from the images with TSL of 10ms and 40ms, by voxel-wise fitting to mono-exponential decay. In addition, time series of all functional data were high-pass filtered to remove low frequency drifts caused by subject motion and physiological noise. The voxel-wise phase and amplitude of neuronal responses for all

functional modalities was estimated by taking the Fourier transform of the time series at the stimulus frequency (0.02Hz=1/50sec). Functional activation maps (phase and coherence) were resampled into matrices with 1 mm resolution to match the source data for cortical surfaces. Image alignment between the functional activation maps and 3D anatomical MP-RAGE was performed, and then mapped to the cortical surface. The phase data were smoothed with a Gaussian kernel of 8mm FWHM along the cortical surface. The phase maps are represented in the color scale between 0 and 2π for the phase values.

For each voxel, we calculated an F ratio and corresponding p-values by dividing the squared amplitude of the response at the fundamental stimulus frequency (0.02Hz) with the average squared amplitudes at all other frequencies except the signal at the DC component frequency. For each subject, the statistical map of BOLD eccentricity was thresholded ($p<0.01$) and an ROI was created including significantly activated voxels for eccentricity maps. The statistical maps of ASL and $T_{1\rho}$ eccentricity were masked with the same ROI created from the BOLD signal, and were threshold ($p<0.05$) because of the lower SNR of ASL and $T_{1\rho}$ images.

Region of interest analysis was performed for BOLD, ASL, and $T_{1\rho}$ time courses. ROIs (2x2 pixels) enclosing the primary visual cortex (V1) were carefully drawn on the functional maps with reference to the flattened cortical surface. Normalized signal changes of individual functional signals in two representative subjects were obtained from the ROIs across all three functional imaging methods. The signal was normalized to ±1.

For temporal resolution comparison of all three modalities, we subtracted the phase map between the BOLD and ASL, between the BOLD and $T_{1\rho}$, and between the ASL and $T_{1\rho}$. All subtraction images were masked with the ROI created from the BOLD signal thresholded ($p<0.01$), and converted to time scale.

For each ROI, the phase values between the measured time-series and best-fit sinusoidal function were calculated, which measures temporal delay of the fMRI responses relative to the beginning of the time-series. The BOLD, ASL, and $T_{1\rho}$ time series were each individually averaged over one period relative to their peak activation. The first and last cycle of the time series were discarded before averaging.

6.3. Results

Figure 6.1 shows eccentricity maps of BOLD, ASL, and $T_{1\rho}$ response to the expanding ring stimulus on the left and right inflated hemisphere, and the left flattened cortical surface for a single subject. The color scale indicates the raw phase value between 0 and 2π for eccentricity map. All eccentricity maps show a systematic increase in phase originating from the occipital pole towards more anterior regions. However, in the eccentricity maps, where the fovea is denoted in red/ yellow and the periphery in blue/ green, the phase lag for $T_{1\rho}$ was smaller than these for ASL and BOLD, implying an earlier $T_{1\rho}$ response. Figure 6.2 shows eccentricity maps of BOLD, ASL, and $T_{1\rho}$ response to the expanding ring stimulus on the left inflated cortical surface for the four other subjects (S2, S3, S4, and S5). Both the BOLD and ASL responses show strong eccentric patterns for the specified significance levels (0.01 and 0.05 respectively). The $T_{1\rho}$ imaging had a weaker response. Figure 6.3A and Figure 6.5A show the eccentricity

map of BOLD, ASL, and $T_{1\rho}$ response on their sagittal (upper) and axial (lower) functional data for two representative subjects (S1 and S2), showing the phase map between 0 and 2π. The phase-differences between BOLD, ASL, and $T_{1\rho}$ eccentricity maps are also apparent in the time courses as shown in Figure 6.3B and 6.5B. The average of the BOLD, ASL, $T_{1\rho}$ time course as shown in Figure 6.3B and 6.5B were obtained in the ROI (2x2) within visual cortex for the subject (S1 and S2) as shown by black color square in Figure 6.3A and 6.5A. The $T_{1\rho}$ signal (red) change appears to precede the ASL (blue) signal, followed by BOLD (black) signal. It would suggest that the $T_{1\rho}$ signal has a higher temporal resolution as compared to the BOLD and ASL response. Figure 6.3C and 6.5C shows the subtracted time delay maps between the BOLD and the ASL, and between the BOLD and the $T_{1\rho}$, and between the ASL and the $T_{1\rho}$. Figure 6.3D and 6.5D shows the averaged BOLD, ASL, and $T_{1\rho}$ across the entire time course. Although the BOLD and ASL temporal dynamics were quite similar, there was a trend towards ASL preceding the BOLD changes. $T_{1\rho}$ signal responded faster than ASL, which precedes the BOLD signal by 1-2 seconds. $T_{1\rho}$ signal peaked faster than the BOLD and ASL. However, the $T_{1\rho}$ did tend to decay slower than BOLD and ASL. All three modalities tended to reach settle back to the baseline at about the same time. Figure 6.3E shows the best fit of sinusoidal function for the BOLD, ASL, and $T_{1\rho}$. Figure 6.4 and 6.6 show the hemodynamic response delay of BOLD and ASL relative to $T_{1\rho}$ response for the subject (S1 and S2). Red circles represent data thresholded by F ratio of 5.29 (p-value<0.01). The phase lag for $T_{1\rho}$ was smaller than these for BOLD and ASL in the voxels with high statistically significance (red circles). The difference between BOLD and ASL delay times, between BOLD and $T_{1\rho}$, and between ASL and $T_{1\rho}$ delay times

across all subjects is shown in Figure 6.7A. The mean difference between all imaging modalities is shown in Figure 6.7B. The corresponding difference of delay times are listed in Table 6.1.

6.4. Discussion and Conclusions

In this study, we used the phase-encoded visual stimulation with a 50 sec period to compare the temporal resolution between $T_{1\rho}$, BOLD, and ASL response. The occipital cortex was used as a model system for this study. Our data suggests that the $T_{1\rho}$ signal has a higher temporal resolution as compared to the hemodynamic response. Recently, we found that $T_{1\rho}$ contrast can used to detect dynamic fluctuations in pH associated with brain activity resulting from a visual flashing checkerboard [139]. These findings were supported using ^{31}P spectroscopy. In addition, we have shown that the $T_{1\rho}$ changes are independent of blood oxygenation. Therefore we hypothesized that activity-evoked pH changes and pH-sensitive $T_{1\rho}$ signal in the visual cortex will precede the hemodynamic response. Based on our data, $T_{1\rho}$ may respond up to 4 seconds faster than ASL and BOLD. This study also found that dynamic $T_{1\rho}$ signal responds faster than ASL. The hemodynamic delay time between BOLD and ASL signal for distinct visual area are consistent with these reported in the literature [174].

Neural activity and cerebral blood flow are closely coupled, which is called neurovascular coupling [150]. Increases in oxygen and glucose consumption during neural activity are followed by an increase in CBF. In addition, the cerebral blood flow is controlled by feedback mechanisms, which are correlated with the concentration of metabolic by-products such as nitric oxide, adenosine, carbon dioxide, and arachidonic

acid metabolites. Prior studies have shown that local acidosis may alter blood flow by depolarizing the vascular smooth muscle cells which triggers vasodilation [150]. Consequently, activity-evoked acidosis may be a key mechanism underlying neurovascular coupling. Nevertheless, current functional imaging paradigms are limited by their dependence on blood flow, blood volume, and the vascular anatomy, which limits their temporal and spatial resolution. However, $T_{1\rho}$ could be a more direct and precise method of imaging brain functions because acidic end products of metabolism are a likely source of pH, driving the vascular response. Furthermore, $T_{1\rho}$ response might precede the hemodynamic response detected by BOLD and CBF, because pH may drive the hemodynamic response.

We found significant differences in the eccentric patterns detected by $T_{1\rho}$, BOLD, and ASL. It is well known that the BOLD signal is primarily caused by oxygenation and volume changes in veins, which can spread the fMRI-detected area to region where there are no neuronal activation whereas ASL is more closely associated with the capillary bed [54,60,164]. It has been suggested that the hemodynamic response is delayed in the more downstream and the larger the vasculature is, with delays ranging between 2 sec in the parenchyma to 14 sec in the large draining veins [162,163]. Therefore, these different spatial locations and hemodynamic response delay contribute to the observed discrepancy between ASL and BOLD phase maps. While the $T_{1\rho}$ activation area was contained mostly within the BOLD and ASL activation area, the $T_{1\rho}$ activation area was significantly smaller. This would be expected if the $T_{1\rho}$ signal is generated from pH changes associated with local brain activity. However, the significant activated region in the $T_{1\rho}$ eccentric map was found mostly in the primary visual area (V1). Other regions had a

lower signal to noise ratio. We found that the signal change was half of the BOLD magnitude and may require additional temporal sampling to achieve the same power as BOLD imaging.

In conclusion, we performed the eccentric mapping of the human brain at 3T using the expanding ring stimulus to assess the temporal dynamic of $T_{1\rho}$ relative to BOLD and ASL. Our study suggests that $T_{1\rho}$ signal has a higher temporal resolution as compared to the hemodynamic response. This is further evidence that the $T_{1\rho}$ signal is not sensitive to blood oxygenation or other blood factors that might alter $T_{1\rho}$. Therefore, our findings support the hypothesis that dynamic $T_{1\rho}$ imaging detects activity-evoked pH changes. $T_{1\rho}$ imaging could be used to map neural activation more precisely than blood flow dependent methods. Furthermore, a number of psychiatric and neurological disorders could potentially benefit from the ability to study dynamic pH changes.

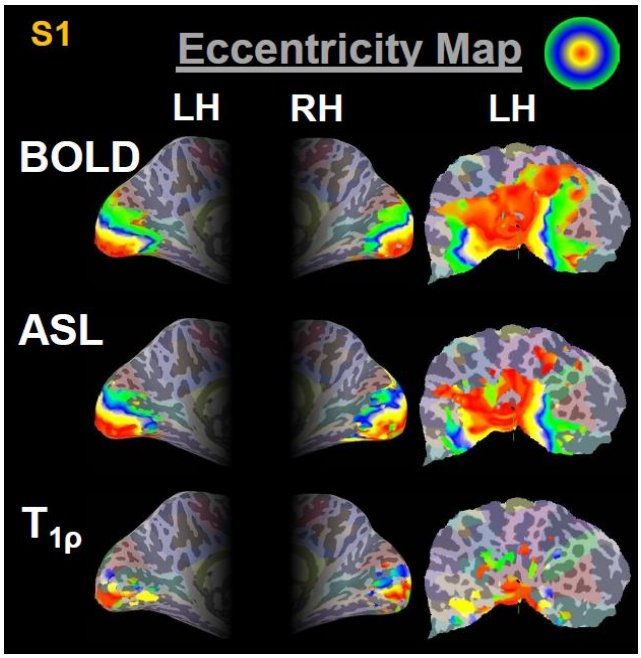

Figure 6.1. Eccentricity maps of BOLD, ASL, and $T_{1\rho}$ response to the expanding ring stimulus on the left and right inflated hemisphere, and the left flattened brain surface for single subject (S1). The color scale indicates the raw phase value between 0 and 2π for eccentricity map. The red color indicates regions corresponding to the center of field of view, while the green color regions correspond to the outer eccentric degrees.

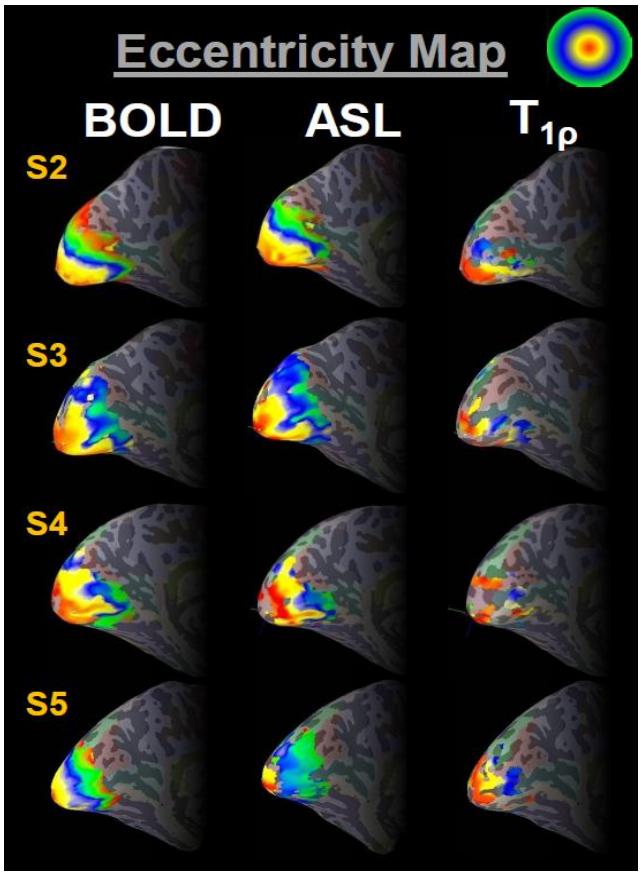

Figure 6.2. Eccentricity maps of BOLD, ASL, and $T_{1\rho}$ response to the expanding ring stimulus on the left inflated hemisphere for four subjects (S2-S5). The color scale indicates the phase lag between 0 and 2π for eccentricity map. The red color indicates regions corresponding to the center of field of view, while the green color regions correspond to the outer eccentric degrees.

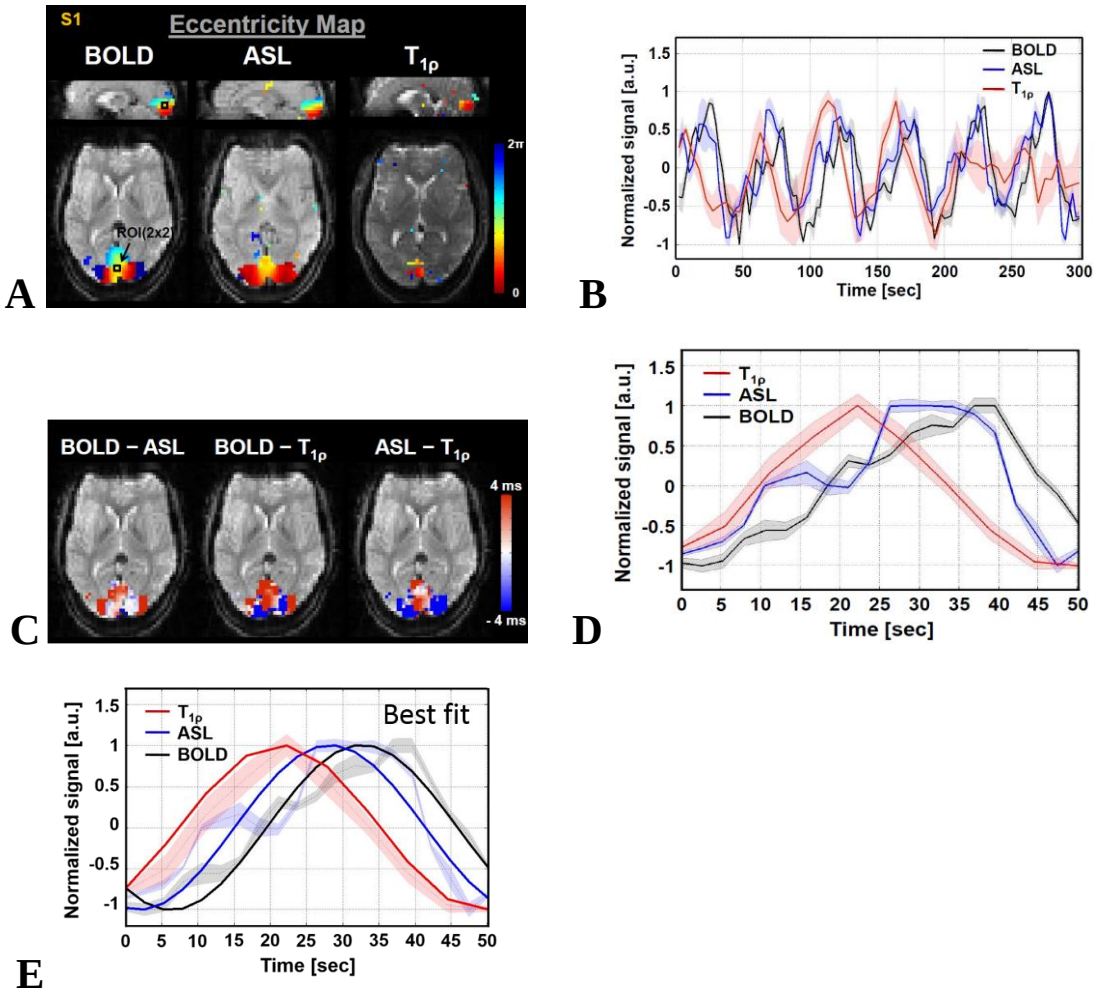

Figure 6.3. Eccentricity maps and normalized signal changes of BOLD, ASL, and $T_{1\rho}$ response. (A) Phase maps of BOLD, ASL, and $T_{1\rho}$ response on the sagittal (upper) and axial (lower) functional data for a representative subject (S1). (B) Averaged signal changes of the BOLD, ASL, and $T_{1\rho}$ time courses. (C) Time delay subtraction images between the BOLD, the ASL and the $T_{1\rho}$. (D) Averaged signal changes of the BOLD, ASL, and $T_{1\rho}$ time courses for one period, which were shifted by calculated phase offset. (E) Best fit of sinusoidal function for the BOLD (black line), ASL (blue line), and $T_{1\rho}$ (red line) time courses for one period

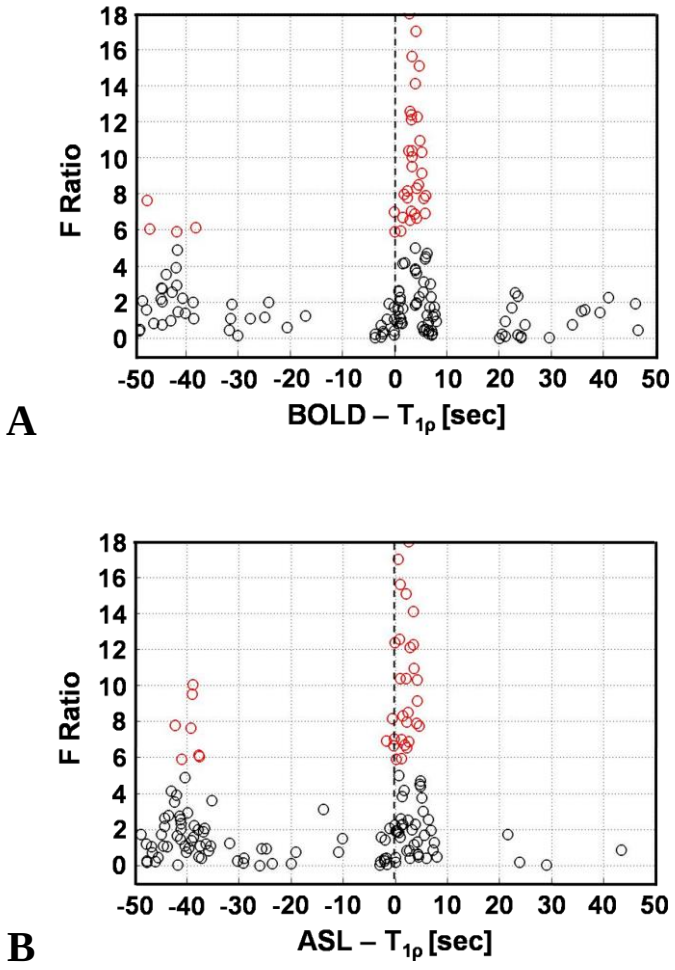

Figure 6.4. Hemodynamic response delay of BOLD and ASL relative to $T_{1\rho}$ response. (A) Time lag between BOLD and $T_{1\rho}$ response. (B) Time lag between ASL and $T_{1\rho}$ response for a representative subject (S1). Red circles represent data thresholded by F ratio of 5.29. Note that F ratio of 5.29 corresponds to p-value of 0.01.

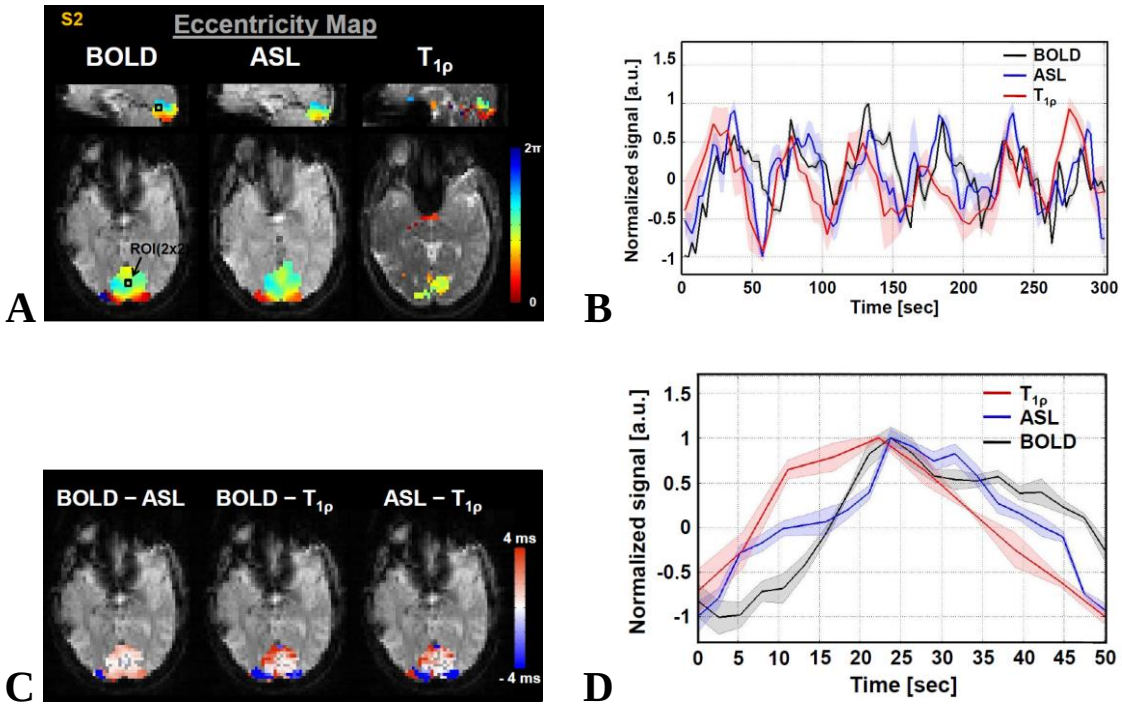

Figure 6.5. Eccentricity maps and normalized signal changes of BOLD, ASL, and $T_{1\rho}$ response. (A) Phase maps of BOLD, ASL, and $T_{1\rho}$ response on the sagittal (upper) and axial (lower) functional data for a representative subject (S2). (B) shows averaged signal changes of the BOLD (black line), ASL (blue line), and $T_{1\rho}$ (red line) time courses obtained in the ROI (2x2) within the primary visual cortex in the subject (S1) as shown in black color square in figure 4A. (C) Time delay subtraction images between the BOLD and the ASL (left) and the BOLD and the $T_{1\rho}$ (middle) and the ASL and the $T_{1\rho}$ (right). (D) Averaged signal changes of the BOLD (black line), ASL (blue line), and $T_{1\rho}$ (red line) time courses for one period, which were shifted by calculated phase offset. Error bars depict standard deviation.

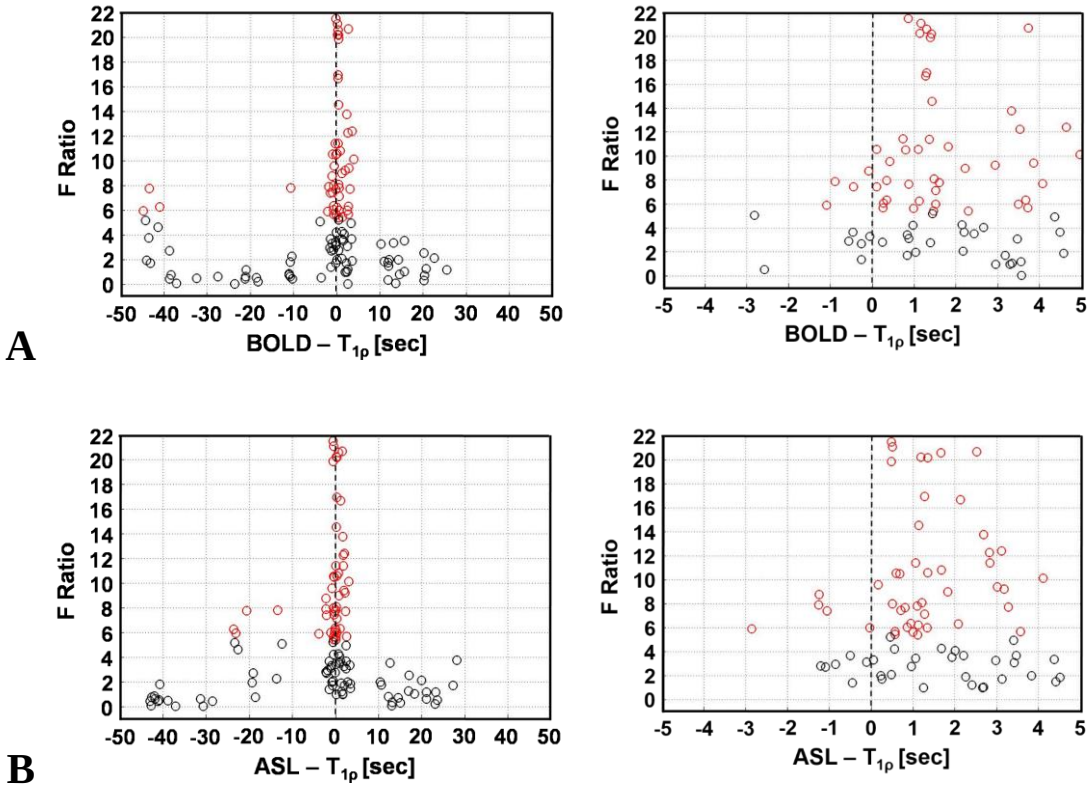

Figure 6.6. Hemodynamic response delay of BOLD and ASL relative to $T_{1\rho}$ response. (A) Time lag between BOLD and $T_{1\rho}$ response. (B) Time lag between ASL and $T_{1\rho}$ response for a representative subject (S2). Red circles represent data thresholded by F ratio of 5.29. Note that F ratio of 5.29 corresponds to p-value of 0.01.

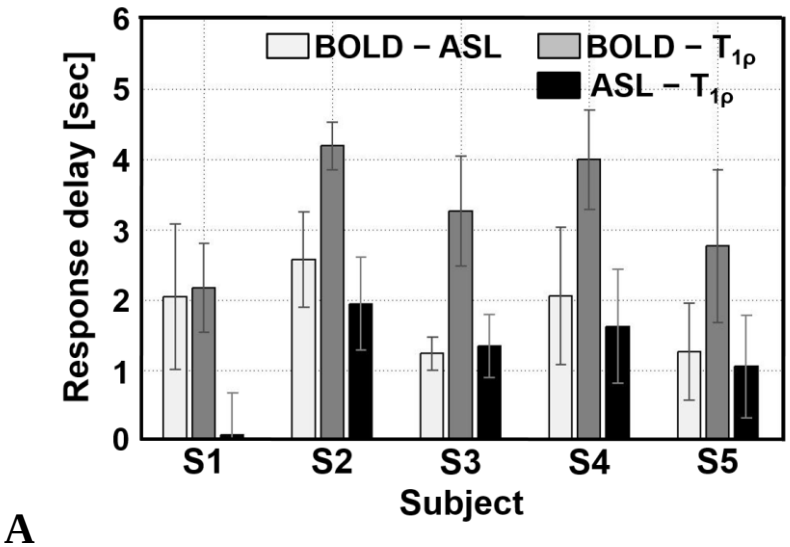

A

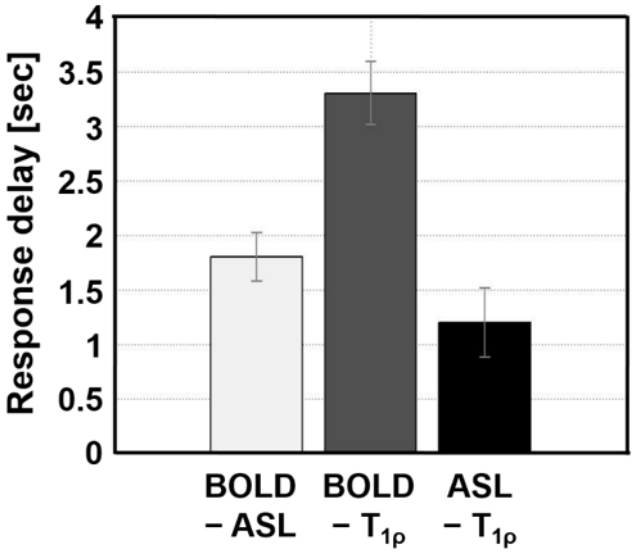

B

Figure 6.7. Difference of the response delay times between BOLD and ASL, between BOLD and $T_{1\rho}$, between ASL and $T_{1\rho}$. (A) The first bars represent the difference of the time lag between BOLD and ASL, the second bars represent the difference of the time lag between BOLD and $T_{1\rho}$, and the third bars represent the difference of the time lag between ASL and $T_{1\rho}$. Error bars depict standard error. (B) Mean difference of the response delay across all subjects.

	S1	S2	S3	S4	S5	Mean
BOLD – ASL [sec]	2.04 ± 1.03	2.57 ± 0.68	1.23 ± 0.24	2.05 ± 0.98	1.26 ± 0.69	1.8 ± 0.74
BOLD – $T_{1\rho}$ [sec]	2.17 ± 0.63	4.18 ± 0.34	3.26 ± 0.78	3.99 ± 0.71	2.76 ± 1.09	3.3 ± 0.97
ASL – $T_{1\rho}$ [sec]	0.07 ± 0.60	1.94 ± 0.66	1.34 ± 0.45	1.62 ± 0.81	1.05 ± 0.73	1.2 ± 0.64

Table 6.1. Difference and mean of the response delay times between BOLD and ASL, between BOLD and $T_{1\rho}$, and between ASL and $T_{1\rho}$.

CHAPTER 7

DISCUSSION AND CONCLUSION

The major findings of this study are: 1) $T_{1\rho}$ detects a localized acidosis in the human visual cortex induced by a flashing checkerboard task. 2) $T_{1\rho}$ depends on the degree of brain activity. 3) $T_{1\rho}$ response temporally precedes the hemodynamic response measured by BOLD and ASL. Firstly, we found that $T_{1\rho}$ contrast can detect dynamic fluctuations in pH associated with brain activity resulting from a visual flashing checkerboard. Both the $T_{1\rho}$ and ^{31}P measurements revealed a local acidosis in the visual cortex associated with brain activity. In addition, a significant increase in lactate signal using ^{1}H spectroscopy within the visual cortex was observed. BOLD signal originates in the venous system, which results in spatial displacement of the signal from the actual site of brain activity. Therefore functional $T_{1\rho}$ imaging may provide improved localization of brain activity since acidic end products of metabolism, lactic acid, are likely more localized to the brain activity as compared to blood oxygenation. In addition, it is observed that the magnitude and extent of the $T_{1\rho}$ response increased significantly with increasing frequency of the flashing checkerboard, which is consistent with a greater acidosis. Consistent with these $T_{1\rho}$ data, ^{31}P spectroscopy also detected a greater acidosis during visual stimulation with the higher temporal frequencies. These observations suggest that the magnitude of the $T_{1\rho}$ and pH response depends on stimulation frequency and is thus likely to be activity-dependent. Lastly, we found that activity-evoked pH changes and pH-sensitive $T_{1\rho}$ signal in the visual cortex precede the hemodynamic response.

In conclusion, my findings support the hypothesis that dynamic $T_{1\rho}$ imaging detects activity-evoked pH changes. $T_{1\rho}$ MRI might provide a means for more precisely mapping brain activity. Furthermore, a number of psychiatric and neurological disorders could potentially benefit from the ability to study dynamic pH changes.

REFERENCES

1 Friese, M. A. *et al.* Acid-sensing ion channel-1 contributes to axonal degeneration in autoimmune inflammation of the central nervous system. *Nat Med* 13, 1483-1489, doi:Doi 10.1038/Nm1668 (2007).

2 Urbanics, R., Leniger-Follert, E. & Lubbers, D. W. Time course of changes of extracellular H+ and K+ activities during and after direct electrical stimulation of the brain cortex. *Pflugers Archiv : European journal of physiology* 378, 47-53 (1978).

3 Somjen, G. G. Acidification of Interstitial Fluid in Hippocampal-Formation Caused by Seizures and by Spreading Depression. *Brain Res* 311, 186-188 (1984).

4 Simon, R. P., Benowitz, N., Hedlund, R. & Copeland, J. Influence of the Blood-Brain Ph Gradient on Brain Phenobarbital Uptake during Status Epilepticus. *J Pharmacol Exp Ther* 234, 830-835 (1985).

5 Simon, R. P., Bronstein, J. M., Lewis, A. & Benowitz, N. Effects of Status Epilepticus on Brain Uptake of Phenobarbital. *T Am Neurol Assoc* 106, 184-186 (1981).

6 Simon, R. P., Copeland, J. R., Benowitz, N. L., Jacob, P. & Bronstein, J. Brain Phenobarbital Uptake during Prolonged Status Epilepticus. *J Cerebr Blood F Met* 7, 783-788 (1987).

7 Chesler, M. & Chan, C. Y. Stimulus-Induced Extracellular Ph Transients in the Invitro Turtle Cerebellum. *Neuroscience* 27, 941-948 (1988).

8 Chesler, M. & Kaila, K. Modulation of Ph by Neuronal-Activity. *Trends Neurosci* 15, 396-402 (1992).

9 Kuschinsky, W. Coupling of function, metabolism, and blood flow in the brain. *Neurosurgical review* 14, 163-168 (1991).

10 Ursino, M. Mechanisms of cerebral blood flow regulation. *Critical reviews in biomedical engineering* 18, 255-288 (1991).

11 Villringer, A. Understanding functional neuroimaging methods based on neurovascular coupling. *Advances in experimental medicine and biology* 413, 177-193 (1997).

12 Dirnagl, U. Metabolic aspects of neurovascular coupling. *Advances in experimental medicine and biology* 413, 155-159 (1997).

13 Ballanyi K, K. K. Activity-evoked changes in intracellular pH. In: Kaila K, Ransom B (eds) pH and brain function. *Wiley- Liss*, 291–308 (1998).

14 Kaila, K. & Ransom, B. R. *pH and brain function*. (Wiley-Liss, 1998).

15 Roy, C. S. & Sherrington, C. S. On the Regulation of the Blood-supply of the Brain. *The Journal of physiology* 11, 85-158 117 (1890).

16 Harper, A. M. & Bell, R. A. The Effect of Metabolic Acidosis and Alkalosis on the Blood Flow through the Cerebral Cortex. *Journal of neurology, neurosurgery, and psychiatry* 26, 341-344 (1963).

17 Esquivel, G., Schruers, K. R., Maddock, R. J., Colasanti, A. & Griez, E. J. Acids in the brain: a factor in panic? *Journal of psychopharmacology* 24, 639-647, doi:10.1177/0269881109104847 (2010).

18 Zandbergen, J., Pols, H., De Loof, C., Lousberg, H. & Griez, E. Effect of hypercapnia and other disturbances in the acid-base-balance on panic disorder. *Hillside J Clin Psychiatry* 11, 185-197 (1989).

19 Wemmie, J. A. *et al.* The acid-activated ion channel ASIC contributes to synaptic plasticity, learning, and memory. *Neuron* 34, 463-477 (2002).

20 Wemmie, J. A. *et al.* Acid-sensing ion channel 1 is localized in brain regions with high synaptic density and contributes to fear conditioning. *The Journal of neuroscience : the official journal of the Society for Neuroscience* 23, 5496-5502 (2003).

21 Xiong, Z. G. *et al.* Neuroprotection in ischemia: blocking calcium-permeable acid-sensing ion channels. *Cell* 118, 687-698, doi:10.1016/j.cell.2004.08.026 (2004).

22 Rehncrona, S. Brain acidosis. *Annals of emergency medicine* 14, 770-776 (1985).

23 Nedergaard, M., Kraig, R. P., Tanabe, J. & Pulsinelli, W. A. Dynamics of interstitial and intracellular pH in evolving brain infarct. *The American journal of physiology* 260, R581-588 (1991).

24 Bloch, F. The Principle of Nuclear Induction. *Science* 118, 425-430, doi:10.1126/science.118.3068.425 (1953).

25 Purcell, E. M. Nuclear Magnetism in Relation to Problems of the Liquid and Solid States. *Science* 107, 433-440, doi:10.1126/science.107.2783.433 (1948).

26 Sepponen, R. E., Pohjonen, J. A., Sipponen, J. T. & Tanttu, J. I. A method for T1 rho imaging. *Journal of computer assisted tomography* 9, 1007-1011 (1985).

27 Redfield, A. G. Nuclear spin thermodynamics in the rotating frame. *Science* 164, 1015-1023, doi:10.1126/science.164.3883.1015 (1969).

28 Abragam, A. *The principles of nuclear magnetism*. (Clarendon Press, 1961).

29 Garwood, M. & DelaBarre, L. The return of the frequency sweep: designing adiabatic pulses for contemporary NMR. *Journal of magnetic resonance* 153, 155-177, doi:10.1006/jmre.2001.2340 (2001).

30 Tannus, A. & Garwood, M. Adiabatic pulses. *Nmr Biomed* 10, 423-434 (1997).

31 Solomon, I. Rotary Spin Echoes. *Phys Rev Lett* 2, 301-302 (1959).

32 Duvvuri, U. *et al.* Water magnetic relaxation dispersion in biological systems: the contribution of proton exchange and implications for the noninvasive detection of cartilage degradation. *Proceedings of the National Academy of Sciences of the United States of America* 98, 12479-12484, doi:10.1073/pnas.221471898 (2001).

33 Blicharski, J. S. Nuclear magnetic relaxation in the rotating frame. *Acta Phys. Polon* A 223–236 (1972).

34 Makela, H. I., Grohn, O. H., Kettunen, M. I. & Kauppinen, R. A. Proton exchange as a relaxation mechanism for T1 in the rotating frame in native and immobilized protein solutions. *Biochemical and biophysical research communications* 289, 813-818, doi:10.1006/bbrc.2001.6058 (2001).

35 Charagundla, S. R., Stolpen, A. H., Leigh, J. S. & Reddy, R. Off-resonance proton T1rho dispersion imaging of 17O-enriched tissue phantoms. *Magnetic resonance in medicine : official journal of the Society of Magnetic Resonance in Medicine / Society of Magnetic Resonance in Medicine* 39, 588-595 (1998).

36 Tailor, D. R., Poptani, H., Glickson, J. D., Leigh, J. S. & Reddy, R. High-resolution assessment of blood flow in murine RIF-1 tumors by monitoring uptake of H(2)(17)O with proton T(1rho)-weighted imaging. *Magnetic resonance in medicine : official journal of the Society of Magnetic Resonance in Medicine / Society of Magnetic Resonance in Medicine* 49, 1-6, doi:10.1002/mrm.10375 (2003).

37 Tailor, D. R. *et al.* Indirect 17(O)-magnetic resonance imaging of cerebral blood flow in the rat. *Magnetic resonance in medicine : official journal of the Society of Magnetic Resonance in Medicine / Society of Magnetic Resonance in Medicine* 49, 479-487, doi:10.1002/mrm.10403 (2003).

38 Ogawa, S. & Lee, T. M. Magnetic resonance imaging of blood vessels at high fields: in vivo and in vitro measurements and image simulation. *Magnetic resonance in medicine : official journal of the Society of Magnetic Resonance in Medicine / Society of Magnetic Resonance in Medicine* 16, 9-18 (1990).

39 Ogawa, S., Lee, T. M., Kay, A. R. & Tank, D. W. Brain magnetic resonance imaging with contrast dependent on blood oxygenation. *Proceedings of the National Academy of Sciences of the United States of America* 87, 9868-9872 (1990).

40 Ogawa, S., Lee, T. M., Nayak, A. S. & Glynn, P. Oxygenation-sensitive contrast in magnetic resonance image of rodent brain at high magnetic fields. *Magnetic resonance in medicine : official journal of the Society of Magnetic Resonance in Medicine / Society of Magnetic Resonance in Medicine* 14, 68-78 (1990).

41 Ogawa, S. *et al.* Functional brain mapping by blood oxygenation level-dependent contrast magnetic resonance imaging. A comparison of signal characteristics with a biophysical model. *Biophysical journal* 64, 803-812, doi:10.1016/S0006-3495(93)81441-3 (1993).

42 Thulborn, K. R., Waterton, J. C., Matthews, P. M. & Radda, G. K. Oxygenation dependence of the transverse relaxation time of water protons in whole blood at high field. *Biochimica et biophysica acta* 714, 265-270 (1982).

43 Boxerman, J. L. *et al.* The intravascular contribution to fMRI signal change: Monte Carlo modeling and diffusion-weighted studies in vivo. *Magnetic resonance in medicine : official journal of the Society of Magnetic Resonance in Medicine / Society of Magnetic Resonance in Medicine* 34, 4-10 (1995).

44 Song, A. W. Single-shot EPI with signal recovery from the susceptibility-induced losses. *Magnetic resonance in medicine : official journal of the Society of Magnetic Resonance in Medicine / Society of Magnetic Resonance in Medicine* 46, 407-411 (2001).

45 Zhong, J., Kennan, R. P., Fulbright, R. K. & Gore, J. C. Quantification of intravascular and extravascular contributions to BOLD effects induced by alteration in oxygenation or intravascular contrast agents. *Magnetic resonance in medicine : official journal of the Society of Magnetic Resonance in Medicine / Society of Magnetic Resonance in Medicine* 40, 526-536 (1998).

46 Duong, T. Q. *et al.* Microvascular BOLD contribution at 4 and 7 T in the human brain: gradient-echo and spin-echo fMRI with suppression of blood effects. *Magnetic resonance in medicine : official journal of the Society of Magnetic Resonance in Medicine / Society of Magnetic Resonance in Medicine* 49, 1019-1027, doi:10.1002/mrm.10472 (2003).

47 Yoder, D. A., Zhao, Y., Paschal, C. B. & Fitzpatrick, J. M. MRI simulator with object-specific field map calculations. *Magnetic resonance imaging* 22, 315-328, doi:10.1016/j.mri.2003.10.001 (2004).

48 Ugurbil, K. *et al.* Magnetic resonance studies of brain function and neurochemistry. *Annual review of biomedical engineering* 2, 633-660, doi:10.1146/annurev.bioeng.2.1.633 (2000).

49 Duong, T. Q., Kim, D. S., Ugurbil, K. & Kim, S. G. Spatiotemporal dynamics of the BOLD fMRI signals: toward mapping submillimeter cortical columns using the early negative response. *Magnetic resonance in medicine : official journal of the Society of Magnetic Resonance in Medicine / Society of Magnetic Resonance in Medicine* 44, 231-242 (2000).

50 Shmuel, A., Yacoub, E., Chaimow, D., Logothetis, N. K. & Ugurbil, K. Spatio-temporal point-spread function of fMRI signal in human gray matter at 7 Tesla. *NeuroImage* 35, 539-552, doi:10.1016/j.neuroimage.2006.12.030 (2007).

51 Yacoub, E., Shmuel, A., Logothetis, N. & Ugurbil, K. Robust detection of ocular dominance columns in humans using Hahn Spin Echo BOLD functional MRI at 7 Tesla. *NeuroImage* 37, 1161-1177, doi:10.1016/j.neuroimage.2007.05.020 (2007).

52 Detre, J. A. MR perfusion imaging of hyperacute stroke. *AJNR. American journal of neuroradiology* 22, 806-807 (2001).

53 Detre, J. A. & Alsop, D. C. Perfusion magnetic resonance imaging with continuous arterial spin labeling: methods and clinical applications in the central nervous system. *European journal of radiology* 30, 115-124 (1999).

54 Detre, J. A., Leigh, J. S., Williams, D. S. & Koretsky, A. P. Perfusion imaging. *Magnetic resonance in medicine : official journal of the Society of Magnetic Resonance in Medicine / Society of Magnetic Resonance in Medicine* 23, 37-45 (1992).

55 Detre, J. A. *et al.* Tissue specific perfusion imaging using arterial spin labeling. *Nmr Biomed* 7, 75-82 (1994).

56 Williams, D. S., Detre, J. A., Leigh, J. S. & Koretsky, A. P. Magnetic resonance imaging of perfusion using spin inversion of arterial water. *Proceedings of the National Academy of Sciences of the United States of America* 89, 212-216 (1992).

57 Ye, F. Q. *et al.* Correction for vascular artifacts in cerebral blood flow values measured by using arterial spin tagging techniques. *Magnetic resonance in medicine : official journal of the Society of Magnetic Resonance in Medicine / Society of Magnetic Resonance in Medicine* 37, 226-235 (1997).

58 Alsop, D. C. & Detre, J. A. Multisection cerebral blood flow MR imaging with continuous arterial spin labeling. *Radiology* 208, 410-416 (1998).

59 Luh, W. M., Wong, E. C., Bandettini, P. A. & Hyde, J. S. QUIPSS II with thin-slice TI1 periodic saturation: a method for improving accuracy of quantitative perfusion imaging using pulsed arterial spin labeling. *Magnetic resonance in medicine : official journal of the Society of Magnetic Resonance in Medicine / Society of Magnetic Resonance in Medicine* 41, 1246-1254 (1999).

60 Wong, E. C., Buxton, R. B. & Frank, L. R. Quantitative imaging of perfusion using a single subtraction (QUIPSS and QUIPSS II). *Magn Reson Med* 39, 702-708 (1998).

61 Brown, G. G., Clark, C. & Liu, T. T. Measurement of cerebral perfusion with arterial spin labeling: Part 2. Applications. *Journal of the International Neuropsychological Society : JINS* 13, 526-538, doi:10.1017/S1355617707070634 (2007).

62 Liu, T. T. & Brown, G. G. Measurement of cerebral perfusion with arterial spin labeling: Part 1. Methods. *Journal of the International Neuropsychological Society : JINS* 13, 517-525, doi:10.1017/S1355617707070646 (2007).

63 Fernandez-Seara, M. A. *et al.* Imaging mesial temporal lobe activation during scene encoding: comparison of fMRI using BOLD and arterial spin labeling. *Human brain mapping* 28, 1391-1400, doi:10.1002/hbm.20366 (2007).

64 Federspiel, A., Muller, T. J., Horn, H., Kiefer, C. & Strik, W. K. Comparison of spatial and temporal pattern for fMRI obtained with BOLD and arterial spin labeling. *Journal of neural transmission* 113, 1403-1415, doi:10.1007/s00702-006-0434-5 (2006).

65 Mildner, T., Zysset, S., Trampel, R., Driesel, W. & Moller, H. E. Towards quantification of blood-flow changes during cognitive task activation using perfusion-based fMRI. *NeuroImage* 27, 919-926, doi:10.1016/j.neuroimage.2005.04.040 (2005).

66 Wong, E. C., Buxton, R. B. & Frank, L. R. Implementation of quantitative perfusion imaging techniques for functional brain mapping using pulsed arterial spin labeling. *Nmr Biomed* 10, 237-249 (1997).

67 Kim, S. G. & Ugurbil, K. Comparison of blood oxygenation and cerebral blood flow effects in fMRI: estimation of relative oxygen consumption change. *Magnetic resonance in medicine : official journal of the Society of Magnetic Resonance in Medicine / Society of Magnetic Resonance in Medicine* 38, 59-65 (1997).

68 Yang, Y. *et al.* Multislice imaging of quantitative cerebral perfusion with pulsed arterial spin labeling. *Magnetic resonance in medicine : official journal of the Society of Magnetic Resonance in Medicine / Society of Magnetic Resonance in Medicine* 39, 825-832 (1998).

69 Mandeville, J. B. *et al.* Dynamic liver imaging with iron oxide agents: effects of size and biodistribution on contrast. *Magnetic resonance in medicine : official journal of the Society of Magnetic Resonance in Medicine / Society of Magnetic Resonance in Medicine* 37, 885-890 (1997).

70 van Sluis, R. *et al.* In vivo imaging of extracellular pH using 1H MRSI. *Magnetic resonance in medicine : official journal of the Society of Magnetic Resonance in Medicine / Society of Magnetic Resonance in Medicine* 41, 743-750 (1999).

71 Garcia-Martin, M. L. *et al.* Mapping extracellular pH in rat brain gliomas in vivo by 1H magnetic resonance spectroscopic imaging: comparison with maps of metabolites. *Cancer research* 61, 6524-6531 (2001).

72 Gasparovic, C. *et al.* A study of imidazole-based nuclear magnetic resonance probes of cellular pH. *Analytical biochemistry* 261, 64-72, doi:10.1006/abio.1998.2698 (1998).

73 Dager, S. R. *et al.* Two-dimensional proton echo-planar spectroscopic imaging of brain metabolic changes during lactate-induced panic. *Archives of general psychiatry* 56, 70-77 (1999).

74 Dager, S. R., Richards, T., Strauss, W. & Artru, A. Single-voxel 1H-MRS investigation of brain metabolic changes during lactate-induced panic. *Psychiatry research* 76, 89-99 (1997).

75 Layton, M. E., Friedman, S. D. & Dager, S. R. Brain metabolic changes during lactate-induced panic: effects of gabapentin treatment. *Depression and anxiety* 14, 251-254 (2001).

76 Rainey, J. M., Jr. *et al.* Panic anxiety and lactate metabolism. *Psychopharmacology bulletin* 21, 434-437 (1985).

77 Rehncrona, S., Rosen, I. & Siesjo, B. K. Brain lactic acidosis and ischemic cell damage: 1. Biochemistry and neurophysiology. *Journal of cerebral blood flow and metabolism : official journal of the International Society of Cerebral Blood Flow and Metabolism* 1, 297-311, doi:10.1038/jcbfm.1981.34 (1981).

78 van Rijen, P. C. *et al.* 1H and 31P NMR measurement of cerebral lactate, high-energy phosphate levels, and pH in humans during voluntary hyperventilation: associated EEG, capnographic, and Doppler findings. *Magnetic resonance in medicine : official journal of the Society of Magnetic Resonance in Medicine / Society of Magnetic Resonance in Medicine* 10, 182-193 (1989).

79 King, L. R., McLaurin, R. L. & Knowles, H. C., Jr. Acid-base balance and arterial and CSF lactate levels following human head injury. *Journal of neurosurgery* 40, 617-625, doi:10.3171/jns.1974.40.5.0617 (1974).

80 Enevoldsen, E. M., Cold, G., Jensen, F. T. & Malmros, R. Dynamic changes in regional CBF, intraventricular pressure, CSF pH and lactate levels during the acute phase of head injury. *Journal of neurosurgery* 44, 191-214, doi:10.3171/jns.1976.44.2.0191 (1976).

81 Vermathen, P., Capizzano, A. A. & Maudsley, A. A. Administration and (1)H MRS detection of histidine in human brain: application to in vivo pH measurement. *Magnetic resonance in medicine : official journal of the Society of Magnetic Resonance in Medicine / Society of Magnetic Resonance in Medicine* 43, 665-675 (2000).

82 Alger, J. R., Brunetti, A., Nagashima, G. & Hossmann, K. A. Assessment of postischemic cerebral energy metabolism in cat by 31P NMR: the cumulative effects of secondary hypoxia and ischemia. *Journal of cerebral blood flow and metabolism : official journal of the International Society of Cerebral Blood Flow and Metabolism* 9, 506-514, doi:10.1038/jcbfm.1989.74 (1989).

83 Allen, K., Busza, A. L., Crockard, H. A. & Gadian, D. G. Brain metabolism and blood flow in acute cerebral hypoxia studied by NMR spectroscopy and hydrogen clearance. *NMR in biomedicine* 5, 48-52 (1992).

84 Sappey-Marinier, D. *et al.* Effect of photic stimulation on human visual cortex lactate and phosphates using 1H and 31P magnetic resonance spectroscopy. *Journal of cerebral blood flow and metabolism : official journal of the International Society of Cerebral Blood Flow and Metabolism* 12, 584-592, doi:10.1038/jcbfm.1992.82 (1992).

85 Redfield, C. *et al.* Analysis of the solution structure of human interleukin-4 determined by heteronuclear three-dimensional nuclear magnetic resonance techniques. *Journal of molecular biology* 238, 23-41, doi:10.1006/jmbi.1994.1265 (1994).

86 Jia, G. *et al.* Amide proton transfer MR imaging of prostate cancer: a preliminary study. *Journal of magnetic resonance imaging : JMRI* 33, 647-654, doi:10.1002/jmri.22480 (2011).

87 Jones, C. K. *et al.* Amide proton transfer imaging of human brain tumors at 3T. *Magnetic resonance in medicine : official journal of the Society of Magnetic Resonance in Medicine / Society of Magnetic Resonance in Medicine* 56, 585-592, doi:10.1002/mrm.20989 (2006).

88 Salhotra, A. *et al.* Amide proton transfer imaging of 9L gliosarcoma and human glioblastoma xenografts. *Nmr Biomed* 21, 489-497, doi:10.1002/nbm.1216 (2008).

89 Sun, P. Z., Zhou, J., Huang, J. & van Zijl, P. Simplified quantitative description of amide proton transfer (APT) imaging during acute ischemia. *Magnetic resonance in medicine : official journal of the Society of Magnetic Resonance in Medicine / Society of Magnetic Resonance in Medicine* 57, 405-410, doi:10.1002/mrm.21151 (2007).

90 Sun, P. Z., Zhou, J., Sun, W., Huang, J. & van Zijl, P. C. Suppression of lipid artifacts in amide proton transfer imaging. *Magnetic resonance in medicine : official journal of the Society of Magnetic Resonance in Medicine / Society of Magnetic Resonance in Medicine* 54, 222-225, doi:10.1002/mrm.20530 (2005).

91 Zhao, X. *et al.* Saturation power dependence of amide proton transfer image contrasts in human brain tumors and strokes at 3 T. *Magnetic resonance in medicine : official journal of the Society of Magnetic Resonance in Medicine / Society of Magnetic Resonance in Medicine* 66, 1033-1041, doi:10.1002/mrm.22891 (2011).

92 Zhou, J. Amide proton transfer imaging of the human brain. *Methods in molecular biology* 711, 227-237, doi:10.1007/978-1-61737-992-5_10 (2011).

93 Zhou, J., Lal, B., Wilson, D. A., Laterra, J. & van Zijl, P. C. Amide proton transfer (APT) contrast for imaging of brain tumors. *Magnetic resonance in medicine : official journal of the Society of Magnetic Resonance in Medicine / Society of Magnetic Resonance in Medicine* 50, 1120-1126, doi:10.1002/mrm.10651 (2003).

94 Zhou, J. Y., Payen, J. F., Wilson, D. A., Traystman, R. J. & van Zijl, P. C. M. Using the amide proton signals of intracellular proteins and peptides to detect pH effects in MRI. *Nat Med* 9, 1085-1090, doi:Doi 10.1038/Nm907 (2003).

95 Mori, S., Eleff, S. M., Pilatus, U., Mori, N. & van Zijl, P. C. Proton NMR spectroscopy of solvent-saturable resonances: a new approach to study pH effects in situ. *Magnetic resonance in medicine : official journal of the Society of Magnetic Resonance in Medicine / Society of Magnetic Resonance in Medicine* 40, 36-42 (1998).

96 van Zijl, P. C. *et al.* Mechanism of magnetization transfer during on-resonance water saturation. A new approach to detect mobile proteins, peptides, and lipids. *Magnetic resonance in medicine : official journal of the Society of Magnetic Resonance in Medicine / Society of Magnetic Resonance in Medicine* 49, 440-449, doi:10.1002/mrm.10398 (2003).

97 Englander, S. W., Downer, N. W. & Teitelbaum, H. Hydrogen exchange. *Annual review of biochemistry* 41, 903-924, doi:10.1146/annurev.bi.41.070172.004351 (1972).

98 Liepinsh, E. & Otting, G. Proton exchange rates from amino acid side chains--implications for image contrast. *Magnetic resonance in medicine : official journal of the Society of Magnetic Resonance in Medicine / Society of Magnetic Resonance in Medicine* 35, 30-42 (1996).

99 Zhou, J., Payen, J. F., Wilson, D. A., Traystman, R. J. & van Zijl, P. C. Using the amide proton signals of intracellular proteins and peptides to detect pH effects in MRI. *Nat Med* 9, 1085-1090, doi:10.1038/nm907 (2003).

100 Covingto.Ak, Robinson, R. A. & Bates, R. G. Ionization Constant of Deuterium Oxide from 5 to 50 Degrees. *J Phys Chem-Us* 70, 3820-& (1966).

101 Sun, P. Z. *et al.* Relaxation-compensated fast multislice amide proton transfer (APT) imaging of acute ischemic stroke. *Magnetic resonance in medicine : official journal of the Society of Magnetic Resonance in Medicine / Society of Magnetic Resonance in Medicine* 59, 1175-1182, doi:10.1002/mrm.21591 (2008).

102 Sun, P. Z., van Zijl, P. C. & Zhou, J. Optimization of the irradiation power in chemical exchange dependent saturation transfer experiments. *Journal of magnetic resonance* 175, 193-200, doi:10.1016/j.jmr.2005.04.005 (2005).

103 Sun, P. Z., Zhou, J., Sun, W., Huang, J. & van Zijl, P. C. Detection of the ischemic penumbra using pH-weighted MRI. *Journal of cerebral blood flow and metabolism : official journal of the International Society of Cerebral Blood Flow and Metabolism* 27, 1129-1136, doi:10.1038/sj.jcbfm.9600424 (2007).

104 Samson, R. S., Wheeler-Kingshott, C. A., Symms, M. R., Tozer, D. J. & Tofts, P. S. A simple correction for B1 field errors in magnetization transfer ratio measurements. *Magnetic resonance imaging* 24, 255-263, doi:10.1016/j.mri.2005.10.025 (2006).

105 Kettunen, M. I., Grohn, O. H., Penttonen, M. & Kauppinen, R. A. Cerebral T1rho relaxation time increases immediately upon global ischemia in the rat independently of blood glucose and anoxic depolarization. *Magnetic resonance in medicine : official journal of the Society of Magnetic Resonance in Medicine / Society of Magnetic Resonance in Medicine* 46, 565-572 (2001).

106 Kettunen, M. I., Grohn, O. H., Silvennoinen, M. J., Penttonen, M. & Kauppinen, R. A. Effects of intracellular pH, blood, and tissue oxygen tension on T1rho relaxation in rat brain. *Magnetic resonance in medicine : official journal of the Society of Magnetic Resonance in Medicine / Society of Magnetic Resonance in Medicine* 48, 470-477, doi:10.1002/mrm.10233 (2002).

107 Engelhardt, R. T. & Johnson, G. A. T1 rho relaxation and its application to MR histology. *Magnetic resonance in medicine : official journal of the Society of Magnetic Resonance in Medicine / Society of Magnetic Resonance in Medicine* 35, 781-786 (1996).

108 Wheaton, A. J., Borthakur, A., Corbo, M., Charagundla, S. R. & Reddy, R. Method for reduced SAR T1rho-weighted MRI. *Magnetic resonance in medicine : official journal of the Society of Magnetic Resonance in Medicine / Society of Magnetic Resonance in Medicine* 51, 1096-1102, doi:10.1002/mrm.20141 (2004).

109 Bloembergen, N., Purcell, E. M. & Pound, R. V. Relaxation Effects in Nuclear Magnetic Resonance Absorption. *Phys Rev* 73, 679-712 (1948).

110 McIntosh, T. K., Faden, A. I., Bendall, M. R. & Vink, R. Traumatic brain injury in the rat: alterations in brain lactate and pH as characterized by 1H and 31P nuclear magnetic resonance. *Journal of neurochemistry* 49, 1530-1540 (1987).

111 Zipp, A., Kuntz, I. D. & James, T. L. Hemoglobin-water interactions in normal and sickle erythrocytes by proton magnetic resonance T1p measurements. *Archives of biochemistry and biophysics* 178, 435-441 (1977).

112 Chesler, M. Regulation and modulation of pH in the brain. *Physiological reviews* 83, 1183-1221, doi:10.1152/physrev.00010.2003 (2003).

113 Stewart, P. A. Independent and dependent variables of acid-base control. *Respiration physiology* 33, 9-26 (1978).

114 Traynelis, S. F. & Chesler, M. Proton release as a modulator of presynaptic function. *Neuron* 32, 960-962 (2001).

115 Tresguerres, M., Buck, J. & Levin, L. R. Physiological carbon dioxide, bicarbonate, and pH sensing. *Pflugers Archiv : European journal of physiology* 460, 953-964, doi:10.1007/s00424-010-0865-6 (2010).

116 Wemmie, J. A., Price, M. P. & Welsh, M. J. Acid-sensing ion channels: advances, questions and therapeutic opportunities. *Trends in neurosciences* 29, 578-586, doi:10.1016/j.tins.2006.06.014 (2006).

117 Ziemann, A. E. *et al.* The amygdala is a chemosensor that detects carbon dioxide and acidosis to elicit fear behavior. *Cell* 139, 1012-1021, doi:10.1016/j.cell.2009.10.029 (2009).

118 Petroff, O. A. *et al.* Cerebral intracellular pH by 31P nuclear magnetic resonance spectroscopy. *Neurology* 35, 781-788 (1985).

119 Siesjo, B. K., von Hanwehr, R., Nergelius, G., Nevander, G. & Ingvar, M. Extra- and intracellular pH in the brain during seizures and in the recovery period following the arrest of seizure activity. *Journal of cerebral blood flow and metabolism : official journal of the International Society of Cerebral Blood Flow and Metabolism* 5, 47-57, doi:10.1038/jcbfm.1985.7 (1985).

120 Maddock, R. J., Buonocore, M. H., Copeland, L. E. & Richards, A. L. Elevated brain lactate responses to neural activation in panic disorder: a dynamic 1H-MRS study. *Molecular psychiatry* 14, 537-545, doi:10.1038/sj.mp.4002137 (2009).

121 Coryell, M. W. *et al.* Restoring Acid-sensing ion channel-1a in the amygdala of knock-out mice rescues fear memory but not unconditioned fear responses. *The Journal of neuroscience : the official journal of the Society for Neuroscience* 28, 13738-13741, doi:10.1523/JNEUROSCI.3907-08.2008 (2008).

122 Coryell, W., Dindo, L., Fyer, A. & Pine, D. S. Onset of spontaneous panic attacks: A prospective study of risk factors. *Psychosom Med* 68, 754-757, doi:DOI 10.1097/01.psy.0000232268.00327.b4 (2006).

123 Wemmie, J. A. *et al.* Overexpression of acid-sensing ion channel 1a in transgenic mice increases acquired fear-related behavior. *Proceedings of the National Academy of Sciences of the United States of America* 101, 3621-3626, doi:10.1073/pnas.0308753101 (2004).

124 Dager, S. R. *et al.* Brain metabolic alterations in medication-free patients with bipolar disorder. *Archives of general psychiatry* 61, 450-458, doi:10.1001/archpsyc.61.5.450 (2004).

125 Bhujwalla, Z. M., McCoy, C. L., Glickson, J. D., Gillies, R. J. & Stubbs, M. Estimations of intra- and extracellular volume and pH by 31P magnetic resonance spectroscopy: effect of therapy on RIF-1 tumours. *British journal of cancer* 78, 606-611 (1998).

126 Gillies, R. J., Liu, Z. & Bhujwalla, Z. 31P-MRS measurements of extracellular pH of tumors using 3-aminopropylphosphonate. *The American journal of physiology* 267, C195-203 (1994).

127 Raghunand, N., Howison, C., Sherry, A. D., Zhang, S. & Gillies, R. J. Renal and systemic pH imaging by contrast-enhanced MRI. *Magnetic resonance in medicine : official journal of the Society of Magnetic Resonance in Medicine / Society of Magnetic Resonance in Medicine* 49, 249-257, doi:10.1002/mrm.10347 (2003).

128 Raghunand, N., Zhang, S., Sherry, A. D. & Gillies, R. J. In vivo magnetic resonance imaging of tissue pH using a novel pH-sensitive contrast agent, GdDOTA-4AmP. *Academic radiology* 9 Suppl 2, S481-483 (2002).

129 Aime, S. *et al.* Paramagnetic lanthanide(III) complexes as pH-sensitive chemical exchange saturation transfer (CEST) contrast agents for MRI applications. *Magnetic resonance in medicine : official journal of the Society of Magnetic Resonance in Medicine / Society of Magnetic Resonance in Medicine* 47, 639-648 (2002).

130 Ward, K. M. & Balaban, R. S. Determination of pH using water protons and chemical exchange dependent saturation transfer (CEST). *Magnetic resonance in medicine : official journal of the Society of Magnetic Resonance in Medicine / Society of Magnetic Resonance in Medicine* 44, 799-802 (2000).

131 Zhang, S., Merritt, M., Woessner, D. E., Lenkinski, R. E. & Sherry, A. D. PARACEST agents: modulating MRI contrast via water proton exchange. *Accounts of chemical research* 36, 783-790, doi:10.1021/ar020228m (2003).

132 Liu, G., Li, Y., Sheth, V. R. & Pagel, M. D. Imaging in vivo extracellular pH with a single paramagnetic chemical exchange saturation transfer magnetic resonance imaging contrast agent. *Molecular imaging* 11, 47-57 (2012).

133 Longo, D. L., Busato, A., Lanzardo, S., Antico, F. & Aime, S. Imaging the pH evolution of an acute kidney injury model by means of iopamidol, a MRI-CEST pH-responsive contrast agent. *Magnetic resonance in medicine : official journal of the Society of Magnetic Resonance in Medicine / Society of Magnetic Resonance in Medicine*, doi:10.1002/mrm.24513 (2012).

134 Takayama, Y. *et al.* Ytterbium-based PARACEST agent: feasibility of CEST imaging on a clinical MR scanner. *Magnetic resonance in medical sciences : MRMS : an official journal of Japan Society of Magnetic Resonance in Medicine* 11, 35-41 (2012).

135 Patel, N., Forton, D. M., Coutts, G. A., Thomas, H. C. & Taylor-Robinson, S. D. Intracellular pH measurements of the whole head and the basal ganglia in chronic liver disease: a phosphorus-31 MR spectroscopy study. *Metabolic brain disease* 15, 223-240 (2000).

136 Stubbs, M. *et al.* An assessment of 31P MRS as a method of measuring pH in rat tumours. *NMR in biomedicine* 5, 351-359 (1992).

137 Pan, J. W., Hamm, J. R., Rothman, D. L. & Shulman, R. G. Intracellular pH in human skeletal muscle by 1H NMR. *Proceedings of the National Academy of Sciences of the United States of America* 85, 7836-7839 (1988).

138 Rothman, D. L., Behar, K. L., Prichard, J. W. & Petroff, O. A. Homocarnosine and the measurement of neuronal pH in patients with epilepsy. *Magnetic resonance in medicine : official journal of the Society of Magnetic Resonance in Medicine / Society of Magnetic Resonance in Medicine* 38, 924-929 (1997).

139 Magnotta, V. A. *et al.* Detecting activity-evoked pH changes in human brain. *Proceedings of the National Academy of Sciences of the United States of America* 109, 8270-8273, doi:10.1073/pnas.1205902109 (2012).

140 Zhang, X., Lin, Y. & Gillies, R. J. Tumor pH and its measurement. *Journal of nuclear medicine : official publication, Society of Nuclear Medicine* 51, 1167-1170, doi:10.2967/jnumed.109.068981 (2010).

141 Jin, T., Autio, J., Obata, T. & Kim, S. G. Spin-locking versus chemical exchange saturation transfer MRI for investigating chemical exchange process between water and labile metabolite protons. *Magnetic resonance in medicine : official journal of the Society of Magnetic Resonance in Medicine / Society of Magnetic Resonance in Medicine* 65, 1448-1460, doi:10.1002/mrm.22721 (2011).

142 Vafaee, M. S. *et al.* Frequency-dependent changes in cerebral metabolic rate of oxygen during activation of human visual cortex. *Journal of cerebral blood flow and metabolism : official journal of the International Society of Cerebral Blood Flow and Metabolism* 19, 272-277, doi:10.1097/00004647-199903000-00005 (1999).

143 Singh, M., Kim, S. & Kim, T. S. Correlation between BOLD-fMRI and EEG signal changes in response to visual stimulus frequency in humans. *Magnetic resonance in medicine : official journal of the Society of Magnetic Resonance in Medicine / Society of Magnetic Resonance in Medicine* 49, 108-114, doi:10.1002/mrm.10335 (2003).

144 Fox, P. T. & Raichle, M. E. Stimulus rate dependence of regional cerebral blood flow in human striate cortex, demonstrated by positron emission tomography. *Journal of neurophysiology* 51, 1109-1120 (1984).

145 Lin, A. L. *et al.* Evaluation of MRI models in the measurement of CMRO2 and its relationship with CBF. *Magnetic resonance in medicine : official journal of the Society of Magnetic Resonance in Medicine / Society of Magnetic Resonance in Medicine* 60, 380-389, doi:10.1002/mrm.21655 (2008).

146 Lin, A. L., Fox, P. T., Hardies, J., Duong, T. Q. & Gao, J. H. Nonlinear coupling between cerebral blood flow, oxygen consumption, and ATP production in human visual cortex. *Proceedings of the National Academy of Sciences of the United States of America* 107, 8446-8451, doi:10.1073/pnas.0909711107 (2010).

147 Vafaee, M. S. & Gjedde, A. Model of blood-brain transfer of oxygen explains nonlinear flow-metabolism coupling during stimulation of visual cortex. *Journal of cerebral blood flow and metabolism : official journal of the International Society of Cerebral Blood Flow and Metabolism* 20, 747-754, doi:10.1097/00004647-200004000-00012 (2000).

148 Pawela, C. P. *et al.* Modeling of region-specific fMRI BOLD neurovascular response functions in rat brain reveals residual differences that correlate with the differences in regional evoked potentials. *NeuroImage* 41, 525-534, doi:10.1016/j.neuroimage.2008.02.022 (2008).

149 Prichard, J. *et al.* Lactate rise detected by 1H NMR in human visual cortex during physiologic stimulation. *Proceedings of the National Academy of Sciences of the United States of America* 88, 5829-5831 (1991).

150 Kety, S. S. & Schmidt, C. F. The Effects of Altered Arterial Tensions of Carbon Dioxide and Oxygen on Cerebral Blood Flow and Cerebral Oxygen Consumption of Normal Young Men. *The Journal of clinical investigation* 27, 484-492, doi:10.1172/JCI101995 (1948).

151 Maddess, T., McCourt, M. E., Blakeslee, B. & Cunningham, R. B. Factors governing the adaptation of cells in area-17 of the cat visual cortex. *Biological cybernetics* 59, 229-236 (1988).

152 Ho, W. A. & Berkley, M. A. Evoked potential estimates of the time course of adaptation and recovery to counterphase gratings. *Vision research* 28, 1287-1296 (1988).

153 Janz, C., Heinrich, S. P., Kornmayer, J., Bach, M. & Hennig, J. Coupling of neural activity and BOLD fMRI response: new insights by combination of fMRI and VEP experiments in transition from single events to continuous stimulation. *Magnetic*

resonance in medicine : official journal of the Society of Magnetic Resonance in Medicine / Society of Magnetic Resonance in Medicine 46, 482-486 (2001).

154 Abelson, J. L., Weg, J. G., Nesse, R. M. & Curtis, G. C. Persistent respiratory irregularity in patients with panic disorder. *Biological Psychiatry* 49, 588-595 (2001).

155 Abelson, J. L., Weg, J. G., Nesse, R. M. & Curtis, G. C. Persistent respiratory irregularity in patients with panic disorder. *Biological Psychiatry* 39, 77-77 (1996).

156 Philibert, R. A., Nelson, J. J., Sandhu, H. K., Crowe, R. R. & Coryell, W. H. Association of an exonic LDHA polymorphism with altered respiratory response in probands at high risk for panic disorder. *American Journal of Medical Genetics Part B-Neuropsychiatric Genetics* 117B, 11-17, doi:Doi 10.1002/Ajmg.B.10015 (2003).

157 Philibert, R. A., Sandhu, H. K., Nelson, J. J., Crowe, R. R. & Coryell, W. H. An association of an exonic LDHA polymorphism with altered respiratory response in probands at high risk for panic disorder. *Biological Psychiatry* 51, 127s-127s (2002).

158 Coryell, W., Fyer, A., Pine, D., Martinez, J. & Arndt, S. Aberrant respiratory sensitivity to CO2 as a trait of familial panic disorder. *Biological Psychiatry* 49, 582-587 (2001).

159 Buxton, R. B., Wong, E. C. & Frank, L. R. Dynamics of blood flow and oxygenation changes during brain activation: the balloon model. *Magnetic resonance in medicine : official journal of the Society of Magnetic Resonance in Medicine / Society of Magnetic Resonance in Medicine* 39, 855-864 (1998).

160 Uludag, K., Muller-Bierl, B. & Ugurbil, K. An integrative model for neuronal activity-induced signal changes for gradient and spin echo functional imaging. *NeuroImage* 48, 150-165, doi:10.1016/j.neuroimage.2009.05.051 (2009).

161 Ugurbil, K., Toth, L. & Kim, D. S. How accurate is magnetic resonance imaging of brain function? *Trends in neurosciences* 26, 108-114, doi:10.1016/S0166-2236(02)00039-5 (2003).

162 Lee, A. T., Glover, G. H. & Meyer, C. H. Discrimination of large venous vessels in time-course spiral blood-oxygen-level-dependent magnetic-resonance functional neuroimaging. *Magnetic resonance in medicine : official journal of the Society of Magnetic Resonance in Medicine / Society of Magnetic Resonance in Medicine* 33, 745-754 (1995).

163 Saad, Z. S., Ropella, K. M., Cox, R. W. & DeYoe, E. A. Analysis and use of FMRI response delays. *Human brain mapping* 13, 74-93 (2001).

164 Silva, A. C., Williams, D. S. & Koretsky, A. P. Evidence for the exchange of arterial spin-labeled water with tissue water in rat brain from diffusion-sensitized measurements of perfusion. *Magnetic resonance in medicine : official journal of the Society of Magnetic Resonance in Medicine / Society of Magnetic Resonance in Medicine* 38, 232-237 (1997).

165 Engel, S. A., Glover, G. H. & Wandell, B. A. Retinotopic organization in human visual cortex and the spatial precision of functional MRI. *Cerebral cortex* 7, 181-192 (1997).

166 Engel, S. A. *et al.* fMRI of human visual cortex. *Nature* 369, 525, doi:10.1038/369525a0 (1994).

167 Sereno, M. I. *et al.* Borders of multiple visual areas in humans revealed by functional magnetic resonance imaging. *Science* 268, 889-893 (1995).

168 Brainard, D. H. The Psychophysics Toolbox. *Spatial vision* 10, 433-436 (1997).

169 Pelli, D. G. The VideoToolbox software for visual psychophysics: transforming numbers into movies. *Spatial vision* 10, 437-442 (1997).

170 Dale, A. M., Fischl, B. & Sereno, M. I. Cortical surface-based analysis. I. Segmentation and surface reconstruction. *NeuroImage* 9, 179-194, doi:10.1006/nimg.1998.0395 (1999).

171 Fischl, B., Sereno, M. I. & Dale, A. M. Cortical surface-based analysis. II: Inflation, flattening, and a surface-based coordinate system. *NeuroImage* 9, 195-207, doi:10.1006/nimg.1998.0396 (1999).

172 Fischl, B., Sereno, M. I., Tootell, R. B. & Dale, A. M. High-resolution intersubject averaging and a coordinate system for the cortical surface. *Human brain mapping* 8, 272-284 (1999).

173 Cox, R. W. AFNI: software for analysis and visualization of functional magnetic resonance neuroimages. *Computers and biomedical research, an international journal* 29, 162-173 (1996).

174 Cavusoglu, M., Bartels, A., Yesilyurt, B. & Uludag, K. Retinotopic maps and hemodynamic delays in the human visual cortex measured using arterial spin labeling. *NeuroImage* 59, 4044-4054, doi:10.1016/j.neuroimage.2011.10.056 (2012).